UNIVERSITY OF LODZ
UNIVERSITÀ DEGLI STUDI DI TRIESTE

XXX CICLO DEL DOTTORATO DI RICERCA IN FISICA

HIGH ENERGY RADIATION FROM LOW-LUMINOSITY ACCRETING BLACK HOLES

Settore scientifico-disciplinare: **FIS/01 Fisica Sperimentale**

DOTTORANDO / A
RAFAŁ WOJACZYŃSKI

COORDINATORE
PROF. PIOTR KOSIŃSKI
PROF. LIVIO LANCERI

SUPERVISORE DI TESI
PROF. ANDRZEJ NIEDŹWIECKI
PROF. FRANCESCO LONGO

ANNO ACCADEMICO 2016/2017

WYDZIAŁ FIZYKI
i INFORMATYKI
STOSOWANEJ
Uniwersytet Łódzki

HIGH ENERGY RADIATION FROM LOW-LUMINOSITY ACCRETING BLACK HOLES

Rafał Wojaczyński

Advisors:

Prof. Andrzej Niedźwiecki

Prof. Francesco Longo

October 10, 2018

Acknowledgements

I would like to thank:
Andrzej Niedźwiecki as supervisor of this thesis. Thank you for giving me chance at the beginning and all hard work during my studies.
Francesco Longo as second supervisor for Fermi and AGILE scientific advices and all support during my stay in Trieste.
My referees: Carlotta Pittori and Piotr Lubiński for valuable comments that improved final version of this thesis.
My wife Magda, and my daughter Martyna for being very patient while I was struggling with scientific problems and not spent time with them.
My parents and all my friends to support me during this important years.

Abstract (English)

This PhD thesis includes theoretical and observational studies of γ-ray emission from radio-quiet accreting black holes. The theoretical motivation for the search of γ-ray emission from such sources concerns the considerable hadronic production of γ-rays predicted by models of hot flows, which most likely power these sources at low luminosities. I thoroughly investigated this model prediction and I found that the luminosity at either hundreds of MeV or in the GeV range, depending on proton distribution, can reach $\sim 10^{-5} L_{\rm Edd}$ for the X-ray luminosities between $\sim 10^{-4} L_{\rm Edd}$ and $10^{-3} L_{\rm Edd}$. These levels of γ-ray luminosities can be probed in some Seyfert galaxies. Comparing the model predictions with *Fermi*/LAT upper limits for NGC 4258, NGC 7213 and NGC 4151 I found interesting constraints on the acceleration efficiency of protons, plasma magnetization and black hole spins.

I found an interesting hint for a γ-ray signal in the LAT data from NGC 4151, which is only slightly below the formal detection threshold of 5σ.

I also found hints for the correlation between the X-ray and γ-ray emission in the nearby galaxy NGC 4945, which harbors both an active galactic nucleus and a nuclear starburst region. I have divided the *Fermi*/LAT observations of NGC 4945 into two datasets, comprising events detected during the low and high level of X-ray emission from the active nucleus of this galaxy, determined using the *Swift*/BAT light curve. I found a $\sim 5\sigma$ difference between spectral parameters fitted to these datasets, and a similar significance of the reversal of the γ-ray signal in significance maps for low and high γ-ray energies. This X/γ-ray correlation indicates that the γ-ray production is dominated by the active nucleus rather than by cosmic rays interacting with the interstellar medium. I compared NGC 4945 with other starburst galaxies detected by LAT and I note similarities between those with active nuclei, e.g. unlikely high efficiencies of γ-ray production in starburst scenario, which argues for a significant contribution of their active nuclei to the γ-ray emission.

Finally, I took into account *AGILE* observations of Cyg X-1. I found that it has not reached yet a sensitivity level needed for a detection of this source.

Abstract (Polish)

Praca doktorska obejmuje teoretyczne i obserwacyjne badania emisji promieniowania γ z radiowo cichych układów akrecyjnych wokół czarnych dziur. Teoretyczna motywacja do poszukiwania promieniowania γ z tych źródeł wynika z silnej hadronowej emisji promieniowania γ przewidywanej przez modele gorących przepływów, które najprawdopodobniej zasilają takie źródła przy niskiej jasności. W pracy dokładnie zbadałem przewidywania tego modelu i stwierdziłem, że jasność w zakresie kilkuset MeV lub w zakresie GeV, w zależności od rozkładu energii protonów, może osiągać $\sim 10^{-5} L_{\rm Edd}$, dla jasności promieniowania rentgenowskiego pomiędzy $\sim 10^{-4} L_{\rm Edd}$ i $10^{-3} L_{\rm Edd}$. Te poziomy jasności γ mogą być badane w niektórych galaktykach Seyferta. Porównując przewidywania modelu z ograniczeniami górnymi detektora *Fermi*/LAT dla galaktyk NGC 4258, NGC 7213 i NGC 4151, znalazłem interesujące ograniczenia dotyczące skuteczności przyspieszania protonów, namagnesowania plazmy i spinów czarnych dziur.

Odkryłem również interesujący sygnał γ w danych LAT z NGC 4151, który jest tylko nieznacznie poniżej formalnego progu detekcji $\sim 5\sigma$.

Odkryłem korelację między emisją promieniowania rentgenowskiego i γ w pobliskiej galaktyce NGC 4945, która zawiera zarówno aktywne jądro galaktyki, jak i region gwiazdotwórczy. Podzieliłem obserwacje *Fermi*/LAT NGC 4945 na dwa zestawy danych, obejmujące dane zarejestrowane podczas niskiego i wysokiego poziomu emisji promieniowania rentgenowskiego z aktywnego jądra tej galaktyki, określone za pomocą krzywej blasku *Swift*/BAT. Stwierdziłem różnice rzędu $\sim 5\sigma$ pomiędzy parametrami widmowymi tych zbiorów danych, oraz zmianę sygnału γ o podobnej istotności statystycznej na mapach TS (Test Statistic) dla niskich i wysokich energii promieniowania γ. Ta korelacja promieniowania X i γ wskazuje, że produkcja promieniowania γ jest zdominowana przez aktywne jądro, a nie przez promieniowanie kosmiczne oddziałujące z ośrodkiem międzygwiezdnym. Porównałem NGC 4945 z innymi galaktykami gwiazdotwórczymi odkrytymi przez LAT i zauważyłem podobieństwa między tymi zawierającymi aktywne jądro (np. zbyt silną produkcję promieniowania γ w scenariuszu gwiazdotwórczym), które przemawiają za znaczącym wkładem aktywnych jąder w emisję promieniowania γ.

W ostatniej części pracy wziąłem pod uwagę obserwacje *AGILE* dla Cyg X-1. Stwierdziłem, że *AGILE* nie osiągnął jeszcze poziomu czułości wymaganego do wykrycia tego źródła.

Abstract (Italian)

Questa tesi di dottorato comprende sia studi teorici che osservativi riguardo all'emissione di radiazione γ a seguito di fenomeni di accrescimento su buchi neri cosiddetti "radio-quieti". La motivazione teorica per la ricerca di emissione γ da tali sorgenti riguarda la considerevole produzione adronica di raggi γ prevista da modelli di flussi ad alta temperatura, che molto probabilmente alimentano queste sorgenti a basse luminosità. Questa predizione teorica del modello è stata studiata a fondo in questa tesi scoprendo che la luminosità attorno al centinaio di MeV o nella banda energetica del GeV, a seconda della distribuzione energetica dei protoni, può raggiungere $\sim 10^{-5} L_{\rm Edd}$ per sorgenti con luminosità in raggi-X tra $\sim 10^{-4} L_{\rm Edd}$ e $10^{-3} L_{\rm Edd}$. Questi livelli di luminosità di γ possono essere rivelati in alcune galassie di Seyfert. Confrontando le previsioni del modello con i limiti superiori ottenuti da *Fermi*/LAT per le sorgenti NGC 4258, NGC 7213 e NGC 4151 sono stati ricavati limiti interessanti sull'efficienza di accelerazione dei protoni, sulla magnetizzazione del plasma e sullo spin del buco nero centrale.

Si è inoltre riscontrato un possibile segnale γ nei dati ottenuti da LAT per la galassia NGC 4151, con una significatività solo leggermente inferiore alla soglia di rivelazione di 5σ.

Questa tesi ha inoltre evidenziato una possibile correlazione tra l'emissione di raggi X e γ nella vicina galassia NGC 4945, che ospita sia un nucleo galattico attivo che una regione di "starburst" nucleare. Le evidenze di tale correlazione sono state ottenute dividendo le osservazioni di NGC 4945 da parte di *Fermi*/LAT in due serie, comprendenti rispettivamente eventi rivelati durante livelli diversi (cosiddetti "alto" e "basso") di emissione nella banda dei raggi X da parte del nucleo attivo di questa galassia. I livelli alto e basso sono stati determinati analizzando la curva di luce della medesima sorgente ottenuta dallo strumento *Swift*/BAT. In questa analisi si è trovata una differenza $\sim 5\sigma$ tra i parametri spettrali ottenuti per modellizzare l'emissione gamma di questi diversi set di dati e, con la medesima evidenza, un'inversione del segnale γ nelle mappe di significatività, rispettivamente ottenute nella banda γ alle basse e alle alte energie. Questa correlazione X/γ indica che la produzione γ è dominata dal nucleo attivo piuttosto che da interazioni di raggi cosmici con il mezzo interstellare. Si è inoltre confrontato il segnale della galassia NGC 4945 con altre galassie starburst rilevate da LAT e si sono notate invece delle similitudini con quelle contenenti un nucleo attivo, manifestando ad esempio un'improbabile alta efficienza nella produzione di γ nello scenario starburst e sostenendo al contrario l'ipotesi di un contributo significativo dei loro nuclei attivi all'emissione nella banda γ.

Infine, questa tesi ha preso in considerazione le osservazioni di Cyg X-1 effettuate da *AGILE*. Ho scoperto che tali osservazioni non hanno ancora raggiunto un livello di sensitività sufficiente per la rivelazione di questa sorgente.

Sommario (Italian)

I processi di accrescimento che avvengono attorno ad oggetti compatti massivi come stelle di neutroni o buchi neri non sono ancora del tutto compresi. Esistono due tipi di sistemi astrofisici contenenti un buco nero. Il primo tipo consiste in un sistema binario contenente generalmente un buco nero con massa da un paio sino a diverse masse solari. L'altro tipo di sistemi contenente un buco nero risiede nelle zone centrali delle galassie che presentano un nucleo attivo (dette AGN, Active Galactic Nuclei). Le loro masse possono essere dell'ordine di centinaia di milioni fino a miliardi di masse solari. Ciò che caratterizza entrambi i tipi di sistemi è la forte emissione variabile nella banda dei raggi X ed un insieme di processi fisici simili che tendono a verificarsi indipendentemente dalle dimensioni del sistema. I modelli teorici costruiti a partire dagli anni 70 'prevedono anche l'emissione di raggi gamma dalla zona centrale di tali sistemi. Prima del lancio di *Fermi*/LAT e di *AGILE*/GRID non esistevano strumenti sufficientemente sensibili per rilevare potenziali emissioni di raggi gamma da sistemi galattici binari o AGN.

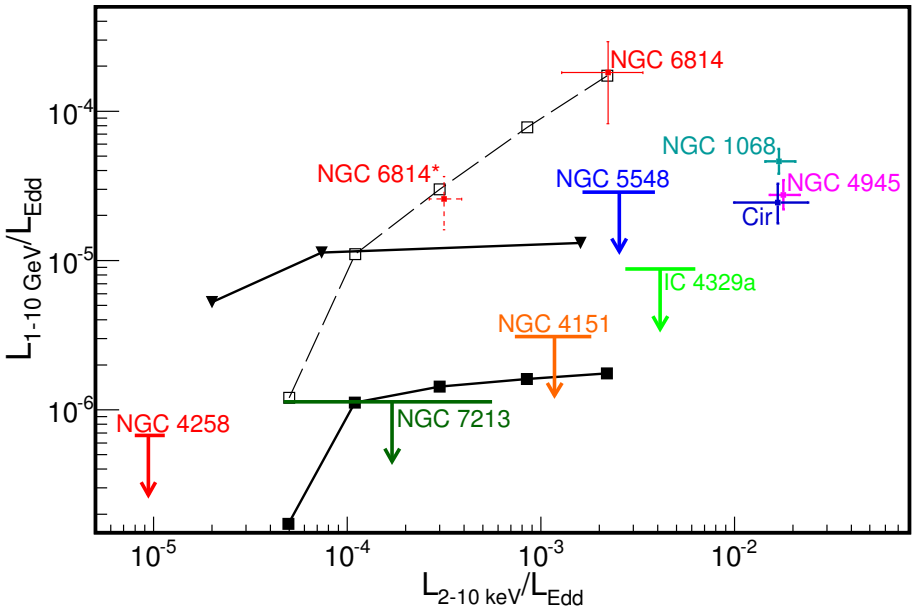

Figure 1: $\lambda_{1-10\,\mathrm{GeV}}$ come funzione di $\lambda_{2-10\,\mathrm{keV}}$, vedi Tabelle 4.1 e 4.2 per i dati osservativi; $\lambda 2-10$ keV corrisponde alla luminosità media in raggi X durante le osservazioni di *Fermi*/LAT (vedi Sezione 4.2). Le linee continue sono per il modello N con $\delta = 10^{-3}$, $a = 0.95$, $\beta = 9$ (triangoli) e per il modello $H_{0.1}$ con $\delta = 10^{-3}$, $a = 0.95$, $\beta = 9$ (quadrati). Il precedente modello supera significativamente gli *Upper Limits* per tre AGN, il che esclude uno scenario con la maggior parte della potenza dovuta all'*accretion* utilizzata per l'accelerazione dei protoni sino a velocità relativistiche. La linea tratteggiata con i quadrati aperti è per la luminosità *rest-frame* nell'ultimo modello (ad es., $H_{0.1}$). Tali luminosità γ, trascurando l'assorbimento $\gamma\gamma$ e il trasferimento GR di radiazioni, sono state studiate da Mahadevan *et al.* (1997) e Oka & Manmoto (2003). Vediamo che il trattamento semplificato di questi articoli sopravvaluta le luminosità osservate anche di due ordini di grandezza e influenza significativamente il confronto con le osservazioni.

Inoltre, si prevede che l'emissione di radiazione nella banda gamma ad alta energia avvenga solo al di sotto di alcune soglie di luminosità. Oltre il 10% della luminosità di Eddington, l'emissione termica dei raggi X domina lo spettro e il disco di accrescimento rimane in prossimità del buco nero. Al di sotto di tale valore, i raggi X sono prodotti principalmente per effetto Compton, il

disco è lontano dal centro e si prevede che si verifichi un flusso caldo in una regione vicina al buco nero. Il mio interesse si volge particolarmente a questo particolare regime. In esso sono previsti due potenziali meccanismi di creazione di raggi gamma vicino al buco nero. Uno è l'effetto Compton sugli elettroni non termici, mentre l'altro riguarda il meccanismo adronico (la collisione tra i protoni altamente energetici produce pioni neutri che decadono immediatamente in due fotoni gamma).

La mancanza apparente della rivelazione di raggi gamma in oggetti in cui la radiazione non è dominata da getti relativistici, è stata una delle motivazioni per lo studio affrontato in questa tesi di dottorato. La prima parte della ricerca consiste nella ricerca di emissione di raggi gamma da diverse galassie Seyfert "radio-quiete" basata sui dati *Fermi*/LAT. In tali sistemi, la luminosità di Eddington è inferiore a 0,1 e è probabile che si verifichi un flusso di accrescimento ad elevata temperatura. L'analisi dei dati dal telescopio *Fermi* è stata confrontata con il modello di flusso ad alta temperatura che attualmente descrive al meglio tali sistemi. Ho esplorato la dipendenza della luminosità dei raggi gamma dal tasso di accrescimento, dalla rotazione, dall'intensità del campo magnetico nelle vicinanze del buco nero. I risultati ottenuti pongono alcuni vincoli interessanti su alcuni dei parametri cruciali del sistema contenente un buco nero.

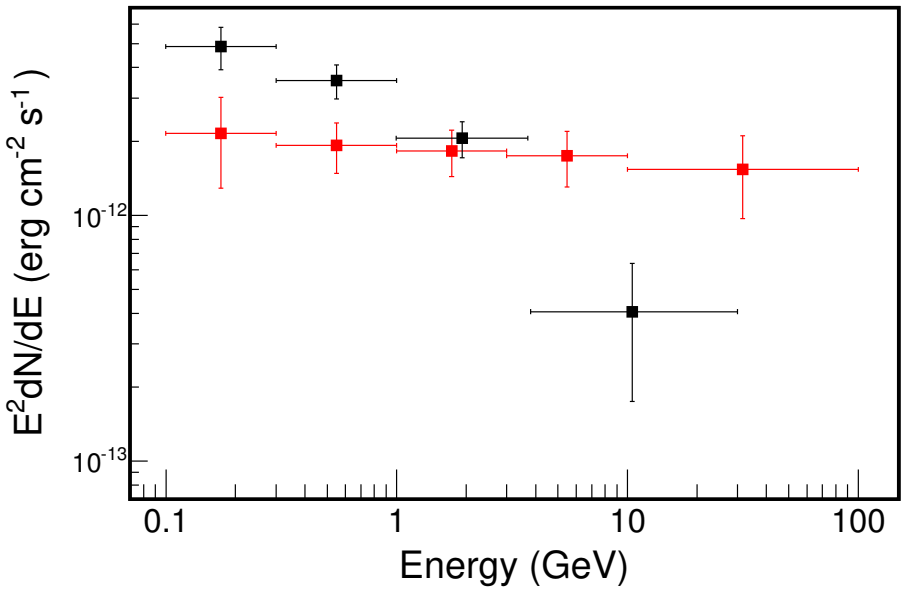

Figure 2: SED per i set di dati gamma risolti in corrispondenza del flusso in raggi X, simile a Figura 5.2, ma per L5 (nero) e H5 (rosso), (vedi Sezione 5.3).

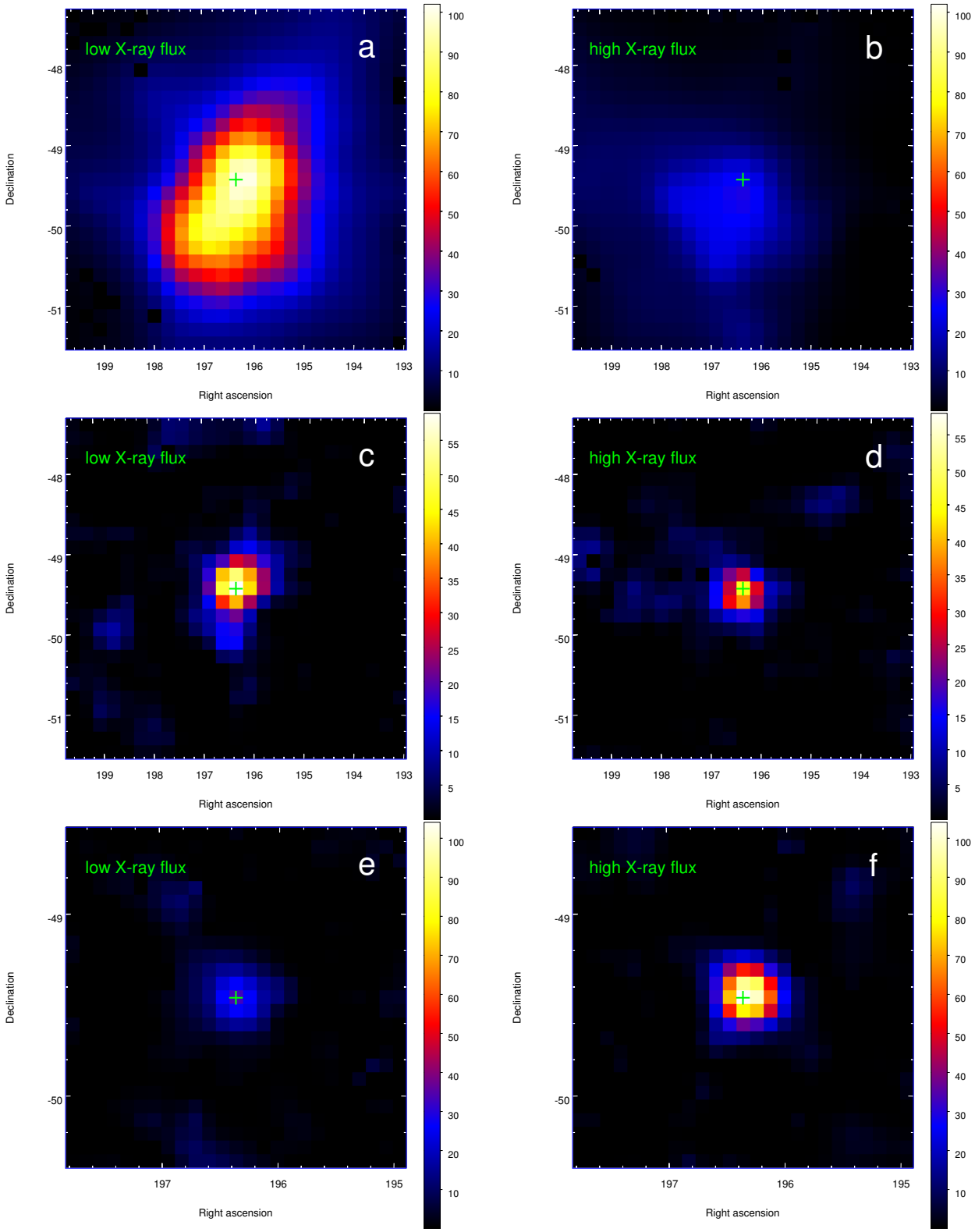

Figure 3: Mappe TS per la regione intorno a NGC 4945 create utilizzando gli eventi rivelati durante i livelli di flusso di raggi bassi (dataset L; left maps) e alti (dataset H; right maps). Le mappe principali sono per eventi con $E < 1$ GeV con una dimensione in pixel di 0.17°; le mappe intermedie sono per eventi con E tra 1 e 3 GeV con una dimensione in pixel di 0.17°; le mappe di fondo sono per eventi con $E > 3$ GeV con una dimensione in pixel di 0.075°. In tutti i pannelli la croce verde mostra la posizione di NGC 4945. In tutti i pannelli, le sorgenti 3FGL sono state sottratte dalle mappe (ad eccezione di 3FGL J1305.4-4926 che è la controparte γ di questa galassia), (vedi Sezione 5.3).

La seconda parte del lavoro ha comportato l'analisi della correlazione tra i diversi livelli di flusso in banda X e il corrispondente flusso di raggi gamma da parte della galassia di tipo Seyfert 2 denominata NGC 4945 Seyfert 2. Essa presenta simultaneamente un nucleo galattico attivo ed una forte attività di formazione stellare per cui l'origine di una significativa emissione di raggi gamma non è ancora chiara. La correlazione scoperta in questa tesi implica che l'emissione di raggi gamma dipende fortemente dall'emissione di raggi X e suggerisce che la creazione dei raggi gamma avvenga in prossimità del nucleo attivo che è esattamente quanto previsto nei modelli a flusso ad alta temperatura.

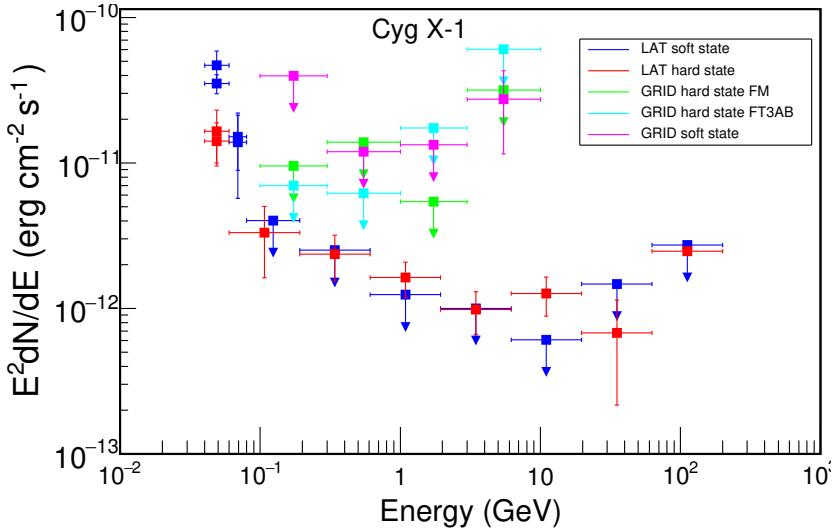

Figure 4: *AGILE*/GRID UL per il flusso di energia, calcolato con il modello L, confrontato con le misurazioni LAT di Zdziarski *et al.* (2017). I dati GRID per lo stato soft sono stati calcolati con il filtro FM, il filtro FT3AB fornisce risultati simili. Dati LAT gentilmente forniti da Andrzej Zdziarski, (vedi Sezione 6.4).

La terza parte consiste in una breve analisi delle osservazioni effettuate dal telescopio *AGILE*/GRID del sistema galattico binario denominato Cyg X-1 contenente un buco nero. È anche probabile che si verifichi un flusso di accrescimento ad alta temperatura con emissione significativa di raggi gamma durante gli stati cosiddetti "duri" presenti di in tali sistemi binari. Nonostante il set di dati due volte più esteso temporalmente la presente ricerca non è stata in grado di confermare in modo significativo dal punto di vista statistico il segnale gamma da parte di Cyg-X1 né sul totale delle osservazioni né nello stato "duro" di Cyg X-1. Infine la tesi discute la possibile spiegazione di tale fenomeno nel contesto dei due telescopi per raggi gamma *Fermi*/LAT e *AGILE*/GRID.

Contents

List of Figures

List of Tables

Chapter 1

Introduction

Black-hole accretion is a fundamental astrophysical process, powering active galactic nuclei (AGNs) as well as black hole X-ray binaries (BHBs)[1]. These objects have been extensively studied for several decades, which led to understanding that the nature of accretion flows changes at bolometric luminosities of about 10% of the Eddington limit (defined below) in both AGNs and BHBs. At higher luminosities, accretion proceeds through an optically thick disc, whose thermal emission dominates the radiative output. Depending on the mass of the central black hole and the accretion rate, the temperature of such a disc is in the range $\sim 10^4$ – 10^7 K. Lower-luminosity systems are supposed to be powered by optically thin, hot flows with electron temperature of $\sim 10^9$ K and the energy spectra of these less luminous objects are dominated by hard X-ray radiation.

Theoretical models of hot accretion flows in general predict production of γ-rays. In particular, large proton temperatures, $\sim 10^{12}$ K close to the black hole, are predicted in such models. At such temperatures, the thermal energies of protons exceed the pion production threshold, leading to emission of π^0-decay γ-rays. Observational evidence of this emission, confirming our current understanding of accretion physics, would be of major importance.

On the observational side, a large amount of information has become available in the past decade with the sensitive γ-ray data continually provided by the *Fermi* and *AGILE* satellites. However, γ-ray properties of radio-quiet black-hole systems are still rather poorly known.

These open questions motivated the research presented in this PhD thesis. In this introductory Chapter I briefly review some observational properties of accreting black holes, which are relevant for my study, and basic concepts for their interpretation. In Chapter 2 I describe two γ-ray instruments, *Fermi*/LAT and *AGILE*/GRID, providing data used for my study. Chapter 3 presents a brief overview of hot flow models. Then, using a precise computational model, developed in earlier works, I investigate the γ-ray emission resulting from proton-proton interactions, thoroughly exploring the dependence of the γ-ray luminosity on the accretion rate, the black hole spin, the magnetic field strength, the electron heating efficiency, and the particle distribution. Chapter 4 presents the results of my analysis of *Fermi*/LAT observations of several nearby Seyfert galaxies and their comparison with the hadronic γ-ray luminosities predicted by the hot flow model. In Chapters 5 and 6 I consider two objects: a nearby galaxy hosting an active supermassive black hole at its center, and a galactic binary system including a stellar-mass black hole. Both systems have

[1] most likely, it also powers γ-ray bursts, which are not considered in this thesis

low luminosities in the sense that they are slightly below (although close to) the limiting value of 10% of the Eddington limit. In particular Chapter 5 presents my analysis of the γ-ray loud galaxy NGC 4945, which harbors both an active galactic nucleus and a nuclear starburst region. The X/γ-ray correlation found in my analysis indicates that the γ-ray production is dominated by the active nucleus rather than by cosmic rays interacting with the interstellar medium. Chapter 6 presents my analysis of the *AGILE*/GRID data for Cyg X-1. Summary of my results is presented in Chapter 7.

My original results presented in Chapters 3 and 4 were published in:

Wojaczyński, R., Niedźwiecki, A., Xie, F.-G. & Szanecki, M. Gamma-ray activity of Seyfert galaxies and constraints on hot accretion flows. *Astronomy and Astrophysics* **584,** A20 (Dec. 2015), referred to in this thesis as Paper 1, except for the extended to 9 years analysis of LAT observations of NGC 4151, which has not been published yet. Results presented in Chapter 5 were published in:

Wojaczyński, R. & Niedźwiecki, A. The X-/γ-Ray Correlation in NGC 4945 and the Nature of Its γ-Ray Source. *Astrophysical Journal* **849,** 97 (Nov. 2017), referred to in this thesis as Paper 2.

My analysis of GRID observations of Cyg X-1 has not been published.

1.1 Accreting black holes

Astronomical observations indicate the presence of two populations of black holes in the Universe: stellar-mass black holes with masses in the range of $\sim 5M_\odot$ to $30M_\odot$, and supermassive black holes with masses in the range of $\sim 10^6 M_\odot$ to $10^{10} M_\odot$, where $M_\odot$ is the mass of the Sun. A distinct class of black holes with intermediate mass may also exist. I do not consider them in my thesis, so I only briefly note that main candidates for such objects are the ultraluminous X-ray sources, observed in external galaxies with luminosities exceeding the Eddington luminosity for a $10M_\odot$ black hole by a factor of $\sim 100-1000$; however, neither of these cases has been directly confirmed due to difficulties with dynamical measurement of the black hole mass. Recently, gravitational-wave detectors provided the first evidence for the formation of relatively massive black holes in merging events (e.g. Abbott *et al.*, 2016), but still less massive than $\sim 100M_\odot$.

An astrophysical black hole is fully characterized by two parameters, its mass, M, and angular momentum, J. The latter is conveniently described by the dimensionless spin parameter ranging from 0 to 1,

$$a = \frac{J}{cR_\mathrm{g}M}, \tag{1.1}$$

where

$$R_\mathrm{g} = \frac{GM}{c^2} \tag{1.2}$$

is the gravitational radius.

Accretion onto black holes can produce large luminosities by converting a significant amount of the released potential energy into radiation. A characteristic luminosity for this process is the Eddington limit, at which the outward radiative pressure is balanced by the inward gravitational attraction of the central mass M (assuming that the accreting material is fully ionized hydrogen

and its opacity is provided by Thomson scattering):

$$L_{\rm Edd} = \frac{4\pi G M m_{\rm p} c}{\sigma_{\rm T}} \simeq 1.3 \times 10^{38} \frac{M}{M_\odot} \ {\rm erg \ s^{-1}}, \tag{1.3}$$

where m_p is the mass of the proton and $\sigma_{\rm T}$ is the Thomson cross-section for electron scattering.

Since bolometric luminosity of a spherical object cannot exceed $L_{\rm Edd}$, luminosities of bright quasars of $\sim 10^{46}$ erg s^{-1} require the presence of supermassive black holes with $M > 10^8 M_\odot$. The nuclei of nearby galaxies usually have low accretion luminosities and hence are faint sources, enabling spectroscopic observations relatively close to the central black hole. Then, masses of supermassive black holes in these nearby nuclei can be measured with dynamical methods. Mapping of the trajectories of stars orbiting the nucleus of Milky Way Galaxy provides evidence for presence of a black-hole with $(4.4\pm0.4)\times10^6 M_\odot$ (Meyer *et al.*, 2012). Precise measurements of the mass are also allowed in several galaxies by radio observations of maser emission (from transitions of the water molecule), with the most spectacular case of the galaxy NGC 4258, where a perfect Keplerian profile around the nucleus was determined giving the black hole mass of $(4.00\pm0.09)\times10^7 M_\odot$ (e.g. Humphreys *et al.*, 2013).

Several tens of black hole masses have been measured by dynamical modeling of the spatially resolved stellar or gas kinematics observed with high spatial resolution by the Hubble Space Telescope (e.g. Kormendy & Ho, 2013). These observations have shown that nucleus of essentially every galaxy hosts a supermassive black hole.

Radiative properties of accreting black holes seem to depend on the accretion rate scaled by the Eddington value and determination of the black hole mass is crucial for their studies. Then, I note that other, less direct (and less precise), methods for measuring M include reverberation mapping (Peterson *et al.*, 2004), and an empirical correlation between the supermassive black hole mass and the stellar velocity dispersion of the bulge (or its luminosity) of their host galaxies (e.g. Ferrarese & Merritt, 2000; Gebhardt *et al.*, 2000). Feedback of supermassive black holes on their host galaxies during the formation of both entities, implied by these correlations, is a subject of intense studies (e.g. Di Matteo *et al.*, 2005; King, 2005).

All known stellar-mass black holes candidates are located in X-ray binary systems. Identification of the compact component of the binary as a black hole relies on the comparison of its mass with the maximum stable mass of a neutron star, which is less than $\simeq 3M_\odot$. In ten X-ray binaries, optical spectroscopic observations of the companion star constrain the compact object mass to be larger than $\sim (3-8)M_\odot$, allowing for black hole identifications. In the remaining cases such identification requires additional estimation of the binary mass ratio and inclination angle, which gives robust results for about 15 more systems (a review of these results is given, e.g., by Casares & Jonker, 2014).

The second black hole parameter, a, is much more difficult to measure because its effects are significant only close to the black hole, at $R \lesssim 10R_{\rm g}$. Applied methods include modeling the profile of the relativistically distorted fluorescence Fe Kα line, observed in some objects (e.g. Tanaka *et al.*, 1995; Reynolds, 2014) and fitting the thermal continuum spectrum in the soft spectral states to the optically thick disc model (e.g. McClintock *et al.*, 2014). These results are, however, model dependent. In particular they rely on the assumption that the inner edge of the disc is at the

innermost stable circular orbit, which has the radius dependent on a.

1.2 X-ray black-hole binaries

Most of my research is focused on AGNs, however, I start with a brief review of the studies of BHBs, where better quality data give us a more complete view of the inner regions of the accretion flow.

The first discovered black hole candidate in a binary system was Cyg X-1, which was noted in the early stages of X-ray astronomy as a bright X-ray source (Bowyer *et al.*, 1965), and for which dynamical observations indicated a mass of at least several solar masses (Paczynski, 1974), making it too massive to be a neutron star. Over 20 more stellar black holes were discovered since then. Depending on the donor mass, the X-ray binaries are classified as either low mass X-ray binaries (LMXBs) fueled by a $\sim 1 M_{\odot}$ Roche-lobe filling star, or high mass X-ray binaries (HMXBs), fueled from the wind of a $\gtrsim 10 M_{\odot}$ companion (e.g. van Paradijs, 1998).

Five black holes have been identified in HMXBs, including Cyg X-1, three systems in nearby galaxies (LMC X-1, LMC X-3, M33 X-7) and the recently discovered MWC 656. Except for the last one, these systems are persistent and radiate at a significant fraction of their Eddington limits. MWC 656 is the first HMXB observed in a quiescent state (i.e. with a very low luminosity $< 10^{-7} L_{\rm Edd}$, Munar-Adrover *et al.*, 2014); interestingly for the subject of this thesis, its discovery was triggered by the γ-ray detection with *AGILE*, noted in Section 1.4.

All the remaining known BHBs are LMXBs, which are in general transient systems, spending most of the time in their quiescent state (in which they are typically not observable in the X-ray band). Their outbursts, driven by thermal-viscous instabilities (e.g. Lasota *et al.*, 2016) occur with recurrence times ranging from months to decades, and last typically from several days to several months. A remarkable exception to that is GRS 1915+105, whose outburst started in 1992 and is still ongoing; in this system the Roche lobe overflow occurs in a much wider binary than in other LMXBs and the large disc structure contains enough material to maintain large accretion rates over time-scales of tens of years (e.g. Done *et al.*, 2004).

Two main spectral states, hard and soft states, were originally identified in the persistent system Cyg X-1 (Tananbaum *et al.*, 1972), and more states were defined by studies of transient systems (e.g. Miyamoto *et al.*, 1992; Belloni *et al.*, 1996), in which an outburst evolution, with luminosity varying by several orders of magnitude, is characterized by strong changes of spectral properties. Apart from these spectral changes, fast X-ray variability properties, extensively explored with observations of the *RossiXTE* satellite, are important for identification of the source states (e.g. Remillard & McClintock, 2006). Also jets observed in BHBs exhibit a clear correlation with the spectral state (e.g. Fender *et al.*, 2004). Below I note spectral X-ray characteristics for the two main states.

The soft state is typically observed at high bolometric luminosities, approaching the Eddington limit, and its energy spectrum is dominated by a thermal disc component, with an inner temperature of the order of 1 keV, extending to radii close to the BH. At high energies, an additional weak hard component is observed, whose origin is not well understood. The hard state is observed at lower bolometric luminosities, $\lesssim 0.1 L_{\rm Edd}$ (the exact luminosity of state transition may deviate

by a factor of several even in the same object). In transient systems, the hard state occurs at the beginning and at the end of outbursts and continues into the quiescent state. Its energy spectrum is dominated by a hard component which can be roughly approximated with a power law with a photon spectral index between ~ 1.5 and 2, extending up to ~ 100 keV. An excellent agreement of this component with thermal Comptonization indicates this process, in a mildly relativistic thermal electron plasma, to be the dominant one in the hard state (e.g. Zdziarski & Gierliński, 2004; Burke *et al.*, 2017: and references therein).

The widely accepted model (e.g. Esin *et al.*, 1997; Done *et al.*, 2007) for the above involves a cold accretion disc which is truncated in the quiescent and hard state and replaced in the inner part by a hot optically-thin flow, where most of the accretion power is released. This flow also acts as the launching site of the jet. Models of such flows are discussed in Chapter 3. Increase of the mass accretion rate decreases the disc truncation radius, leading to softer spectra and a faster jet, until the disc extends down to the last stable orbit, which gives the hard to soft spectral transitions.

1.3 Active galactic nuclei

The term active galactic nucleus refers to energetic phenomena in the nuclei of galaxies, which cannot be attributed to stars. Historically, two major classes of AGNs, Seyfert galaxies and quasars, were independently discovered, but now they are commonly regarded as different manifestations of the same basic phenomena (i.e. powered by black hole accretion) with the main difference concerning the amount of radiation emitted by the nucleus. In the case of a typical Seyfert galaxy, the total energy emitted by the nuclear source is comparable to the energy emitted by all stars in the galaxy, whereas in a typical quasar the nuclear source is brighter by over a factor of 100 than the stars.

A reach phenomenology revealed by AGN observations, with division of these objects into a number of subclasses, can be largely systematized within unification schemes presented, e.g., in Padovani & Urry (1992), Antonucci (1993), Urry & Padovani (1995), Urry (2003), Padovani *et al.* (2017). Two major classes of AGNs involve radio-loud ($\sim 10\%$ of all AGNs) and radio-quiet ($\sim 90\%$) objects. The main difference between them can be explained by the presence (in the former) or absence (in the latter) of relativistic jet structures, where radio emission is produced by synchrotron process. Other apparent differences can be explained by orientation effects and the presence of a dust torus obscuring the central region in systems observed from a side, which explains differences between type 1 (observed face-on; e.g. Seyfert 1 galaxies, broad line radio galaxies) and type 2 (observed edge-on; e.g. Seyfert 2 galaxies, narrow line radio galaxies) AGNs. An even more spectacular orientation effect concerns the radio-loud AGNs, which are observed as radio galaxies at large angles with respect to the jet direction, while those observed along the jet direction are observed as blazars. In the latter the observed radiation is dominated by emission from the jet which is beamed towards observer and Doppler boosted.

Although jet-powered sources are not the main subject of my thesis, these sources are the main class of objects observed at γ-ray energies. Then, I briefly note that blazars were first identified by optical observations as sources that exhibit violent variability and high polarization. Later studies have shown that superluminal motion at radio frequencies and highly luminous and variable γ-ray

emission are also typical properties of blazars. Their spectral energy distribution shows two characteristic bumps; the first - peaking between IR an UV - attributed to synchrotron emission, and the second - peaking in X-rays or γ-rays - explained with inverse Compton mechanism. Blazars are divided into 2 classes, flat spectrum radio quasars (FSRQ) showing broad emission lines and BL Lacs with no strong spectral lines, whose parent (misaligned) populations are recognized as Fanaroff & Riley (FR) type-II and type-I, respectively, radio galaxies. The latter, i.e. BL Lacs and FR Is are often supposed to be power by low luminosity (and radiatively inefficient) accretion flows, while FSRQs and FR IIs are linked with luminous discs (e.g. Ghisellini *et al.*, 2011).

AGNs radiating at large Eddington ratios do not possess properties directly corresponding to soft spectral states of BHBs, as discussed e.g. by Done (2014). On the other hand, low luminosity AGNs, including normal Seyfert galaxies and even lower luminosity nuclei, often identified as LINERs (low-ionization nuclear emission-line regions), seem to be the direct analogue of the hard state of BHBs. They do not show strong blue bumps indicating a dominating contribution of thermal disc emission or relativistic reflection features indicating an optically thick disc extending close to the black hole. The accuracy of hard X-ray/soft γ-ray spectra measured from these AGNs is lower than that for X-ray binaries. Still, high-energy cutoffs compatible with thermal Comptonization are commonly observed, e.g., Zdziarski *et al.* (1996), Gondek *et al.* (1996), Zdziarski *et al.* (2000), Lubiński *et al.* (2016). Overall, these low luminosity AGNs are likely explained by hot inner flows with radiative properties consistent with those found in the hard states of BHBs.

1.4 Black-hole systems in γ-rays

Blazars were established as a γ-ray loud class of AGNs already by *CGRO*/EGRET. Apart from unidentified sources, the only other extragalactic source observed by this detector was the nearby radio galaxy Centaurus A. Blazars are also a main class of objects seen by *Fermi*/LAT. The third catalog of AGNs detected by LAT (3LAC Ackermann *et al.*, 2015) reports about 1600 AGNs, 98% of which are blazars (evenly split between FSRQs and BL Lacs). In some blazars their γ-ray emission reaches TeV energies and is observed by ground-based detectors. LAT discovered also new (but less numerous, each including several objects) classes of γ-ray loud AGNs, which include narrow and broad line radio galaxies as well as radio-loud narrow-line Seyfert 1. In all these sources, their γ-rays are attributed to emission from a jet. Then, these LAT findings contribute mostly to studies of the relativistic jet physics.

LAT observed also γ-rays from cosmic-ray processes in starburst but also in normal galaxies (Ackermann *et al.*, 2012a; Ackermann *et al.*, 2016; Ackermann *et al.*, 2017). Searches for GeV γ-rays from radio-quiet AGNs in general did not reveal any signals except for the three radio-quiet Seyert 2 galaxies, NGC 4945, NGC 1068 and Circinus (Lenain *et al.*, 2010; Ackermann *et al.*, 2012a; Hayashida *et al.*, 2013), which are however also starburst galaxies and their γ-ray emission can be attributed to cosmic-ray processes. My studies presented in Chapters 4 and 5 contribute mostly to this area of research.

Two HMXBs powered by accretion were observed in γ-rays. The first one is Cyg X-3 (Fermi LAT Collaboration *et al.*, 2009; Tavani *et al.*, 2009a), where the γ-rays may be produced by Compton up-scattering of the stellar emission from the companion Wolf-Rayet star by relativistic

electrons in the jet (Dubus *et al.*, 2010). The nature of its compact object is, however, uncertain, as its mass of $\sim 2.5 M_\odot$ allows either a neutron star or a low-mass black hole (e.g. Zdziarski *et al.*, 2013). The other, much weaker in γ-rays, is Cyg X-1. An 8σ source at its position is reported in the recent LAT list of sources (FL8Y; see Section 2.3.5), while it was not listed in any previous LAT catalog. This γ-ray signal was found to indeed come from Cyg X-1 by Zanin *et al.* (2016) and Zdziarski *et al.* (2017) and it was also attributed to a jet (Chapter 6).

In 2010, *AGILE* detected a γ-ray point-like source, AGL J2241+4454, with a significant excess above 5σ (Lucarelli *et al.*, 2010). Searches of its possible counterpart have led to the discovery of a quiescent black hole HMXB, MWC 656 (Munar-Adrover *et al.*, 2014). This source was not detected with *Fermi*/LAT (Alexander & McSwain, 2015) but recently it was reported to show recurrent activity in *AGILE* by Munar-Adrover *et al.* (2016), who also discuss this apparent discrepancy between *AGILE* and *Fermi*.

A 4σ significance flare was reported also from a black hole LMXB, V404 Cyg, (Loh *et al.*, 2016).

1.5 Notation

Throughout the thesis I use the following dimensionless parameters. Luminosities are scaled by $L_{\rm Edd}$, given by equation (1.3) and given as the Eddington ratio denoted by λ. Subscript indicate the energy range, for example, $\lambda_{2-10\,\rm keV} = L_{2-10\,\rm keV}/L_{\rm Edd}$ and $\lambda_{1-10\,\rm GeV} = L_{1-10\,\rm GeV}/L_{\rm Edd}$, where $L_{2-10\,\rm keV}$ and $L_{1-10\,\rm GeV}$ are the luminosities in the 2–10 keV and 1–10 GeV. If the energy range is not indicated by the subscript, the bolometric luminosity is meant.

The accretion rate in the unit of mass per unit time is denoted by $\dot{M}$ and the dimensionless accretion rate is $\dot{m} = \dot{M}/\dot{M}_{\rm Edd}$, where $\dot{M}_{\rm Edd} = L_{\rm Edd}/c^2$. Distance in the physical units is denoted by R and the distance scaled by the gravitational radius is $r = R/R_{\rm g}$, where $R_{\rm g} = GM/c^2$.

Finally, two phenomenological parameters are used two describe magnetohydrodynamical (MHD) processes in accretion flows. The ratio of the gas pressure (electron and proton) to the magnetic pressure is denoted by β. The fraction of the dissipated energy that directly heats electrons is denoted by δ.

Chapter 2

γ-ray detectors

2.1 Detection techniques

γ-rays cannot be reflected or focused because they have too short wavelengths. Then, they have to be detected through their interaction products. The efficiency of different modes of interaction of γ-rays strongly depends on the atomic number of the target material, but in general Compton scattering dominates over photo-electric absorption at energies larger than 1 MeV and pair production dominates over Compton scattering above $\sim$ (10 – 20) MeV. This determines the energy range for detectors measuring products of the Compton and pair-production processes. At the same time, the atmosphere is opaque to γ-rays and, then, their direct measurements require space-based experiments. Yet another aspect concerns the measured fluxes of cosmic γ-rays, which rapidly decrease towards high energies. Then, detections at higher energies require larger effective areas (given by the product of the geometrical area and the detector efficiency). However, the geometrical area cannot exceed $\sim$ 1 m^2 due to the cost of space technology, so at very high energies (of tens of GeV) the space-based detectors become inefficient. At these very high energies ground-based techniques become more appropriate, as for energies above $\sim$ 20 GeV the electromagnetic air showers induced by γ-rays in the atmosphere become detectable. The shower can be detected either through observation of Cherenkov radiation of the particles in air (the Cherenkov technique) or by directly detecting the charged particles reaching ground (the extensive air shower technique).

Figure 2.1 shows the sensitivity of some of the past, current and planned γ-ray detectors. The first attempts to detect cosmic γ-rays undertaken in the early 1960s with balloon-borne detectors failed due to strong background of secondary γ-rays produced by cosmic rays in the atmosphere. The first detections were then provided by γ-ray satellites in late the 1960s. In particular, OSO-3 satellite in 1968 detected the first photons with energies above 100 MeV from the Milky Way. Two later γ-ray satellites, SAS-2 operating in 1972-1973 and COS-B operating between 1975 and 1982, revealed the diffuse emission of the Galaxy, discovered the Crab and Vela pulsars and the first extragalactic γ-ray source, quasar 3C273.

The Compton Gamma-ray Observatory (*CGRO*), taking data from 1991 until 2000, comprised four instruments including the Imaging Compton Telescope (COMPTEL) and the Energetic Gamma Ray Experiment Telescope (EGRET). The final catalog of EGRET, the pair-production

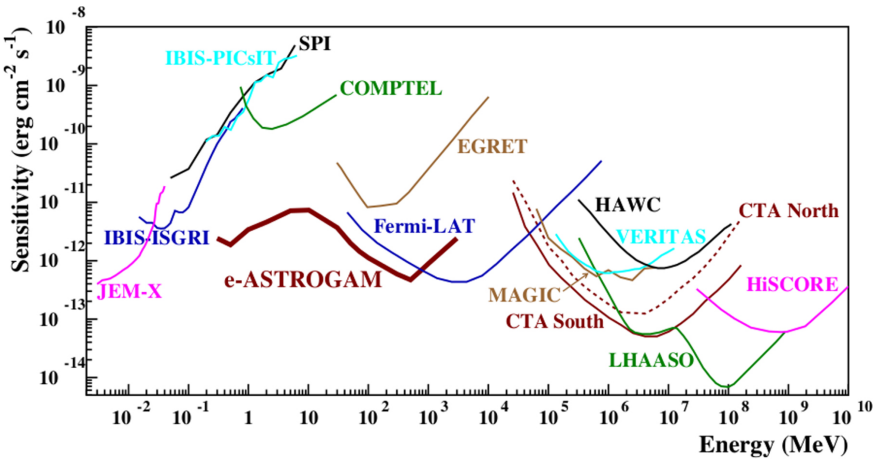

Figure 2.1: Differential sensitivity of hard X-ray and γ-ray instruments; the following observation times were assumed: COMPTEL and EGRET 9 years, *Fermi*/LAT 10 years in survey mode, MAGIC, VERITAS, HESS and CTA 50h, HAWC 5 years, LHAASO 1year, HiSCORE 1000h, e-ASTROGAM 1 year 3σ prediction; adopted from De Angelis *et al.* (2017).

telescope, reports 271 sources, including many AGNs. The current generation of space-based detectors, *AGILE* (Astrorivelatore Gamma a Immagini LEggero) and *Fermi*, started operating a decade ago (Tavani *et al.*, 2009b; Atwood *et al.*, 2009).

Ground-based detectors can measure γ-rays in the GeV and TeV range. The first Imaging Atmospheric Cherenkov Telescope, Whipple constructed in Arizona, discovered the first TeV emitter, i.e. the Crab Nebula, in 1989. Imaging analysis allowed by this instrument was crucial for rejection of background from charged particles using the Hillas parameters method (Hillas, 1985), which is applied also in the current generation of imaging telescopes including H.E.S.S. in Namibia, MAGIC in the Canary Islands and VERITAS in Arizona. A major problem for this technique is that clear and almost dark nights are required for observations due to the faintness of the Cherenkov light. As a consequence, the Cherenkov telescopes are characterized by a low duty cycle of about 15%.

Finally, the extensive air shower technique observes the shower particles reaching ground by detecting the Cherenkov light produced by the secondary particles of the shower entering the water pool equipped with photomultipliers. The currently operating HAWC observatory located at an altitude of 4100 m a.s.l. in Mexico, using this technique, was completed in 2015.

Two particularly interesting of the future instruments shown in Figure 2.1 are the next generation of Imaging Cherenkov detectors, i.e. Cherenkov Telescope Array (Actis *et al.*, 2011) and e-ASTROGAM (De Angelis *et al.*, 2017). The latter, planned for the launch in about 10 years, will be a dual detector using both the Compton scattering and the pair-production effects (with the latter channel optimized for lower energies). Its planned sensitivity will improve that of COMPTEL by over two orders of magnitude and that of *Fermi*/LAT below 1 GeV by over an order of magnitude.

In my study I used data from pair-production telescopes. Below I briefly describe this technique and the somewhat related Compton technique.

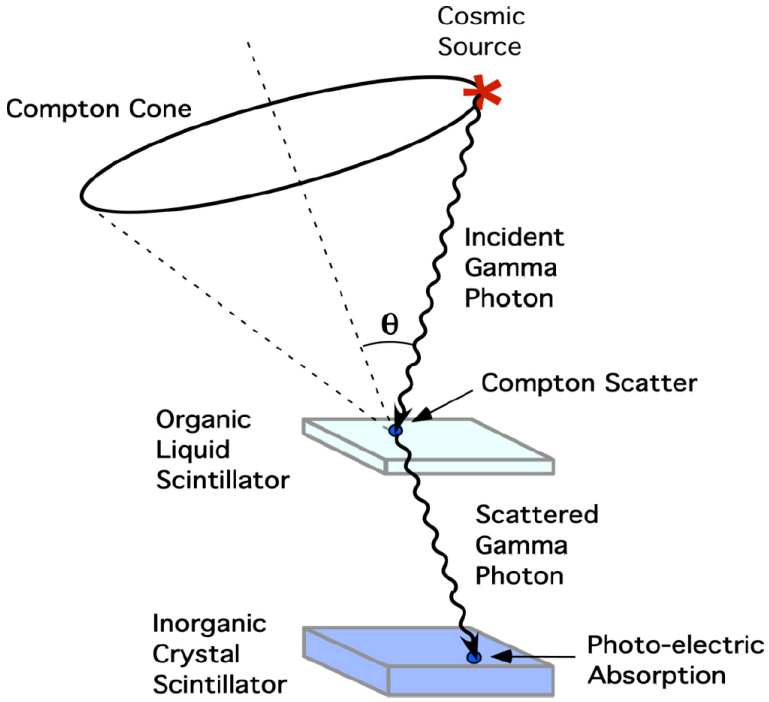

Figure 2.2: Schema of a Compton telescope, adopted from presentation of COMPTEL[1]

2.1.1 Compton technique

Compton scattering is the dominant physical process for interaction of photons with energies in the range from $\sim$ 1 to $\sim$ 20 MeV. Measurement of the direction and energy of an incident γ-ray requires two photon interactions, because the scattered photon carries information about the incident photon. Compton telescopes then include two sub-detectors, a tracker where the Compton scattering occurs, creating an electron and a scattered photon, and a calorimeter, where the energy and absorption position of the scattered photon are measured. The basic principle of the technique is illustrated in Figure 2.2. If only quantities measured in the calorimeter are available, the initial direction can be constrained only to the Compton cone shown in the figure. For photons with energies exceeding a few MeV, measurement of the track of the scattered electron is possible, providing information needed for improved event reconstruction and then reducing the uncertainty in the source localization.

Then, COMPTEL, the first Compton telescope, had 2 layers of scintillator detectors, as seen in Figure 2.2. The first layer consists of low-Z material that allows photon to pass through, and where the actual scattering takes place. After passing the first layer, scattered photon travels down in detector into second layer (1.6 m from the first layer in COMPTEL) where it is completely absorbed via photoelectric effect in inorganic crystal scintillator. In order the photon to be classified as a valid photon it should be recorded almost simultaneously in both layers. In COMPTEL photon should travel the distance between layers in time below 5 ns. This maximum allowed time is called time-of-flight. If time-of-flight is greater than 5 ns the event is rejected.

[1] http://spie.org/newsroom/1058-new-materials-advance-gamma-ray-telescopes?SSO=1

Mission	Duration	Effective area at ≈200 MeV	Angular resolution	Field of view	Energy range	Sky coverage
SAS-2	Nov 1972 - Jun 1973	90 cm^2	≈ 2.5° at 100 MeV ≈ 1.5° at 1 GeV	0.4 sr	35 MeV - 1 GeV	55 %
COS-B	Aug 1975 - Apr 1982	45 cm^2	≈ 3.7° at 100 MeV ≈ 1.2° at 1 GeV	0.4 sr	50 MeV - 5 GeV	60 %
EGRET/CGRO	Apr 1991 - 2000	1300 cm^2	≈ 5.5° at 100 MeV ≈ 1.3° at 1 GeV	0.6 sr	20 MeV –30 GeV	100 %
AGILE/GRID	2007-now	600 cm^2	≈ 3.5° at 100 MeV ≈ 0.6° at 1 GeV	3 sr	30 MeV –30 GeV	100 %
Fermi/LAT	2008-now	5000 cm^2	< 3.5° at 100 MeV ≈ 0.6° at 1 GeV	2.4 sr	30 MeV– 300 GeV	100 %

Table 2.1: Past and present pair production telescopes, Schonfelder & Kanbach (2013), SAS-2: Fichtel *et al.* (1975), COS-B[2], *EGRET*/CGRO: Kanbach *et al.* (1988), *AGILE*/GRID: Tavani *et al.* (2009b), *Fermi*/LAT: Atwood *et al.* (2009).

2.1.2 Pair-production technique

Electron-positron pair production dominates the interaction with matter of photons with energies above $\sim$ 20 MeV. Similarly to Compton telescopes, a pair-production telescope contains two main sub-detectors, a converter-tracker and a calorimeter. The converter-tracker contains a material in which a γ-ray can convert to an e^+e^- pair. The converter planes are interleaved with position-sensitive detectors that record the passage of charged particles, thus measuring the tracks of the particles resulting from pair conversion. The calorimeter then measures the energy deposition due to particles produced in the converter. This above information, i.e. the recorded tracks and energy deposition, is used to reconstruct the direction and energy of the incident photon.

Construction of the converter requires a compromise between increasing the effective area and degrading the angular resolution. The effective area depends on the fraction of converted γ-rays, which increases with the amount of material. However, a larger amount of material increases the number of multiple Coulomb scattering of the e^+ and e^-, which is the main effect limiting the angular resolution.

The pair-production telescope contains a detector layer on the top, where photon enters and interact with material, and some kind of chamber filled with gas on the bottom. Such chamber or a tracker is used to measure direction of created pair or further secondary particles. Since the cross section changes with Z^2 usually high-Z materials are used e.g. heavy metals like lead (Pb). After electron and positron are created they travel down the detector and further are ionizing the gas in spark chamber. This trail of sparks in spark chamber can finally provide three dimensional picture of electron and positron traversing through chamber.

More sophisticated design consists of interleaved layers of converter planes placed between detector layers like silicon planes. In that sense they are forming repetitive structure, one on the other, creating an independent tracker unit. There could be a several of such units to maximize

[2] http://sci.esa.int/cos-b/36277-cos-b-gamma-ray-detector-parameters/

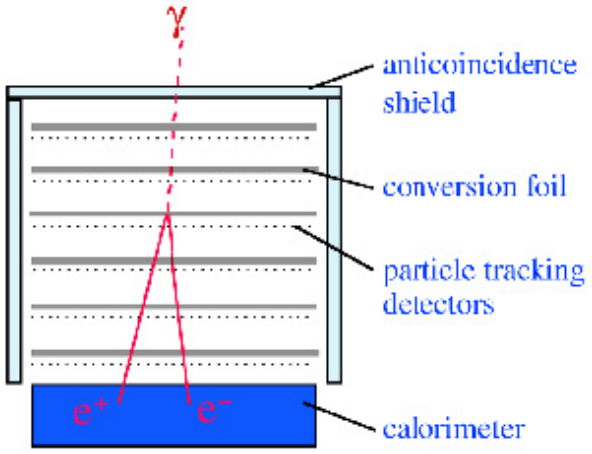

Figure 2.3: Pair-production telescope, adopted from the presentation of LAT[3]

efficiency of detection. They allow to measure direction of secondary particles with greater precision. This type of design (based on calorimeter shown in Figure 2.3) is used in modern pair production telescopes like *Fermi*/LAT or *AGILE*/GRID which are currently operating. Basic properties of these telescopes along with historical ones are presented in Table 2.1. The last condition that need to be satisfied, is the ability of detector to identify and to reject background radiation like cosmic-rays. More than 99.9% of events with energies above 30 MeV are cosmic-rays. To avoid such number of not relevant events, special anti-coincidence shields are constructed, to protect detector planes and tracker.

2.2 The likelihood analysis of γ-ray data

Statistical techniques are required for analysis of data from γ-ray detectors due to their low detection rates and large extents of their point spread functions. The likelihood analysis, proposed for photon-counting experiments by Cash (1979), has become the prevailing method in this area. It has been used, e.g., with the COMPTEL and EGRET data (Schoenfelder *et al.*, 1993; Mattox *et al.*, 1996) and currently it is applied in both the *Fermi* and *AGILE* analysis, as described below. The "likelihood" was introduced by Fisher (1925) to quantify the support in the observed data for a given hypothesis. The likelihood ratio test used for hypothesis testing (Neyman & Pearson, 1928) has a convenient interpretation provided by the Wilks' theorem (Wilks, 1938), which allows to relate the statistical significance with the computed likelihood ratio.

In applications to γ-ray astronomy, the likelihood function, $\mathcal{L}$, gives the probability of obtaining the data with a given input model, which includes the spatial distribution of γ-ray sources, their intensities and spectra. The $\mathcal{L}$ function is constructed by binning the data set into the three-dimensional cube with two dimensions representing the spatial coordinates and one dimension representing the energy. Then, $\mathcal{L}$ is given by the product of Poisson probabilities, p_i, for detecting n_i events in bin i when the model predicts m_i (i labels energy and position in the sky):

$$\mathcal{L} = \prod p_i, \tag{2.1}$$

[3] https://www.nasa.gov/mission_pages/GLAST/multimedia/pair-production_prt.htm

where

$$p_i = \frac{{m_i}^{n_i} e^{-m_i}}{n_i!}, \tag{2.2}$$

or in a simpler form

$$\mathcal{L} = e^{-N_{\rm exp}} \prod \frac{{m_i}^{n_i}}{n_i!}, \tag{2.3}$$

where $N_{\rm exp} = \sum m_i$ is the total number of events expected in all bins. Still more convenient form is given by the logarithm of likelihood:

$$\ln \mathcal{L} = \sum n_i \ln(m_i) - \sum m_i - \sum \ln(n_i!). \tag{2.4}$$

The last term is model independent and it may be neglected for the parameter estimation or for the likelihood ratio test, then

$$\ln \mathcal{L} = \sum n_i \ln(m_i) - \sum m_i. \tag{2.5}$$

The expected number of detected counts m_i is computed by convolving the model spectra of the source and background events with the instrument response functions (IRFs). Standard numerical optimization methods are then applied to find the spectral parameters of model components which give the maximum of the likelihood function. This likelihood spectral fitting yields the best fit parameter values and their uncertainties.

The significance of a model component is quantified with the test statistic (TS). To estimate it, we calculate (and maximize with respect to the adjustable parameters) the likelihoods of the data for the model with or without a source present at a given position on the sky. The test statistic is expressed as

$$\mathrm{TS} = 2(\ln \mathcal{L}_{\rm source} - \ln \mathcal{L}_0), \tag{2.6}$$

where $\mathcal{L}_{\rm source}$ represents the likelihood with the source included in the model and $\mathcal{L}_0$ represents the likelihood of the background model.

According to the Wilks' theorem, for a large number of counts the TS is asymptotically distributed as χ^2_n, where n is the number of parameters characterizing the source. In most cases the γ-ray spectra are described by a simple power-law

$$\frac{dN}{dE} = N_0 E^{-\Gamma}, \tag{2.7}$$

with two additional parameters, the photon spectral index Γ and the normalization $\mathrm{N_0}$ related with the source intensity. Then, TS is distributed as χ^2_2 and the significance of a source detection is approximately equal to $\sqrt{\mathrm{TS}}$.

2.3 *Fermi*

The *Fermi* satellite was launched in 11 June 2008 and started delivering data on 4 August 2008. The *Fermi* mission is a continuation of the goals of *CGRO* mission in γ-ray domain. Originally named as GLAST (Gamma-ray Large Area Space Telescope) it was renamed to *Fermi*, to honor

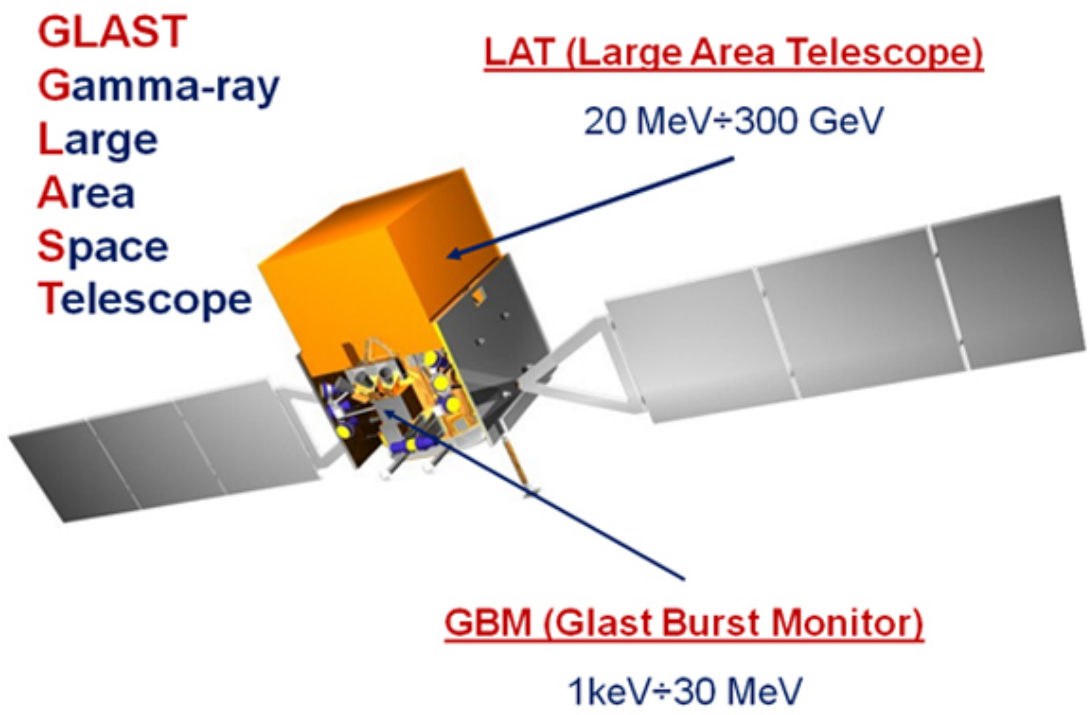

Figure 2.4: *Fermi* observatory and its instruments[4]

Enrico Fermi, just after it started providing data.

Every orbit takes 96.5 minutes at the altitude of 565 km. The orbit has an inclination of 26.5° with an eccentricity of 0.01. Collaboration that build *Fermi* is a joint venture of scientific institutions and space agencies from USA, France, Italy, Germany, Japan and Sweden. On board there are two detectors dedicated to non overlapping different wavelengths and to different scientific purposes: Gamma-ray Burst Monitor (GBM), operating in the energy range of 150 keV–30 MeV and the Large Area Telescope (LAT). The whole structure was assembled at Stanford Linear Acceleration Center, with significant parts of hardware delivered by other countries. Communication to satellite is provided by Tracking and Data Relay Satellite System around 10-11 times per day. It takes usually 7-8 minutes of direct real time telemetry contact to retrieve the data. No data is taken when *Fermi* is passing through South Atlantic Anomaly, which is an area of increased number of trapped charged particles. It results in the loss of 15% of *Fermi* observing time. The main scientific purposes of *Fermi* include: (i) monitoring variable sources and providing fast instrument response for short bursts, (ii) creating catalog of high energy sources with greater precision and sensitivity than EGRET, (iii) localizing point sources with accuracy 0.2-3 arc min, (iv) spatial investigation of nearby extended sources like pulsar wind nebulae, closest galaxies, molecular clouds, (v) studying diffuse background, (vi) potential dark matter imprints and (vii) measuring spectrum of cosmic-ray electrons.

[4] `https://www.nasa.gov/content/fermi-gamma-ray-space-telescope`

2.3.1 The *Fermi* Large Area Telescope

Large Area Telescope (hereafter LAT) on board *Fermi* satellite is the most complex and modern γ-ray telescope operating in the high energy domain i.e. between 30 MeV and $\sim$ 100 GeV (Atwood *et al.*, 2009). The principal investigator of LAT is Peter Michelson from Stanford who was awarded Bruno Rossi prize in 2011 together with the whole LAT team.

Parameter	Value or Range
Energy range	~20 MeV to >300 GeV
Effective Area	>8,000 cm^2 maximum effective area at normal incidence
Angular Resolution	< 3.5°, on-axis, 68% space angle containment radius for E = 100 MeV <0.15°, on-axis, 68% space angle containment radius for E > 10 GeV
Field of View	2.4 sr
Source Location Accuracy	<0.5 arcmin for high-latitude source
Point Source Sensitivity	$<6\times10^{-9}$ ph cm^{-2} s^{-1} for E > 100 MeV, 5σ detection after 1 year sky survey (power-law spectrum with index 2)
Dead Time	<100 microseconds per event

Table 2.2: LAT characteristics, parameters adopted from NASA LAT webpage[5]

At every moment *Fermi*/LAT sees about 20% of the sky. In the survey mode which is the default mode, it needs 2 orbits to cover the entire sky. Basic features of *Fermi*/LAT are summarized in Table 2.2.

Fermi/LAT is a typical pair-conversion telescope with a structure of components described in general overview of pair-production telescopes in Chapter 2.1.2. Its dimensions are 1.8 m in both width and length and 0.72 m in depth with total mass of 2789 kg. Design expectation was to have operational time more than 5 years, which is almost doubled at this moment (over 9.6 years at beginning of April 2018).

Fermi/LAT consist of 4 major elements that were built and tested separately: Tracker, Calorimeter, Anticoincidence Detector (ACD) and Data Aquisition System. Schema of *Fermi*/LAT is presented on Figure 2.5.

Tracker (37 cm^2 area and 66 cm height) is an autonomous device where the actual pair-conversion and tracking of secondary particles takes place. In *Fermi*/LAT there are 16 trackers grouped in the array of 4×4. Each of them is built of layers of tungsten converter foils (incoming photon interacts here) interleaved with silicon-strip detectors. There are exactly 16 tungsten

[5] https://fermi.gsfc.nasa.gov/ssc/data/analysis/documentation/Cicerone/Cicerone_Introduction/LAT_overview.html

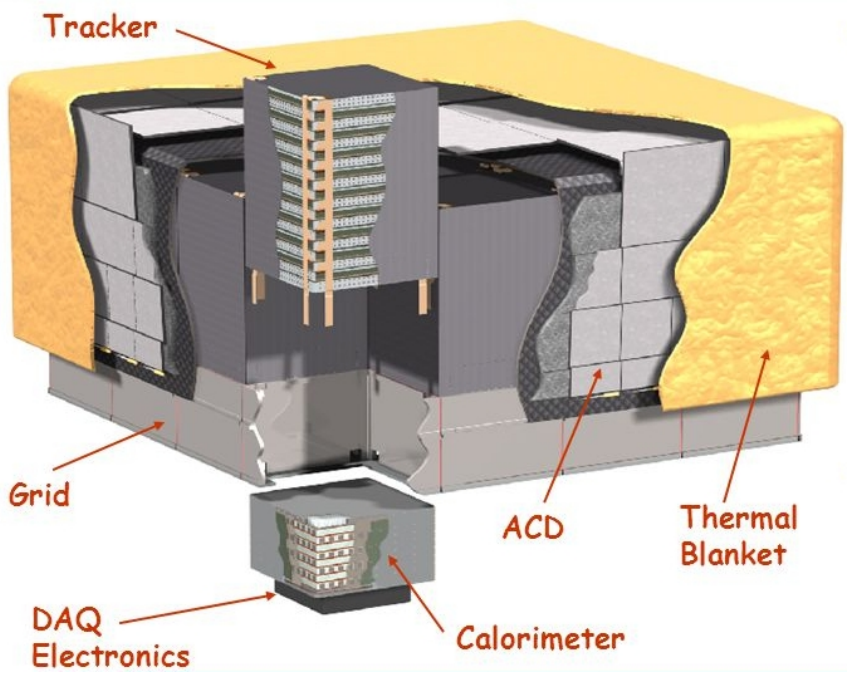

Figure 2.5: Structure of the LAT. Credits: NASA[6]

converters and 18 dual silicon planes in each tracker. Silicon planes are doubled, because one of them is running in x direction whereas the second one in y direction. Such construction of dense detector layers allow a precise path reconstruction of secondary particles in silicon detectors stack. Calculating the direction of electron-positron pair in the first silicon layer (after the conversion), is limited by angular deflection of pair multiple scattering and also by spatial resolution of the tracker. Low energies around 100 MeV are most affected by this effect.

Calorimeter is the element that lies below each tracker tower. There are exactly 16 of them under each tracker. Its goal is to precisely measure incoming energy, time and 3-dimensional path of charged particles. At this stage the 2 particles created by γ-ray photon are mostly totally absorbed. Material that allow full absorption is cesium iodide (CsI) and it is used in scintillator that produces flashes of light. Intensity of those flashes is proportional to particle energies. There are exactly 96 CsI narrow crystals in each calorimeter unit formed in 8 layers. Since the pattern of flashes in crystals is different for cosmic-rays and γ-rays, the calorimeter supports the anti-coincidence shield in rejecting unwanted cosmic-rays.

Anticoincidence detector is a wrapper around the array of towers and one of its goals is to block cosmic-rays that are constantly hitting the *Fermi*/LAT surface, Moiseev *et al.* (2007). This mechanism allows to reject over 99.97% of not desired events. ACD is built of 89 plastic scintillator planes, where flashes of light appear due to excitation of material after incoming charged particles. In contrast to charged cosmic-rays, γ-rays are electronically neutral and they passes through anticoincidence detector without any interaction.

Data Acquisition System collects events and signals from the previous 3 elements and classifies them. It works like a dispatcher which filters out the most probable events that are the γ-ray photons and decides whether they are qualified to be send to ground station. Its secondary objec-

[6] `https://fermi.gsfc.nasa.gov/ssc/data/analysis/documentation/Cicerone/Cicerone_Introduction/LAT_overview.html`

tive is to do on-board search for γ-ray bursts. Since this element provides both side communication (down-link and up-link) it allows to monitor other elements performance, change their configuration or update a software. All top parts of *Fermi* construction are additionally wrapped in a sort of thermal blanket which defends from micro meteoroids or space debris.

2.3.2 Instrument Response Function and event reconstruction

The parameterized representations of instrument performance, i.e. the instrument response functions (IRFs), is a central component for the data analysis. Initial IRFs were derived through Monte Carlo simulations of the LAT response to signals and backgrounds. The calibration data available from real flight data-taking indicated some modifications needed for optimization of IRFs. Then, the LAT event analysis has been substantially improved since the launch. The accumulated updates have been applied in occasional releases of data, each involving reprocessing of the entire LAT data archive. All data released prior to mid-2011 were based on Pass 6. In 2011 the Pass 7 data, and in 2013 the Pass 7 reprocessed data (known as P7REP data), were released. The current release of the Pass 8 data is available since 2015. Each release includes significant analysis improvements with respect to its predecessors.

P8R2 IRF name	Analysis type, description
P8R2_ULTRACLEANVETO_V6	Extra-Galactic Diffuse Analysis
P8R2_ULTRACLEAN_V6	Background rate between CLEAN and ULTRACLEANVETO
P8R2_CLEAN_V6	Hard spectrum sources at high galactic latitudes
PR2_SOURCE_V68	Galactic Point Source Analysis Off-plane Point Source Analysis Galactic Diffuse Analysis
P8R2_TRANSIENT020_V6	Burst and Transient Analysis (<200s)
P8R2_TRANSIENT015S_V6	Impulsive Solar Flare Analysis

Table 2.3: List of available IRFs, Credits: NASA, FSSC [7]

Taking into consideration different inclination angles of photons versus detector position, wide range of energies and best known equations representing physics interaction, a set of γ-ray events was simulated. This classification is due to results of on board processing in DAQ together with ground processing. List of available IRFs together with analysis type recommendation is presented in Table 2.3. The data type that currently are being released are called Pass 8 (version P8R2 - April 2018). It is a new set of reconstruction algorithms that in the best possible way takes advantage of hardware specification, on flight calibration and best knowledge of physical interactions. Moreover each class of IRF consist of separate event types selection, called partitions. In previous data releases (Pass 7 and older) they differed only by either using top part of tracker or by bottom part. Now in Pass 8 another set of event type partitions were added. Beside FRONT/END

[7] https://fermi.gsfc.nasa.gov/ssc/data/analysis/documentation/Cicerone/Cicerone_Data/LAT_DP.html

event types which are Conversion Types there are also 4 types of Point Spread Function (PSF) (PSF0, PSF1, PSF2, PSF3) and 4 types of EDISP (EDISP0, EDISP1, EDSIP2, EDISP3). PSF partition type refers to different quality of reconstructed direction of photon. The worst classified direction (first quartile) is named as PSF0, with the best one as PSF3. In turn EDISP type refers to four level of quality of reconstructed energy. Similarly EDISP0 gather events with the worst classified energy, and EDISP3 with the best one (fourth quartile). During final analysis of *Fermi* data, one of those selections of IRF and event types should be used, hence all released events by *Fermi* team belongs to some class. For typical galactic and extragalactic sources P8R2_SOURCE IRF class is used with event type FRONT+BACK as a sum of both subsets. For any other analysis an appropriate IRF with subsequent event types (photons passing a specific criteria) should be applied. Table 2.3 presents some recommended type of analysis together with corresponding IRF types (e.g. subtle analysis of extragalactic diffuse sources require most clean photons hence P8R2_ULTRACLEANVETO_V6 class should be used).

2.3.3 *Fermi*/LAT data analysis

The LAT data analysis is based on the maximum likelihood method, described in Chapter 2.2. The *Fermi* Team distributes publicly the science analysis tools, referred to as *Science Tools*, that can be used for standard astronomical analyses. It allows to perform two variants of the analysis, binned and unbinned. In the first one, events are binned in the grid consisting of spatial coordinates and the logarithm of energy, and the likelihood is computed strictly following the description in Chapter 2.2. In the unbinned analysis essentially the same approach is applied, however, it assumes infinitesimally small bin sizes, so that each detected event corresponds to its individual bin. Larger bins result in less-time consuming computations but also in a lower accuracy, since binning destroys information. The unbinned method should produce the most accurate results, because precise values of quantities describing each event are taken into account, however, the computations here may be very long (taking even weeks for some data sets considered in this thesis).

The LAT team assumes that the IRFs can be factorized into three parts (see Ackermann *et al.*, 2012c): the effective area, the point-spread function and the energy dispersion. The last one, i.e. energy dispersion, is currently implemented only in the binned version of the publicly available analysis tools.

The model in *Science Tools* is built and processed in XML files (eXtensible Markup Language) and contains: (i) all known γ-ray point sources (their positions and spectral parameters, usually the spectral index and flux), (ii) Galactic diffuse component, (iii) extragalactic isotropic background, (iv) optional spatially extended sources that have to be included in the analysis. The analysis of a given object is done on the area around its location, typically constrained by the radius of several degrees. This area is called the Region Of Interest (ROI). The unbinned and binned likelihood analysis of the LAT data is performed by the *gtlike* tool, which provides the fitted spectral parameters, its uncertainties and detection significance for each component of the model. However, it does not fit the coordinate positions. The optimization of point source location can be performed by another tool called *gtfindsrc*.

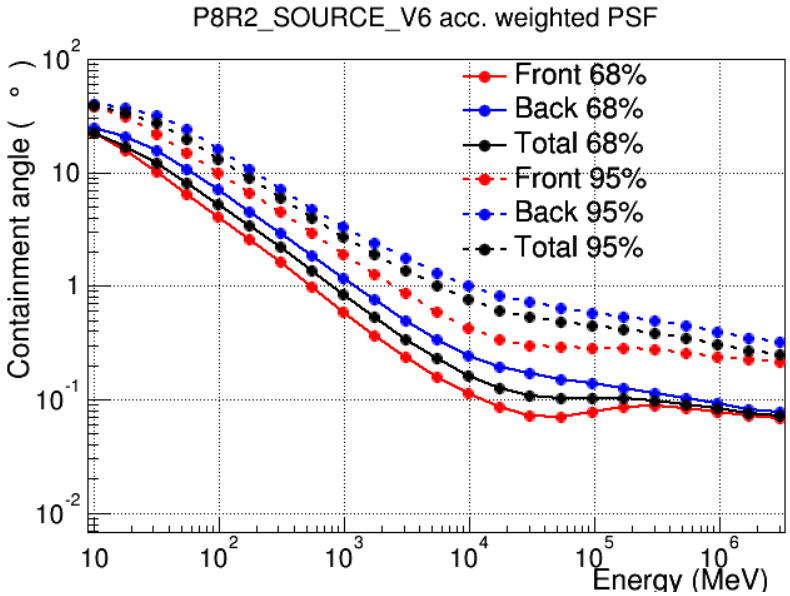

Figure 2.6: 68% and 95% containment angles of the acceptance weighted PSF for both the FRONT/BACK and PSF event types. Adopted from the *Fermi*/LAT performance website[8]

2.3.4 Instrument performance

LAT performance is determined by the design of the hardware, the event reconstruction algorithms, and event selection algorithms. Then, the performance parameters are subjects to improvements, in particular related with optimizations of the event selection algorithms. The current performance of the *Fermi*/LAT is summarized in Figures 2.6 and 2.7, which show effective area and PSF versus energy. As we can see, the effective area drops rapidly below 100 MeV, therefore using the data below 30 MeV or above 500 GeV is in general not recommended. The PSF increases roughly linearly from 10 GeV with decreasing energy to a value greater than 3.5° below 100 MeV.

2.3.5 Key *Fermi* results

Fermi results greatly enhanced view about high-energy universe. Soon after its launch huge γ-ray burst was captured by *Fermi* that had the power of 9000 supernovae, which was the greatest total energy ever seen (Abdo *et al.*, 2009). Other major discoveries include: detection of pulsar in 2010 in CTA 1 supernova remnant, that emitted radiation only in γ-ray band (Abdo *et al.*, 2008); confirming that supernova remnants act as accelerators of cosmic particles; finding huge γ-ray bubbles (Ackermann *et al.*, 2014) extending over 25 thousand light years above and below the Milky Way plane. *Fermi* also looks at Earth close neighborhood and in 2012 it recorded the highest energy light (around 4 GeV) originated from solar eruption, Ajello *et al.* (2014). Terrestrial γ-ray flashes (TGF) are also observed by *Fermi* Gamma-ray Burst Monitor and for the first time positrons were detected (Briggs *et al.*, 2011). Positrons are created due to pair-production of high

[8] http://www.slac.stanford.edu/exp/glast/groups/canda/lat_Performance.htm

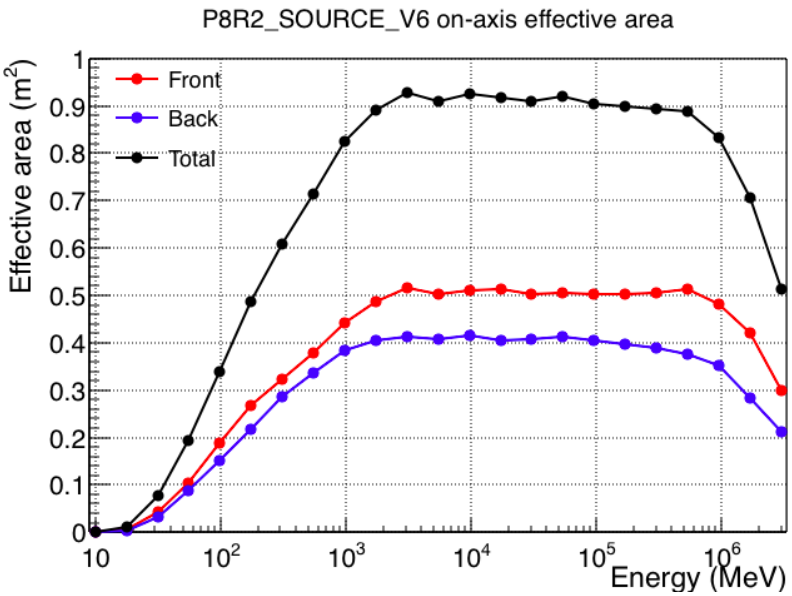

Figure 2.7: Effective area as a function of energy for normal incidence photons. Adopted from the *Fermi*/LAT performance website[9]

energy photons in vicinity of air nuclei and their huge amount strongly exceed the expected value. With new data mode and upgraded analysis methods GBM is able to observe 850 TGF per year (Briggs *et al.*, 2013). A recent major discovery concerns detection and localization of a γ-ray burst GRB 170817A which occurred 2 seconds before gravitational wave (GW170817) was captured by detector LIGO, Abbott *et al.* (2017). Those joint observations were the first indication of common gravitational and electromagnetic radiation from the same source. *Fermi*/LAT detections were systematically published in many catalogs across years. The latest version of catalog of all detected sources in energy range 100 MeV – 300 GeV is 3FGL, Acero *et al.* (2015). It consist of 3033 sources. Other more specific catalogs include the Third Catalog of Hard *Fermi*/LAT Sources (3FHL) for sources detected above 10 GeV with 1556 sources, Ajello *et al.* (2017) and the Third Catalog of Active Galactic Nuclei (3LAC) Ackermann *et al.* (2015), (1591 sources). Currently upcoming 4FGL catalog is preceded by 8-year Point Source List (FL8Y)[10] released in January 2018. FL8Y uses significant analysis improvements as well as a twice longer exposure relative to the 3FGL catalog. FL8Y has not been officially published; after completing with an improved model for Galactic diffuse gamma-ray emission it will be superseded in future by an official 4FGL catalog. It includes 5523 sources above 4-sigma significance based on energy range 100 MeV – 1 TeV.

[9] `http://www.slac.stanford.edu/exp/glast/groups/canda/lat_Performance.htm`
[10] https://fermi.gsfc.nasa.gov/ssc/data/access/lat/fl8y/

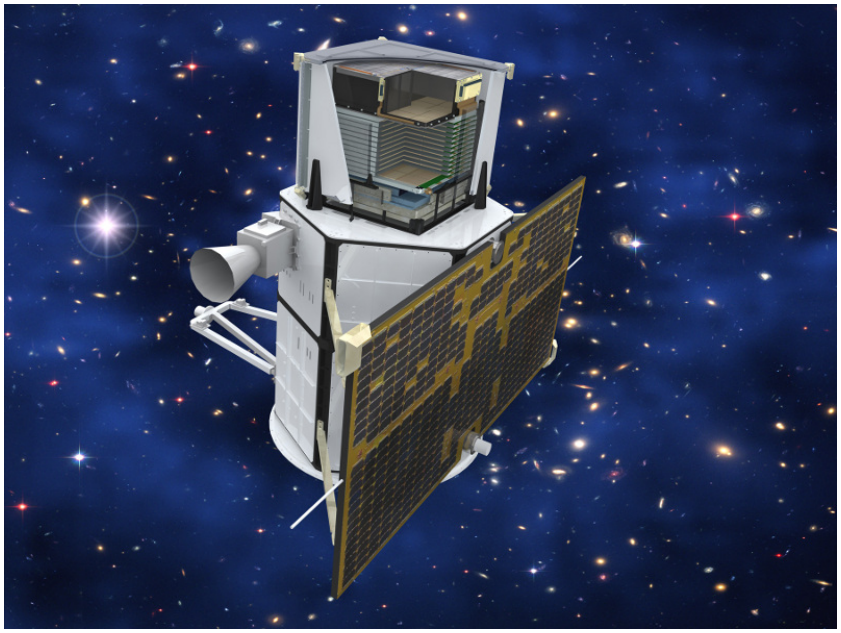

Figure 2.8: *AGILE* satellite[11]

2.4 *AGILE*

2.4.1 General information

AGILE (Astro-Rivelatore Gamma a Immagini Leggero) Tavani *et al.* (2009b), was sent to orbit one year before *Fermi* observatory on 23 April 2007. Comparing to *Fermi* it is relatively small instrument – 130 kg, with total mass of 352 kg during launch. It was build by INFN-INAF and is managed by Italian Space Agency (ASI). Principal investigator is Marco Tavani and co-principal investigator is Guido Barbiellini. The mission was proposed in 1997 to ASI within Program for Small Scientific Missions and soon approved as a first satellite for this program. It took advantage of solid state silicon detector technology, that was developed in INFN laboratories across Italy Barbiellini *et al.* (1995a), Barbiellini *et al.* (1995c), Barbiellini *et al.* (1995b).

The whole idea of building this telescope was to have one integrated instrument made of 3 detectors with broad-band capabilities. On board there are: (i) Gamma-ray Imaging Detector (GRID) sensitive in ~30 MeV – 30 GeV, (ii) Super-*AGILE* working in hard X-ray range (18-60 keV) and (iii) CsI Mini-Calorimeter (MCAL) sensitive at 250 keV — 200 MeV and partially overlapping with GRID. Despite MCAL is not an imaging detector it can provide timing and spectral information of transient events supporting GRID. There are many features that are pretty unique for *AGILE* comparing to other high energy missions. Previous generation of instruments like COS-B, EGRET required specific gas operations e.g refilling whereas *AGILE* does not. Moreover fast electronic readout doesn't need high voltages and it has very small detectors' dead-times. Combination of γ-ray imager and X-ray detector working in 10-40 keV energy range is one of its kind and allow to precise measure coordinates of point and transient sources within one minute of arc.

[11] http://agile.asdc.asi.it/topresults.html

Those advantages make *AGILE* the best possible detector for investigating γ-ray transients for the first time in sub-millisecond time scales in systematic way. Its construction is strictly focused on optimal performance for transient events like γ-ray bursts or unknown γ-ray sources. After first two years when *AGILE* was operating in pointing mode it had to switch to survey mode on 4 November 2009.

2.4.2 Instrument overview

2.4.2.1 Silicon tracker: part of Gamma-ray Imaging Detector (GRID)

Silicon tracker is the main *AGILE* instrument that covers the γ-ray energy band and it was developed by INFN-Trieste. The tracker consist of 12 square planes, each composed of two silicon layers. Every Si-layer is built of 4×4 Si-tiles with total covering area of 38×38 cm^2. Silicon layers are interleaved with tungsten layers, where the actual pair conversion of high-energy γ-ray photon takes place. First 10 out of 12 silicon planes are set as follows: first tungsten layer and then two Si-layers. In order the GRID to be triggered, at least 3 Si-planes need to be activated. That is why there are 2 more silicon layers inserted at the bottom of tracker construction, without any tungsten layers. Distance between planes is 1.9 cm and was optimized by performing Monte Carlo simulations. When *AGILE* started operating, GRID had the smallest ever measured dead time for γ-ray detection (lower than 200 μs). Sensitivity in on-axis is comparable to EGRET, whereas in off-axis it is significantly better. GRID has large field of view covering 1/4 part of the sky (~3 steradians) for each pointing, which is 6 times wider than EGRET. Optimal angular resolution is achieved for very bright sources and its accuracy is between 5 to 20 arc minutes. Comparing to EGRET it is improvement by factor around 2. On 10 May 2007 first γ-ray photon was obtained on orbit by GRID. Table 2.4 summarize basic technical properties of *AGILE*/GRID instrument.

Parameter	Value or range
Energy Range	30 MeV – 50 GeV
Effective Area	>500 cm^2 maximum effective area at normal incidence
Angular Resolution	3.5°, on-axis, 68% space angle containment radius for E = 100 MeV 0.6°, on-axis, 68% space angle containment radius for E = 1 GeV
Field of view	~3 sr
Source Location Accuracy	~5–20 arcmin
Point Source Sensitivity	$<3\times10^{-7}$ ph cm^{-2} s^{-1} for E > 100 MeV, 5σ detection in 10^6s
Deadtime	~200 μs

Table 2.4: Properties of *AGILE*/GRID detector, Credits: *AGILE* Collaboration [12]

[12] http://agile.asdc.asi.it/a-science-27.pdf

2.4.2.2 Hard X–ray Imaging Detector (Super-AGILE)

Super-*AGILE* is supporting GRID in observations in hard X-ray domain (18-60 keV). It consists of 4 silicon square detectors 19 $\times$ 19 cm^2 placed on top of GRID tracker structure, and ultra-light coded mask collimator inserted 14 cm away from silicon planes. Detector was developed in INAF-IASF Rome. It can provide very precise localization of ~2-3 arc min of GRBs and other transient events. Hardware offers excellent timing with deadtime about 4 μs for each independent readout unit. Also field of view is quite big for such energy range and can reach ~0.8 steradian. Super-*AGILE* allows for simultaneous observation of high energy sources by combining X-ray imaging with GRID γ-ray imaging for the first time. Moreover, if flaring γ-ray source is outside Super-*AGILE* FOV (which is ~3$\times$ smaller than FOV of GRID) then *AGILE* can repoint to include flaring source into Super-*AGILE* field of view. Super-*AGILE* general purpose is to discover new GRBs, monitor AGN sources and galactic transients. Special objects of Super-*AGILE* interests are those with shared X-ray and γ-ray properties like blazars having strong X-ray continuum (e.g 3C 273, Mrk 501) or galactic jet sources. Figure 2.9 shows schema of *AGILE* instrument with all its detectors.

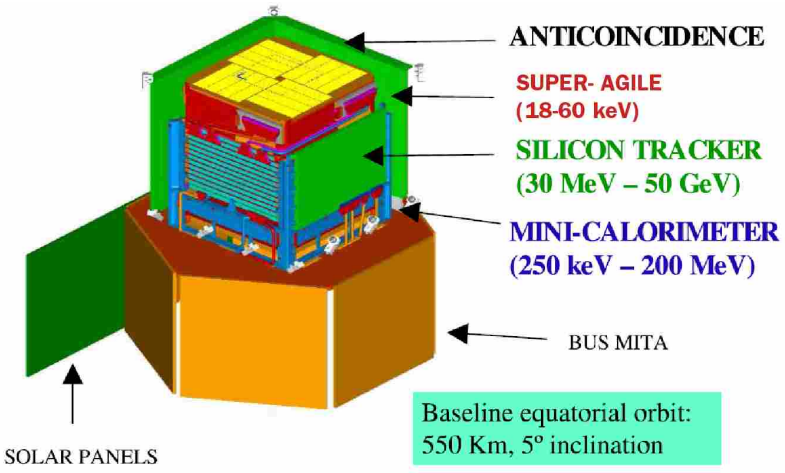

Figure 2.9: *AGILE* payload, *AGILE* Collaboration Pittori (2003)

2.4.2.3 Mini Calorimeter (MCAL), part of GRID

Mini Calorimeter is supporting GRID silicon tracker by covering lower part of γ-ray range up to 200 MeV. It doesn't have imaging capabilities, but it provides unprecedented timing as well as spectral information of observed events. It is developed as part of GRID but it works completely independent of its functions. MCAL is constructed of two planes of 15 Cesium Iodide bars each wrapped in tight diffusion material. After receiving a signal from one of 30 bars, it is collected by two photo diodes at both ends of detector. MCAL can work in GRID mode and measure energy deposit after photon conversion pair takes place, which provides additional information about final properties of particles. In second BURST mode its primary objective is to detect GRBs and weak transients in dedicated 0.25 -200 MeV range.

2.4.2.4 Anti-coincidence system (AC) and data handling system

Anti-coincidence system is fulfilling two primary objectives. It provides background rejection of charged particles and passes through only neutral ones, the other is initial reconstruction of photon direction. AC completely wraps all 3 detectors (GRID, Super-*AGILE*, MC). Each side is segmented in three plastic scintillator layers, 0.6 cm thick and they are connected to photo multipliers at the bottom of instrument. From event handling perspective, processing logic is divided into 3 levels: Level-1, Level-2 and intermediate Level-1.5. Level-1 involves response from GRID in at least 3 contiguous silicon planes, combination of proper chip signals and response from anti-coincidence system. Response from Level-1 is very fast ($< 5\ \mu$s) and is followed by Level-1.5 ($\sim 20\ \mu$s) when event topology is investigated. Both first stages are providing hardware mechanisms for eliminating unwanted initial background events. Final on-board Level-2 stage is the longest one (duration of few ms). It consists of GRID readout of particles trajectories and proper decoding of top and lateral AC signals. First 2 levels are experiencing most number of events reaching up to few thousand events/s, whereas goal of Level-2 stage is to reduce the filtered events further by a factor from 3 to 5. In order to achieve main goal of *AGILE* (which is looking for transients and GRBs) a special burst search algorithms were implemented and appropriate data buffers developed. Particle background rejection is estimated with an inefficiency as low as 10^{-4} (Perotti *et al.*, 2006).

2.4.3 Analysis technique

The *AGILE* data released by ASI Space Science Data Center (SSDC, previously known as ASDC) are organized in event files with 4 classes of events (G, P, S, L). For most analysis class G is used (event is γ-ray photon), whereas the rest are: P–charged particle, S-single track (no separation from electron and positron), L–not classified. To determine where *AGILE* was pointing at given time, one auxiliary file LOG is needed. Current software version that allows to perform *AGILE* analysis is `AGILE_SW_5.0` package, built in 2011. Proper analysis consists of at least 3 steps before the actual fitting model to data procedure takes place. Step one is creating counts map with `AG_ctsmapgen` tool. Step two requires execution of tool `AG_expmapgen`. It produces exposure map by integrating exposure between start and end time of analysis. Step three `AG_gasmapgen2` uses exposure map from previous step and creates diffuse emission map (fits file), where each pixel contains diffuse emission in this pixel. Finally at the end of process, actual fitting can be done with the tool `AG_multi4`. It uses the binned maximum likelihood method described in Chapter 2.2. `AG_multi4` uses result files from 3 previous steps and takes advantage of model file, that is build for the desired region of interest. Model is stored as a text file and every line contain entry about position in galactic coordinates, spectral index, flux and flag that defines what parameters are frozen and what are left free in the procedure. In the end user gets a final report with generated flux, spectral index, significance value of all sources that were left free in the likelihood process. The it AGILE Data Center Team prepared an online tool that allows to perform analysis, without downloading large volumes of data, and with no need to install the software, publicly available at *AGILE* web site[13]. This tool is also a part of 'Open Universe' portal that supports open access to

[13] `http://www.asdc.asi.it/mmia/index.php?mission=agilelv3mmia`

astronomy science data[14].

2.4.4 Key *AGILE* results

During 10 years of *AGILE* operation time, it fulfilled many goals and made many interesting discoveries. Surprising discovery of γ-ray flares from the Crab Nebula between 19 to 22 September 2011 is probably the biggest achievement of *AGILE* instrument Tavani (2011). *Fermi* managed to confirm the flare one day later. Crab always used to be treated as a standard candle producing radiation in a constant way. However variable γ-ray flares turned out to be not produced by the pulsar itself but by pulsar particle wind. It produces strong shocks that accelerate particles in internal part of nebula. That allows to rethink particle acceleration models, that are still not well understood. One small mission that only one country managed to construct and maintain, was able to deliver important contributions for astrophysics and physics of plasma. To honor this discovery Principal Investigator (Marco Tavani together with *AGILE* Team) was awarded Bruno Rossi Prize in High Energy Astrophysics on 10 January 2012. The other discovery was remarkable first ever direct measurement of neutral pion emission in supernova remnant W44 Giuliani *et al.* (2011). Finding evidence of proton acceleration was a 'Holy Grail' of several satellites working at γ-ray domain since studies of W. Baade and F. Zwicky in 30'. *AGILE* effectively working at energies close to 100 MeV could measure characteristic spectrum from decay of pions (from proton-proton interactions) and therefore resulting γ-rays in super nova remnants. SNRs were predicted to be natural accelerators of cosmic-rays but this physical process usually is elusive and is covered by dominated leptonic processes. *AGILE* also detected for the first time several γ-ray flares above 100 MeV from the Cygnus X-3 microquasar, in correlation with a repetitive pattern of multiwavelength radio and X-ray emission (Tavani *et al.*, 2009a: and references therein). Excellent capability of detecting transients by AGILE led to discovery of γ-ray flaring activity above 100 MeV on timescales of a few days consistent with the Cygnus X-1 microquasar (Sabatini *et al.*, 2010).

AGILE also turned out to be perfect instrument for detecting Terrestrial Gamma-ray Flashes, which were observed for the first time with energies of 40 MeV (Marisaldi *et al.*, 2010a) by MCAL. Understanding their nature lead to the conclusion that their spectrum is created by accelerated electrons braking on air nuclei (Bremshtrahlung). *AGILE* was the only mission that performed localization of TGFs (Marisaldi *et al.*, 2010b). Further on also detections of γ-ray emission reaching 100 MeV were observed (Marisaldi *et al.*, 2010c). *AGILE*, just like *Fermi*, produced γ-ray source catalogs with its detections. Following the first *AGILE*/GRID catalog (1AGL) Pittori *et al.* (2009), the most recent is 1AGLR Verrecchia *et al.* (2013) which summarizes *AGILE*/GRID pointing observations from 2 years. It has 54 objects detected in energy range 30 MeV – 50 GeV. Other *AGILE*/GRID catalog resumes *AGILE* findings of TeV counterparts in MeV-GeV range based on the same pointing period Rappoldi *et al.* (2016) (52 sources). The most important catalogs of *AGILE*/MCAL detector is The *AGILE* MCAL Gamma-ray Burst Catalog (350 keV - 100 MeV) with 84 bursts Galli *et al.* (2013) and Terrestrial Gamma-ray (TGF) catalog below 30 MeV Marisaldi *et al.* (2014) with observations carried from March 2009 to July 2012.

[14] http://www.openuniverse.asi.it/

2.5 Instruments performance

New generation of currently working telescopes had to fulfill several major requirements, one was to improve γ-ray angular resolution around 100 MeV at least by a factor of 2-3 comparing to EGRET. The other target was to improve flux sensitivity near this energy. Third important condition was to have large field of view preferably covering 25% of the sky. All these conditions are met in currently operating telescopes. It is important to highlight *AGILE* performance especially against direct predecessor- one of the Great NASA Observatories - EGRET and currently working *Fermi*/LAT. 2 major properties of γ-ray telescopes are crucial, when comparing their capabilities. These are: angular resolution and sensitivity of detectors. From performance tests that were made both for *Fermi*/LAT and *AGILE*/GRID between energies 100 MeV to 1 GeV, the angular resolution of these detectors is similar. Tests were made for the same object: Crab Sabatini *et al.* (2015), with strong emission in γ-rays. Significantly better results are in turn obtained by *Fermi*/LAT in higher energies above 1 GeV. Figure 2.10 shows comparison of angular resolution of those two telescopes. Sensitivity comparison for point sources can be made based on Point Spread Function and the amount of residual background. Figure 2.1 shows sensitivities for most important missions like *Fermi*, EGRET, as well as some other ground TeV telescopes after 10^6 s of observations. When looking at common range of *AGILE* and *Fermi* it looks that sensitivity is improving when PSF gets smaller above 100 MeV. Also amount of background counts gets smaller and effective area is enlarged.

Although there are significant differences in sensitivity between *AGILE* and *Fermi* after long exposure, that doesn't affect much the ability of *AGILE* to investigate γ-ray transients lasting from hours to days. Such comparison of detecting flaring γ-ray sources above 100 MeV and lasting a few days was made, and is described in *AGILE* technical document[15], in Figure 24. Few days is typical duration of AGN-flaring time and the analysis was done during first year of *Fermi* operation, in its scanning mode compared to *AGILE* in its initial pointing mode.

[15] https://agile.asdc.asi.it/a-science-27.pdf

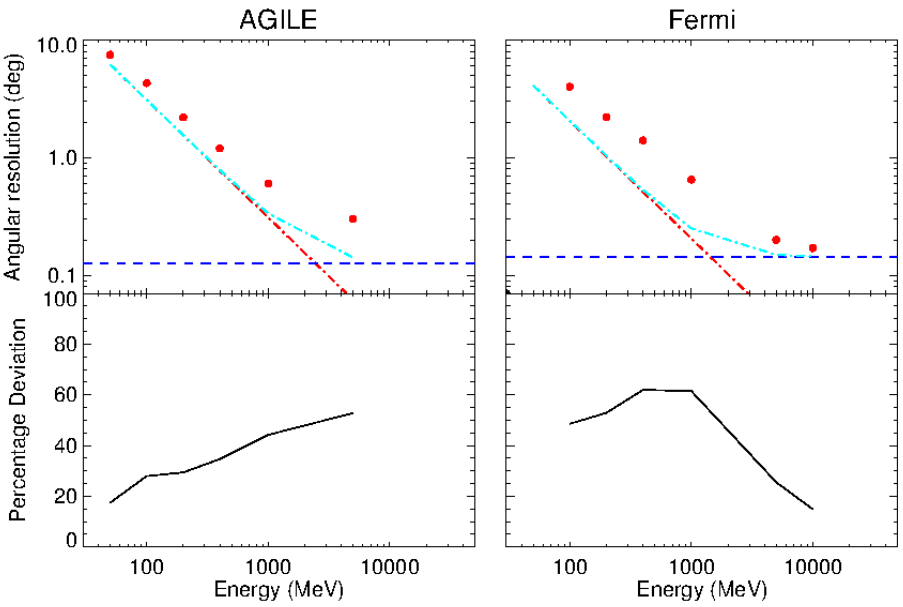

Figure 2.10: Expected limiting values for the angular resolution (dot–dashed cyan line) to the measured ones (red points) for: *AGILE*/GRID (left)- simulated Crab data and *Fermi*/LAT (right). Bottom panels shows percentage deviation of the measured angular resolution from the overall expected limiting value, *AGILE* Collaboration Sabatini *et al.* (2015)

Chapter 3

Hadronic γ-ray emission from hot accretion flows

In the central parts of hot flows, protons have energies above the threshold for pion production. Then, these flows may produce considerable γ-ray fluxes from the decay of neutral pions. This property was noted early in the development of the accretion theory, for instance, by Shapiro *et al.* (1976), and it was considered for the currently popular advection-dominated accretion flow models by Mahadevan *et al.* (1997). As estimated in Shapiro *et al.* (1976) and Oka & Manmoto (2003), the γ-ray luminosity, L_γ, of a flow surrounding a rapidly rotating black hole may be similar to its X-ray luminosity, $L_{\rm X}$. However, these studies neglected the general relativistic (GR) transfer of γ-ray photons as well as the absorption of these photons in the radiation field of the flow. Improved computations by Niedźwiecki *et al.* (2013) showed that L_γ is strongly reduced if these effects are taken into account (see also Figure 4.3 below for illustration of the magnitude of these effects). The precise γ-ray emission model, however, has not been directly compared with current observational data.

Below I present the study of the hadronic γ-ray emission from accretion flows following the approach of Niedźwiecki *et al.* (2013). It relies on a GR hydrodynamic description of the flow combined with GR, Monte Carlo (MC) computations of radiative processes. Solutions were obtained for a range of accretion rates that allows comparing these results with analysis of objects of bolometric luminosities between $\sim 10^{-4}$ and 10^{-2} of the Eddington limit (see Chapter 3.4).

After a short overview of the hot flow model in Chapter 3.1, in Chapter 3.2 I present the model applied in my study and in Chapter 3.3 I discuss the dependence of the predicted L_γ on various parameters of the model, which has not been fully explored with precise computations before. These model predictions are compared with observations in Chapter 4.

3.1 Hot accretion flows

First models of accretion discs were developed in the early 1970s (Shakura & Sunyaev, 1973; Novikov & Thorne, 1973). They described geometrically thin, cold discs which were not able to explain large amounts of hard X-ray emission observed from Cyg X-1. This motivated the work on alternative solutions. The first hot flow model, described by Shapiro *et al.* (1976), included basically all important properties of this class of models. The major novelty of the Shapiro *et*

al. (1976) model was the introduction of a two-temperature accreting plasma, where the protons are much hotter than the electrons. This allowed to explain the geometrical thickness of such flows (supported by the large pressure of protons) and the related optical thinness. This, in turn, gave large temperature of the gas, with that of proton approaching the virial temperature. Their particular solutions were found to be thermally unstable, but it was soon realized that thermal stability is achieved with an inclusion of advection (Ichimaru, 1977), i.e. in flows with dissipated energy used to the heating (and then advected with the flow) rather than being radiated away. Similar models were independently considered by Rees *et al.* (1982) for explanation of low radiative efficiencies of the nuclei of some elliptical galaxies with large jet structures.

The current interest in this class of models was initiated in the mid-1990s (Narayan & Yi, 1994; Narayan & Yi, 1995; Abramowicz *et al.*, 1995). These works introduced the popular in literature term of advection-dominated accretion flow (ADAF); some authors use also another name of radiatively inefficient accretion flow (RIAF). These names are not fully adequate in the whole range of parameters, therefore I refer to these models as hot flows.

As noted in Chapter 1, the hot accretion flow model provides the most widely accepted explanation of black hole systems observed at low luminosities. The radiative properties of hot flows have been studied in a number of works and the model has been applied to various black hole systems including Sagittarius A* in our Galactic center, low-luminosity AGNs, and BHBs in their hard and quiescent states, reviews of these results are given e.g., in Yuan & Narayan (2014), Poutanen & Veledina (2014).

Detailed modeling is, however, subject to theoretical uncertainties on the MHD processes, with the uncertainty regarding the direct heating of electrons being particularly important for my study. Early work on the two-temperature flows (e.g. Ichimaru, 1977; Rees *et al.*, 1982; Narayan & Yi, 1995) assumed that most of the viscous energy goes into the protons and only a small fraction, $\delta < 0.01$, goes into the electrons. Later works on particle heating by magnetic reconnection (e.g. Bisnovatyi-Kogan & Lovelace, 1997; Quataert & Gruzinov, 1999), or MHD turbulence (e.g. Quataert, 1998; Quataert & Gruzinov, 1999; Medvedev, 2000), estimated that a much large fraction of accretion power may go directly to electrons, even comparable to that going to protons, but this issue remains very unclear.

Another major uncertainty concerns the presence of nonthermal particles. Several acceleration mechanisms have been considered for a compact region around the black hole, including the shock acceleration (e.g. Kazanas & Ellison, 1986; Spruit, 1988), magnetic reconnection (e.g. Khiali & de Gouveia Dal Pino, 2016), stochastic acceleration in the accretion-flow turbulence (e.g. Dermer *et al.*, 1996; Kimura *et al.*, 2015), or even acceleration by the electric potential difference in the magnetosphere of a rotating black hole (e.g. Neronov *et al.*, 2005; Ptitsyna & Neronov, 2016). All these processes are likely to accelerate a fraction of the protons and electrons into a nonthermal power-law distribution. While details of energy dissipation and particle acceleration are uncertain, it is clear that Coulomb collisions are too inefficient to thermalize the ions (Mahadevan & Quataert, 1997) and Coulomb coupling between protons and electrons is also inefficient. Then, the protons retain the energy distribution acquired through viscous heating.

3.2 Model of high-energy emission from hot flows

The model applied here was developed in Niedźwiecki *et al.* (2012); Niedźwiecki *et al.* (2013); Niedźwiecki *et al.* (2014); Niedźwiecki *et al.* (2015) and Xie *et al.* (2010). It precisely describes both the structure and radiative processes of hot accretion flows, taking into account, in particular, the global Compton effect, which is important in the considered range of 10^{-4} to $0.01 L_{\rm Edd}$. Calculations are performed in several steps. First, the hydrodynamic structure solution is found for given parameters and then the energy balance for electrons is iteratively solved. These steps were done by my co-authors of Paper 1. Then, I used the X-ray radiation field corresponding to the last, self-consistent iteration to compute the γ-ray luminosity affected by $\gamma\gamma$ absorption.

We considered a black hole that is characterized by its mass, M, and angular momentum, J, surrounded by a geometrically thick accretion flow with an accretion rate, $\dot{M}$. The model has the following free parameters: M, a, δ (electron heating parameter), β (plasma magnetization), α (viscosity parameter), $\dot{m}$ and parameters of the energy distribution of protons in the flow, $\eta_{\rm p}$ and s (defined below). The dimensionless parameters a, β and $\dot{m}$ are explicitly defined in Chapter 1. The α parameter gives the standard form of the viscous stress, $\propto \alpha p$, where p is the total pressure, i.e. including contributions of the gas and the magnetic field. All results presented below assume $\alpha = 0.3$, which is a preferred value for hot flows at least for large $\dot{m}$, see e.g. Narayan & Yi (1995), Esin *et al.* (1997). The density of hot flow solutions approximately follows a simple scaling of $\propto \dot{m}\alpha^{-1}$. Then, there is a degeneracy between α and $\dot{m}$.

Given that the thermalization and cooling timescales for protons are much longer than the accretion timescale, and the distribution of protons is determined by poorly understood heating and acceleration processes, I considered three cases for the proton energy distribution:

(i) thermal model **T** in which all protons have a Maxwellian distribution;

(ii) nonthermal model **N**, where the total power is used to accelerate a small fraction of protons, for which I assumed a power-law distribution, $n_{\rm pl}(\gamma) \propto \gamma^{-s}$ up to $\gamma_{\rm max} = 100$, where γ is the Lorentz factor, and I assumed that the other protons remain cold. The radius-dependent fraction of the protons with the power-law distribution, ψ, is given by

$$\psi(r)\frac{\eta_{\rm p} m_{\rm p} c^2}{s-2} = U_{\rm th}\left[T_{\rm p}(r)\right]. \tag{3.1}$$

where $\eta_{\rm p} = 1$, the left hand side gives the average energy for the power-law distribution and the right hand side gives the average energy of the Maxwellian proton gas

$$U_{\rm th}(\theta_{\rm p}) = \theta_{\rm p} m_{\rm p} c^2 (6 + 15\theta_{\rm p})/(4 + 5\theta_{\rm p}). \tag{3.2}$$

where $\theta_{\rm p} = kT_{\rm p}/m_{\rm p}c^2$, $T_{\rm p}(r)$ is determined by the global hot flow solution and the simplified relativistic form of Gammie & Popham (1998) was used for $U_{\rm th}(\theta_{\rm p})$;

(iii) hybrid model $\mathbf{H}_{0.1}$ with 10% of the energy content in nonthermal protons and 90% of the energy content in thermal protons. For the nonthermal protons I assumed a power-law distribution $\propto \gamma^{-s}$ with $\gamma_{\rm max} = 100$; the fraction of the protons with the power-law distribution is given by equation (3.1) with $\eta_{\rm p} = 0.1$.

I took into account the limiting cases for both the electron heating efficiency and the plasma magnetization. Namely, I considered the case of $\delta = 10^{-3}$, for which electron heating is dominated by Coulomb interactions, and that of $\delta = 0.5$, for which electron heating is dominated by MHD processes. Regarding the magnetic field, I consider weakly magnetized flows with $\beta = 9$, i.e. with the magnetic pressure of 1/10th of the total pressure, and flows with an equipartition between the magnetic and gas pressures, i.e. with $\beta = 1$.

3.2.1 Hydrodynamical solution

The computations are based on the global hydrodynamical solutions of the GR structure equations, including the hydrostatic equilibrium, the energy equations for electrons and protons and the equations for the radial and angular momenta, following Manmoto (2000) with minor improvements described in Niedźwiecki *et al.* (2012). The solution yields the radial distribution of the density, height-scale, velocity field, proton temperature and the initial electron temperature. From this, the self-consistent electron temperature distribution is found, $T_{\rm e}(r)$, for which the electron energy balance with global Compton cooling is achieved. Finding $T_{\rm e}(r)$ requires several iterations between the solutions of the electron energy equation and the MC Comptonization simulations for each set of parameters. This procedure involves the assumption that the flow structure is not affected by changes in $T_{\rm e}$, which constrains the range of exact solutions to $\lambda_{2-10\,{\rm keV}} \lesssim (1-2)\times 10^{-3}$, see Chapter 3.4.

Most of hydrodynamical properties of hot flows, which are relevant for my results, were described in previous works on this subject; the only novelty of computations presented here is taking into account a purely nonthermal distribution of protons (in model N) and its effect on the equation of state. Then, I only briefly note the most important properties.

The general property of accretion flows is that lower thickness (i.e. lower H/R ratio, where H is the height-scale) gives a higher density (e.g. Frank *et al.*, 2002). This, in turn, leads to a significant dependence on plasma magnetization. Namely, for smaller β (i.e. stronger magnetic field) a larger fraction of the accretion power is used to build up the magnetic field strength; therefore, the energy heating the particles, and hence the ion temperature and pressure are smaller. The contribution of magnetic field to the total pressure is characterized by the adiabatic index (4/3) smaller than that of the proton gas (5/3; protons are non-relativistic through most of the flow). Then, a flow with larger β is less compressible and has a larger height-scale. Also a flow supported by the pressure of a nonthermal, relativistic proton gas (as in model N), described by the adiabatic index of $\simeq 4/3$, is more compressible than a supported by thermal protons. Both effects, i.e. higher plasma magnetization and relativistic acceleration of protons, result in a smaller geometrical thickness and, hence, higher density.

The dependence on a involves a well known GR effect of the stabilization of the circular motion of the innermost part of the flow by the rotation of the black hole, which effect is directly related with properties of test particle motion, analogous to the well-known dependence of the innermost stable orbit on a in Keplerian discs. Then, higher a yields both a higher density (because the stabilization implies a lower radial velocity) and a higher proton temperature (because the stabilization implies a larger heating rate).

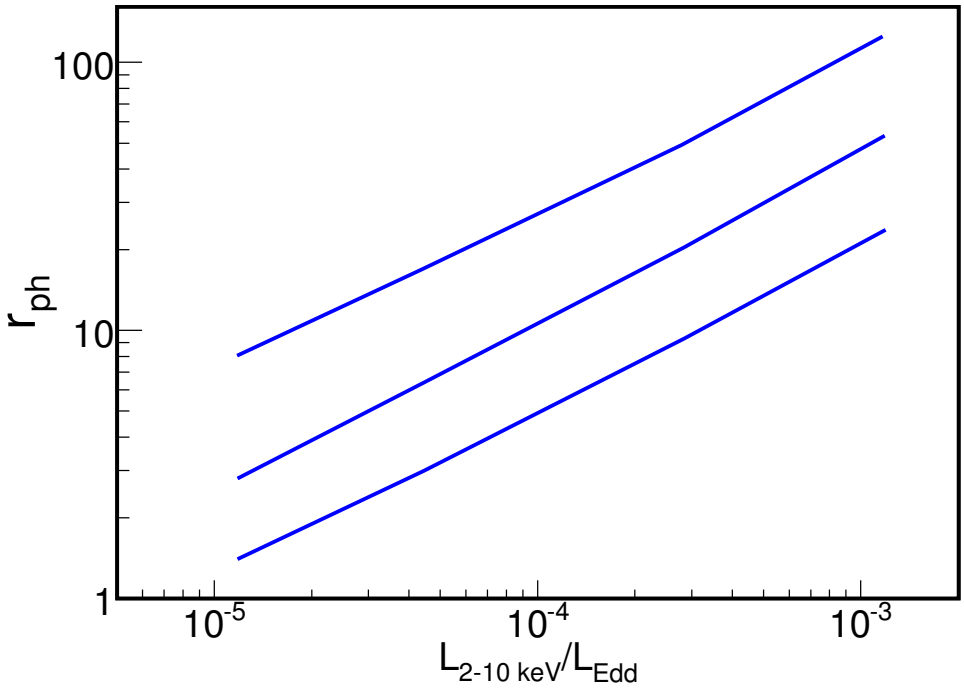

Figure 3.1: Photosphere radius for photons with energies of 0.1, 1, and 10 GeV from bottom to top as a function of $\lambda_{2-10\,\mathrm{keV}}$. The figure is for $\delta = 10^{-3}$, $a = 0.95$, $\beta = 1$, but in other models the dependence of r_{ph} on $\lambda_{2-10\,\mathrm{keV}}$ is similar.

3.2.2 Comptonization and $\gamma\gamma$ absorption

Comptonization is the dominant radiative process in hot flows producing the X-ray radiation in the considered range of luminosities. As found in Niedźwiecki *et al.* (2015), the standard hot flow models for AGNs, including seed photons only from thermal synchrotron emission, predicts too hard spectra. Then, in the model applied here, the X-ray radiation is computed taking into account seed photons for Comptonization from nonthermal synchrotron emission. For $\delta = 10^{-3}$, a sufficient amount of seed photons is provided by the synchrotron emission of pion-decay electrons. For $\delta = 0.5$, additional input of seed photons is needed for agreement with the X-ray observational data. Then, we assumed that 10% of the electron heating power is used for their nonthermal acceleration and we included their nonthermal synchrotron emission.

Using the MC Comptonization code, I tabulated the angular-, energy-, and location-dependent distribution of photons propagating in the central region. Then, to compute L_γ , I took into account the absorption of escaping γ-ray photons on pair creation in interactions with the (tabulated) target photons. The interaction probability is given by Equation (9) in Niedźwiecki *et al.* (2013).

3.3 Results

Figure 3.1 shows the size, r_{ph}, of the γ-ray photosphere (inside which the flow is opaque to γ-rays), which is determined as the radius of the emission point, from which the optical depth along the outward radial trajectory is $\tau_{\gamma\gamma} = 1$. The dependence of r_{ph} on $\lambda_{2-10\,\mathrm{keV}}$ is similar in all models (i.e., for different a, β, or δ).

Below I summarize the dependence of γ-ray luminosity on various parameters of the model.

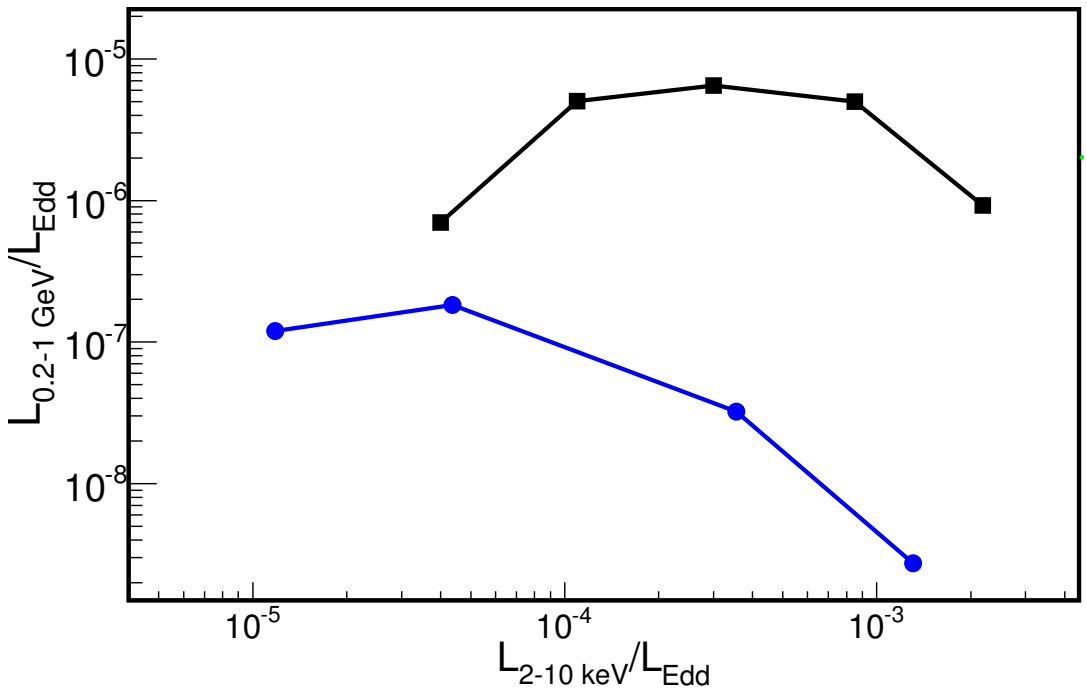

Figure 3.2: $\lambda_{0.2-1\ \mathrm{GeV}}$ as a function of $\lambda_{2-10\ \mathrm{keV}}$. All model points are for thermal protons (model T) with $\delta = 10^{-3}$. The blue line with circles is for $a = 0.95$ and $\beta = 1$ ($\dot{m} = 0.033$, 0.1, 0.3, and 0.5). The black line with squares is for $a = 0.95$ and $\beta = 9$ ($\dot{m} = 0.1$, 0.3, 0.5, 0.8, and 1.2); this model gives *the largest* $\lambda_{0.2-1\ \mathrm{GeV}}$ that can be observed from a hot flow due to pion production by protons with thermal distribution of energies.

For thermal protons, the bulk of the hadronic radiation is emitted in the $\sim 0.1 - 1$ GeV range. The presence of nonthermal protons is reflected in the production of photons with $E > 1$ GeV. Then, I consider these two regimes separately. All results presented below concern the luminosities detected far away from the flow, i.e., affected by GR transfer and $\gamma\gamma$ absorption effects. The luminosities are given as the Eddington ratios defined in Chapter 1.

The presented luminosities are averaged over the observation angle, θ_{obs}. A strong dependence on θ_{obs} occurs only for a rapidly rotating black hole and only at low $\lambda_{2-10\ \mathrm{keV}} \lesssim 10^{-5}$ at which the contribution from the innermost few R_{g} can be directly observed. These luminosities are beyond the range considered here; I extend this discussion in Chapter 4.2.7. At $\lambda_{2-10\ \mathrm{keV}} \gtrsim 10^{-5}$ the anisotropic contribution from the innermost part is attenuated by $\gamma\gamma$ absorption and the difference between γ-ray fluxes received at different θ_{obs} does not exceed a factor of ~ 2.

3.3.1 Thermal protons: $\lambda_{0.2-1\ \mathrm{GeV}}$ vs δ, β, and a

The rate of pion production depends on the number of protons with energies above the pion production threshold. For the thermal distribution of protons, this rate is extremely sensitive to the proton temperature, T_{p}. The pion production rate is low for $T_{\mathrm{p}} \lesssim 10^{12}$ K and negligible for $T_{\mathrm{p}} \lesssim 4 \times 10^{11}$ K. Then, the predicted $\lambda_{0.2-1\ \mathrm{GeV}}$ strongly depends on β, a and δ. This dependence involves the following effects:

- For a smaller β, a larger part of the accretion power is used to build up the magnetic field strength, therefore, the proton heating power is weaker yielding a smaller T_{p}.

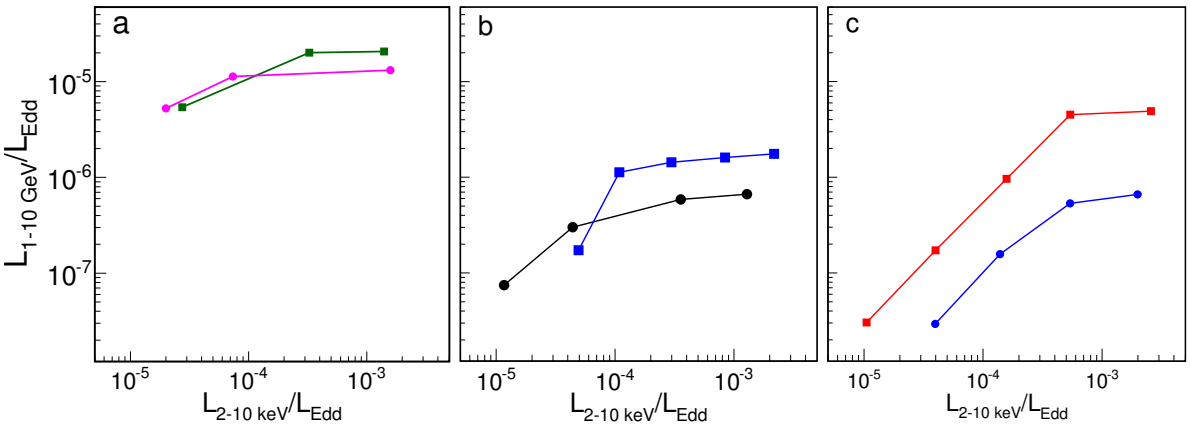

Figure 3.3: $\lambda_{1-10\,\mathrm{GeV}}$ as a function of $\lambda_{2-10\,\mathrm{keV}}$ in models with $\eta_\mathrm{p} > 0$ and $s = 2.1$. (a) Model N with $\delta = 10^{-3}$, the magenta line with circles is for $a = 0.95$ and $\beta = 9$ ($\dot{m} = 0.05$, 0.1, and 0.3), the green line with squares is for $a = 0$ and $\beta = 9$ ($\dot{m} = 0.1$, 0.3 and 0.5). (b) Model $\mathrm{H}_{0.1}$ with $\delta = 10^{-3}$, the black line with circles is for $a = 0.95$ and $\beta = 1$ ($\dot{m} = 0.033$, 0.1, 0.3 and 0.5), the blue line with squares is for $a = 0.95$ and $\beta = 9$ ($\dot{m} = 0.1$, 0.3, 0.5, 0.8 and 1.2). (c) Model N with $\delta = 0.5$, the red line with squares is for $a = 0$ and $\beta = 1$ ($\dot{m} = 0.004$, 0.01, 0.033, 0.1 and 0.3), the blue line with circles is for $a = 0.95$ and $\beta = 9$ ($\dot{m} = 0.003$, 0.01, 0.033 and 0.1).

- A larger δ implies a stronger electron heating and a weaker proton heating, which obviously results in the decrease of the L_γ/L_X ratio.

- A larger a implies that both the viscous dissipation rate (and hence T_p) and the density are larger. Both factors strongly increase $\lambda_{0.2-1\,\mathrm{GeV}}$.

Models with large a, small δ and large β give the *largest* $\lambda_{0.2-1\,\mathrm{GeV}}$ predicted for hot flows, shown by the black curve (with squares) in Figure 3.2. This maximum value of $\lambda_{0.2-1\,\mathrm{GeV}} \simeq 10^{-5}$ is approximately constant for $\lambda_{2-10\,\mathrm{keV}}$ between $\sim 10^{-4}$ and 10^{-3}, where the increase of the rest-frame γ-ray luminosity is approximately balanced by the increase of the opacity. For these parameters the γ-ray emitting region (i.e. with $T_\mathrm{p} \sim 10^{12}$ K) extends out to $r \simeq 20$, so even at $\lambda_{2-10\,\mathrm{keV}} = 10^{-3}$ some significant emission is produced at $r > r_\mathrm{ph}$.

For other values of a, δ or β, the predicted $\lambda_{0.2-1\,\mathrm{GeV}}$ is smaller, even by orders of magnitude, as shown by the blue curve in Figure 3.2 for $\beta = 1$. In this case the γ-ray emitting region is located at $r < 10$, hence, at $\lambda_{2-10\,\mathrm{keV}} = 10^{-3}$ the γ-ray flux is severely attenuated by $\gamma\gamma$ absorption.

3.3.2 Nonthermal protons: $\lambda_{1-10\,\mathrm{GeV}}$ vs δ and η_p

Figure 3.3 shows $\lambda_{1-10\,\mathrm{GeV}}$ in models with relativistic acceleration of protons, efficiency of which is parametrized by η_p. I first emphasize that my assumption that η_p does not depend on r expresses a crucial (assumed) property that the relativistic acceleration occurs in the whole body of the flow. In such a case some γ-ray emission always occurs at $r > r_\mathrm{ph}$. Furthermore, the number of protons above the pion production threshold depends only linearly on the proton heating power. This means that the γ-ray luminosity is much less sensitive to both β and a than in model T. It obviously depends on η_p, and the dependence is stronger than linear due to the hydrodynamical effect noted in Chapter 3.2.1. However, the main effect determining $\lambda_{1-10\,\mathrm{GeV}}$ at a given $\lambda_{2-10\,\mathrm{keV}}$ concerns the radiative efficiency of electrons. The rest-frame γ-ray luminosity depends on the

square of density, so it is $\propto \dot{m}^2$.

- For low values of δ the heating of electrons is dominated by Coulomb interactions, so $\lambda_{2-10\,\mathrm{keV}} \propto \dot{m}^2$. Then, the rest-frame γ-ray luminosity increases roughly linearly with $\lambda_{2-10\,\mathrm{keV}}$. Combining it with the increase of opacity, we get the dependence shown Figure 3.3a (for $\eta_\mathrm{p} = 1$) and 3.3b (for $\eta_\mathrm{p} = 0.1$). The former gives the *largest* predicted from hot flows value of$\lambda_{1-10\,\mathrm{GeV}} \simeq 10^{-5}$ for $\lambda_{2-10\,\mathrm{keV}}$ between $\sim 10^{-5}$ and 10^{-3}.

- For larger δ, the radiative efficiencies are higher, therefore, $\lambda_{1-10\,\mathrm{GeV}}$ is lower (because of the lower $\dot{m}$) at a given $\lambda_{2-10\,\mathrm{keV}}$. Then, in Figure 3.3c I show only results for $\eta_\mathrm{p} = 1$; for $\eta_\mathrm{p} = 0.1$ the predicted $\lambda_{1-10\,\mathrm{GeV}}$ is below the level which can be probed with LAT. For large δ, $\lambda_{2-10\,\mathrm{keV}} \propto \dot{m}$ and therefore the rest-frame γ-ray luminosity $\propto \lambda^2_{2-10\,\mathrm{keV}}$, which explains the fast decrease of $\lambda_{1-10\,\mathrm{GeV}}$ with decreasing $\lambda_{2-10\,\mathrm{keV}}$ seen on Figure 3.3c. Furthermore, for large δ, the radiative efficiency increases with a, as a result, $\lambda_{1-10\,\mathrm{GeV}}$ at a given $\lambda_{2-10\,\mathrm{keV}}$ is by a factor of several larger for $a = 0$ than for $a = 0.95$ (somewhat counter-intuitively).

The uncertain value of δ introduces the main uncertainty in testing the hadronic emission model. It may be partially resolved by including spectral information from the X-ray data. Namely, the Thomson optical depth, τ, of the flow is approximately $\propto \dot{m}$. Then, a larger radiative efficiency (of a larger δ source) implies a lower τ at a given $\lambda_{2-10\,\mathrm{keV}}$. The value of τ can be directly measured in some bright objects, for which the high energy cut-off in their X-ray spectra is observed. For fainter sources, τ can be estimated from the presence or lack of the departures of the X-ray spectrum from a power-law shape. I briefly note the related effects in the next Chapter.

I considered various proton distribution slopes between $s = 2.1$ and 2.7. In all models, the lowest $\lambda_{1-10\,\mathrm{GeV}}$ corresponds to $s = 2.1$; this is related with the assumed $\gamma_\mathrm{max} = 100$, at which a large part of energy is radiated above 10 GeV. For $s = 2.7$, $\lambda_{1-10\,\mathrm{GeV}}$ is larger by a factor of ~ 2.

3.4 X-ray luminosity limits

All model results presented above were computed for a flow extending out to $r = 10^4$, where an outer boundary condition (relating the flow parameters with the Keplerian values at this r) is set. For such a large boundary radius the solution is almost independent of the chosen boundary condition. The computational method applied here allows to investigate solutions with bolometric luminosities between $L \sim 10^{-4} L_\mathrm{Edd}$ and $\sim 10^{-2} L_\mathrm{Edd}$, corresponding to $\lambda_{2-10\,\mathrm{keV}}$ between $\sim 10^{-5}$ and $\sim 10^{-3}$.

The maximum value of $\lambda_{2-10\,\mathrm{keV}} \sim 10^{-3}$ is related with the involved assumptions about negligible effect of Coulomb cooling of protons. At $\lambda_{2-10\,\mathrm{keV}} \sim 10^{-3}$ the Coulomb transfer from protons to electrons (which depends of the square of density and hence its relative importance increases with increasing $\dot{m}$) becomes significant. At higher luminosities the flow structure is characterized by a dramatic dependence on even small changes of T_e (when global Compton cooling is taken into account, cf. Xie *et al.*, 2010) because the Coulomb cooling rate is $\propto (T_\mathrm{p} - T_\mathrm{e})$. This most likely leads to a collapse of the flow and formation of a standard cold disc beyond several tens of R_g, where the ratio of the Coulomb to viscous heating rates is the largest. These physical properties suggest formation of the inner hot flow/outer cold disc geometry, which is indeed

supported by observations of objects radiating at $\lambda_{2-10\,\mathrm{keV}} \gtrsim 10^{-3}$. However, physics of transition between the outer cold disc and the inner hot flow is not well understood. At the same time, hot flow solutions with a small boundary radius are very sensitive to the chosen boundary condition, as found in the preliminary investigation of this regime (i.e. with $\lambda_{2-10\,\mathrm{keV}} > 10^{-3}$) in our group in University of Łódź in collaboration with dr Fu-Guo Xie. A conclusion important for my study is that solutions neglecting the cooling of protons can still be used to assess radiative properties up to $\lambda_{2-10\,\mathrm{keV}} \simeq 3 \times 10^{-3}$ but not for larger luminosities.

I also note that the dependence in Figure 3.1 suggesting a simple scaling of r_{ph} with luminosity cannot be simply extrapolated to $\lambda_{2-10\,\mathrm{keV}} \gtrsim 10^{-3}$. These values of r_{ph} were computed for a flow extending out to large r, where the opacity for a γ-ray photon escaping from r_{em} is dominated by head-head interactions with X-ray photons produced at $r > r_{\mathrm{em}}$. If a flow shrinks to a relatively small size of $\sim 100R_{\mathrm{g}}$, the opacity for γ-rays escaping from the outer parts is dominated by much less efficient head-tail interactions with X-ray photons produced at $r < r_{\mathrm{em}}$.

The minimum luminosity of $\lambda_{2-10\,\mathrm{keV}} \sim 10^{-5}$ that can be studied with the computational method applied here results from the requirement that the energy balance for electrons is determined by radiative cooling (rather than advection). At $\lambda_{2-10\,\mathrm{keV}} \lesssim 10^{-5}$, the differential advective term dominates in the energy equation for electrons which makes the procedure applied here very unstable.

Chapter 4

Gamma-ray activity of Seyfert galaxies and constraints on hot accretion flows

4.1 Introduction

In this Chapter I present the results of my analysis of the *Fermi*/LAT data from radio-quiet AGNs. No prominent γ-ray signal from such objects was found e.g. by Ackermann *et al.* (2012b) and Ackermann *et al.* (2015), except for the three X-ray bright Seyfert 2 galaxies, NGC 4945, NGC 1068, and Circinus, discussed in detail in Chapter 5. The upper limits (UL) on the photon flux in the GeV range, derived in Ackermann *et al.* (2012b), typically constrain the luminosity ratio to $L_\gamma/L_{\rm X} < 0.1$ and in several Seyferts to $L_\gamma/L_{\rm X} < 0.01$, which shows that the sensitivity of the *Fermi*/LAT surveys has reached the level at which predictions of the hadronic emission from hot accretion flows can be probed. This motivated the detailed comparison I present here.

I analyzed 6.4 years of *Fermi*-LAT data of nearby, low-luminosity AGNs, which means that I use a data set that more than three years longer than the one used by Ackermann *et al.* (2012b) and is more than two years longer than the third catalog of AGNs detected by *Fermi*/LAT (Ackermann *et al.*, 2015). A detailed comparison with the model requires a precisely determined black hole mass and intrinsic X-ray luminosity, therefore I focus on several best-studied objects. As a particularly interesting case, I thoroughly examine the data from NGC 4151, for which the ratio of $L_\gamma/L_{\rm X} < 0.0025$, found in Ackermann *et al.* (2012b), is the lowest of the 120 Seyfert galaxies considered in their work.

My main results are presented in Figures 4.3 and 4.4, where I confront observations with predictions for the hadronic emission. In Chapter 4.3 I also briefly consider constraints for the nonthermal acceleration of electrons.

4.2 Sample and data analysis

I considered nearby AGNs with spectral properties consistent with the hot flow model. This includes several Seyfert 1 galaxies: NGC 4151, NGC 5548, IC 4329a, NGC 6814, NGC 4258 and NGC 7213. I also took into account the FR I galaxy Centaurus A, whose X-ray radiation may be dominated by a Seyfert-like emission. These objects show direct evidence of the lack of an optically thick disc in the central region. For objects with the lowest luminosities (NGC 4258

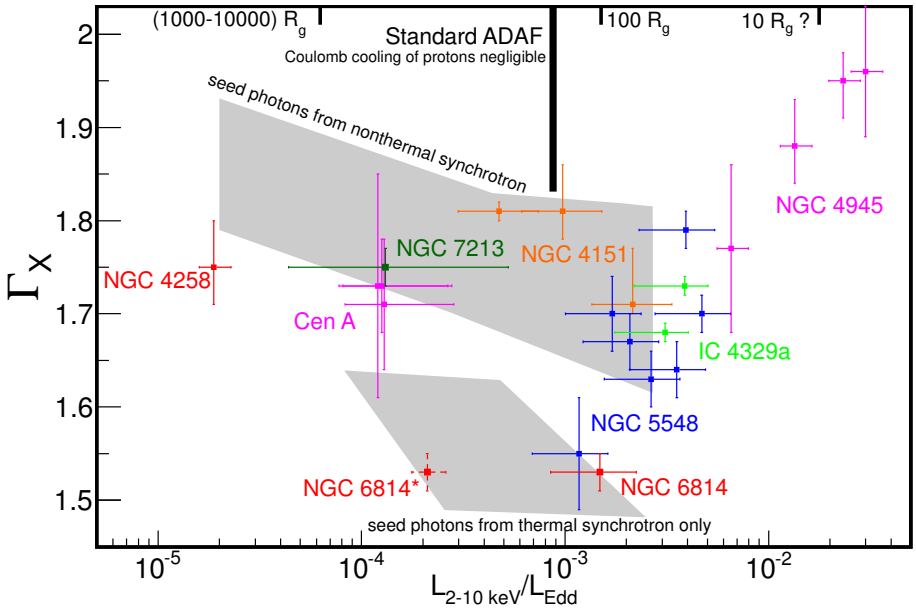

Figure 4.1: X-ray photon spectral index as a function of intrinsic $\lambda_{2-10\,\mathrm{keV}}$. The observational data correspond to the best fits of the high-quality observations described in Sect. 4.2. The gray regions indicate the location of solutions for the model with seed photons from thermal synchrotron only (lower) and including nonthermal synchrotron (of pion-decay or directly accelerated electrons; upper). The thick vertical line indicates the maximum luminosity of flows not affected by the Coulomb cooling of protons. The extent of the gray regions to $\lambda_{2-10\,\mathrm{keV}} \simeq 3 \times 10^{-3}$ corresponds to the approximate applicability of our model. Ticks in the top axis show the approximate value of the truncation radius of a cold disc (see text), which likely gives the size of a hot inner flow. NGC 1068 and Circinus are not shown because the estimates for their intrinsic Γ_X are model dependent.

Table 4.1: Adopted 2-10 keV Eddington ratio, black hole mass, distance, and references for the data. The references are given in the order X-ray measurement, M, and (if available) distance.

Source	$\lambda_{2-10\,\mathrm{keV}}$ $\times 10^{-2}$	M $10^7 M_\odot$	D (Mpc)	Refs.
IC 4329a	0.48	13^{+10}_{-3}	68.4	1^a ,2
NGC 4151	0.12	5.4 ± 1.8	19.0	3^b ,4,4
NGC 4258	0.00094	3.6	7.2	5^c ,6,7
NGC 5548	0.28	$3.2^{+2.3}_{-0.9}$	72.7	8,9
NGC 6814	0.15	$0.26^{+0.19}_{-0.09}$	22.8	10^d ,9,11
NGC 6814*	0.021	1.9 ± 0.4	22.8	10^d ,12,11
NGC 7213	0.014	$8.0^{+16.0}_{-6.0}$	22.0	13,14,11
Cen A	0.012	5.5 ± 3.0	3.8	15,16,17
Circinus	1.1–2.3	0.17 ± 0.03	4.2	18,19,11
NGC 1068	1.7	1.0	14.4	20,21,11
NGC 4945	1.8	0.14	3.6	22,23,24

Notes. $\lambda_{2-10\,\mathrm{keV}}$ given in the second column involves rescaling (based on the *Swift*/BAT data, see text) of the average intrinsic luminosity given in the reference by a factor of $^{(a)}$ 1.3; $^{(b)}$ 1.2; $^{(c)}$ 2; $^{(d)}$ 1.5.

References. (1) Brenneman *et al.* (2014), (2) Markowitz (2009), (3) Lubiński *et al.* (2010), (4) Hönig *et al.* (2014), (5) Reynolds *et al.* (2009), (6) Miyoshi *et al.* (1995), (7) Herrnstein *et al.* (1999), (8) Brenneman *et al.* (2012), (9) Pancoast *et al.* (2015), (10) Walton *et al.* (2013), (11) Tully (1988), (12) Bentz *et al.* (2009), (13) Lobban *et al.* (2010), (14) Schnorr-Müller *et al.* (2014), (15) Fukazawa *et al.* (2011), (16) Cappellari *et al.* (2009), (17) Harris *et al.* (2010), (18) Arévalo *et al.* (2014), (19) Greenhill *et al.* (2003), (20) Bauer *et al.* (2015), (21) Greenhill *et al.* (1996), (22) Puccetti *et al.* (2014), (23) Greenhill *et al.* (1997), (24) Tully *et al.* (2009)

and NGC 7213) studies of the Fe Kα line place the inner edge of optically thick disc between $r_{\mathrm{tr}} \sim 10^3$ and $\sim 10^4$ (Reynolds *et al.*, 2009; Lobban *et al.*, 2010). In more luminous objects (NGC 4151, NGC 5548, IC 4329a, and NGC 6814), the measured Fe Kα line widths, $\lesssim 100$ eV (Lubiński *et al.*, 2010; Walton *et al.*, 2013; Brenneman *et al.*, 2012; Brenneman *et al.*, 2014), indicate truncation of the disc at $r_{\mathrm{tr}} \gtrsim 100$; a similar location of an optically thick disc is indicated by reverberation measurements (Edelson *et al.*, 2015).

I also considered three Seyfert 2 galaxies, NGC 1068, Circinus, and NGC 4945. All three are observed with high bolometric luminosities, above the range that can be precisely studied with the current version of our model. Nevertheless, comparing their γ-ray luminosities with properties of their active nuclei appears to be interesting.

For most AGNs in my sample, direct measurements (through the observed kinematics) of the masses of their supermassive black holes are available. Only for IC 4329a and NGC 7213 I used estimates based on the velocity dispersion. The adopted M and distance values are given in Table 4.1. For NGC 5548 and IC 4329a I assumed the luminosity distances for the following cosmological parameters: $\Omega_{\mathrm{m}} = 0.27$, $\Omega_\Lambda = 0.73$, and $H_0 = 71$ km s^{-1} Mpc^{-1}. The error bars on the values of λ in Figures 4.1 and 4.3 are mostly due to uncertainties in the determination of M. For NGC 4258, NGC 1068, NGC 4945 and Circinus precise measurements of M based on H_20 megamaser kinematics are available. For NGC 6814 the difference of measurements of M between Bentz *et al.* (2009) and Pancoast *et al.* (2015) amount to an order of magnitude, so I present results for both values; the case with the higher value of M is denoted by a star superscript

in Tables 4.1 and 4.2 and Figures 4.1 and 4.3.

Table 4.2 shows the results of my analysis of the *Fermi*/LAT data, described below, except for Centaurus A, for which I used the results of previous studies collected from literature. For NGC 1068, Circinus and NGC 4945 I used results of my analysis of 8 years of observations, presented in the next Chapter. Figures 4.3 and 4.4 show the measured $\lambda_{0.2-1\,\mathrm{GeV}}$ and $\lambda_{1-10\,\mathrm{GeV}}$, or their ULs, as a function of the intrinsic $\lambda_{2-10\,\mathrm{keV}}$. To find the latter, I used results of detailed X-ray spectral studies (specified below) of high-quality data from *Suzaku*, *NuStar,* or simultaneous XMM and INTEGRAL observations, which allow to disentangle the primary X-ray emission from the reflection or absorption components. The parameters of these fits are shown in Figure 4.1. Using the *Swift*/BAT (Krimm *et al.*, 2013) light curves[1], I found that even for the most variable objects (NGC 7213, IC 4329a, and NGC 6814; their light curves are shown in Figure 4.2) the adopted X-ray observations correspond to the flux levels close to the average *Swift*/BAT flux during the analyzed 6.4 years of *Fermi*/LAT observations; in some objects I used the intrinsic $\lambda_{2-10\,\mathrm{keV}}$ rescaled to account for a small deviation from average, see Table 4.1.

We see in Figure 4.1 that spectral parameters of the intrinsic X-ray emission, measured in AGNs with $\lambda_{2-10\,\mathrm{keV}} \lesssim 3\times10^{-3}$, agree with our model of thermal Comptonization in hot flows. The two gray regions shown in that Figure indicate the location of model solutions that include a significant input of seed photons from nonthermal synchrotron radiation (upper gray region) and solutions with only thermal synchrotron emission (lower gray region). We see that typical Seyfert spectra clearly agree with the former solutions, however, they are also occasionally observed with parameters corresponding to inefficient cooling (NGC 6814 and one of NGC 5548 data points). These rarely observed hard spectra may by related with changes of MHD parameters of the flow, e.g. plasma magnetization or acceleration efficiency.

4.2.1 LAT data analysis

For NGC 4151, NGC 5548, NGC 4258, NGC 6814, NGC 7213, and IC 4329a I analyzed 6.4 years of the *Fermi*/LAT data, comprising observations carried out between 2008 August 4 and 2015 January 10. For each object, events were selected from a region with a radius of 15° centered on the position of the analyzed source. I performed the unbinned likelihood analysis using the v9r33p0 *Fermi* Science Tools with CALDB instrument response functions. I used the standard templates for the Galactic (`gll_iem_v05_rev1.fits`) and the isotropic (`iso_source_v05_rev1.txt`) backgrounds. In the likelihood analysis I took into account all sources reported in the *Fermi*/LAT Third Source Catalog (Acero *et al.*, 2015: hereafter 3FGL) within a radius of 15° around the analyzed object. Each of the catalog sources was modeled with a best-fit spectral function (as specified in the catalog, in most cases a power-law) with parameters left free in the model fitting.

Except for NGC 6814 I did not find statistically significant signals. Then, I derived the 95% confidence level ULs for the photon flux using the Bayesian method of Helene (1991) implemented in the `pyLikelihood` module.

I first checked how the use of both an extended data set and improved models (based on 3FGL) of the celestial regions of interest affects the UL values. Assuming the γ-ray photon spectral index $\Gamma = 2.5$, I found ULs for $F_{>0.1\,\mathrm{GeV}}$ lower by a factor ~ 4 (for NGC 7213 and IC 4329a) and ~ 2

[1] http://swift.gsfc.nasa.gov/results/transients

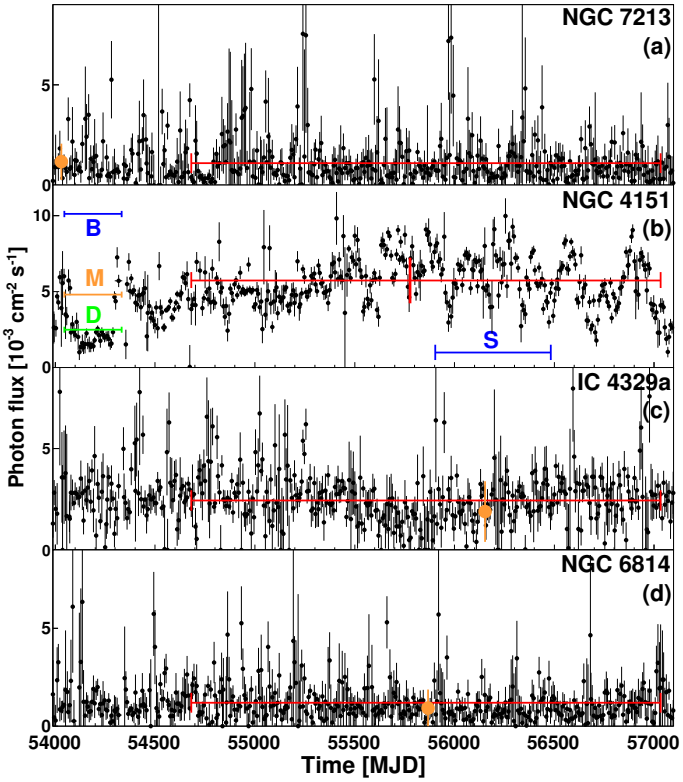

Figure 4.2: Small black circles with error bars show *Swift*/BAT 15-50 keV light curves in seven-day bins for NGC 7213, NGC 4151, IC 4329a, and NGC 6814. The red horizontal line in each panel shows the average flux during the 6.4 years of analyzed *Fermi*/LAT observations. The large orange circles in panels (acd) show the times of the adopted *Suzaku* and *NuStar* observations and the average flux in time bins equal to the duration of these pointing observations. The red vertical line in panel (b) indicates the end of the three-year period used for comparison with Ackermann *et al.* (2012b). The blue line in the bottom of panel (b) delineates period S (see Sect. 4.2.2). The flux levels of dim (D), medium (M), and bright (B) states, defined in Lubiński *et al.* (2010), are shown in the left part of panel (b).

Table 4.2: Integrated photon flux, F_γ, and the photon index, Γ, of power-law fits, or 95% confidence level ULs with the assumed Γ, and the corresponding Eddington ratio for 1–10 GeV (upper part) and 0.2–1 GeV (lower part).

Source	Γ	F_γ 10^{-10} ph/cm^2/s	λ_γ $\times 10^{-5}$
Energy range: 1–10 GeV			
IC 4329a	2.7	< 0.46	< 0.49
IC 4329a	2.1	< 0.68	< 0.88
NGC 4151[a]	2.7	< 1.2	< 0.23
NGC 4151[a]	2.1	< 1.3	< 0.31
NGC 4151[b]	2.1	< 1.8	< 0.43
NGC 4151[c]	2.1	< 1.8	< 0.43
NGC 4151[d]	2.1	< 2.0	< 0.48
NGC 4258	2.7	< 1.1	< 0.043
NGC 4258	2.1	< 1.5	< 0.067
NGC 5548	2.1	< 0.3	< 1.8
NGC 5548	2.7	< 0.6	< 2.9
NGC 6814	2.6 ± 0.1	3.0 ± 0.7	18 ± 10
NGC 6814*	2.6 ± 0.1	3.0 ± 0.7	2.6 ± 1
NGC 7213	2.7	< 0.4	< 0.07
NGC 7213	2.1	< 0.5	< 0.11
Cen A [(1)]	2.1 ± 0.2	18.0 ± 2.7	$0.17^{+0.2}_{-0.1}$
Circinus[e]	2.4 ± 0.1	14.7 ± 1.4	3.1 ± 0.7
NGC 1068[e]	2.5 ± 0.1	9.2 ± 0.8	3.7 ± 0.8
NGC 4945[e]	2.3 ± 0.1	14.7 ± 1.2	2.9 ± 0.6
Energy range: 0.2–1 GeV			
IC 4329a	4.0	< 3.3	< 0.51
NGC 4151 (1)[a]	4.0	< 4.5	< 0.13
NGC 4151 (2)[b]	4.0	< 20	< 0.52
NGC 4258	4.0	< 7.7	< 0.044
NGC 5548	4.0	< 12	< 8.4
NGC 7213	4.0	< 7.1	< 0.18

Notes. [(a)] using the full data set of 6.4 years and including source S in the model; [(b)] $\sim$ 4.9-year data set (6.4 years without period S), source S not included; [(c)] data from the first three years, S included in the model; [(d)] data from the first three years, S not included in the model; [(e)] results of my analysis in Chapter 5.

References.
(1) Sahakyan *et al.* (2013), parameters of the 'second' component above 4 GeV.

(for NGC 5548) than the corresponding UL in Ackermann *et al.* (2012b). For NGC 4151 the UL value is somewhat dependent on the approach to modeling (as discussed below), but in general, I was not able to reduce it significantly below the value quoted by Ackermann *et al.* (2012b).

The π^0-decay spectra can be described by a simple power-law only in limited energy ranges. For the thermal distribution of protons, the spectrum can be very roughly approximated by a very soft power-law, with $\Gamma \simeq 4$, above $\simeq 0.2$ GeV. For the power-law proton distribution, it is a power-law above ~ 1 GeV. Then, to compare with predictions of model T, I assumed $\Gamma = 4$ to find UL for $F_{0.2-1\,\mathrm{GeV}}$. To compare with predictions of models with $\eta_\mathrm{p} > 0$, I found UL for $F_{1-10\,\mathrm{GeV}}$ assuming different values of Γ between 2.1 and 2.7. For all AGNs, except for NGC 5548, the highest ULs

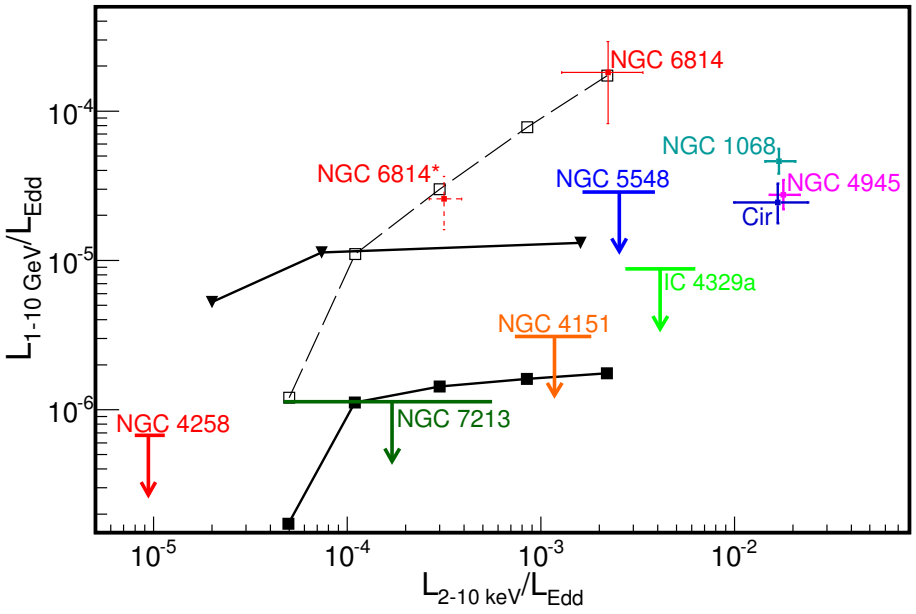

Figure 4.3: $\lambda_{1-10\,\mathrm{GeV}}$ as a function of $\lambda_{2-10\,\mathrm{keV}}$, see Tables 4.1 and 4.2 for the observational data; $\lambda_{2-10\,\mathrm{keV}}$ corresponds to the average X-ray luminosity during the *Fermi*/LAT observations (see text). The solid lines are for model N with $\delta = 10^{-3}$, $a = 0.95$, $\beta = 9$ (triangles) and model $\mathrm{H}_{0.1}$ with $\delta = 10^{-3}$, $a = 0.95$, $\beta = 9$ (squares). The former model significantly exceeds the ULs for three AGNs, which rules out a scenario with most of accretion power used for relativistic acceleration of protons. The dashed line with open squares is for the *rest-frame* luminosity in the latter model (i.e., $\mathrm{H}_{0.1}$). Such γ-ray luminosities, neglecting $\gamma\gamma$ absorption and GR transfer of radiation, were studied by Mahadevan *et al.* (1997) and Oka & Manmoto (2003). We see that simplified treatment in their works overpredicts the observed luminosities even by two orders of magnitude and significantly affects the comparison with observations.

correspond to $\Gamma = 2.1$ (the difference for other values of Γ does not exceed a factor of 2), and I used them in Figure 4.3. The comparison in Figure 4.3 is presented in the most conservative manner, meaning that I used the lowest $\lambda_{1-10\,\mathrm{GeV}}$ predicted by the model (for $s = 2.1$) and the highest UL value (for $\Gamma = 2.1$).

4.2.2 NGC 4151

At the position of NGC 4151 I found a signal with the test-statistic significance TS $\simeq$ 17 for $E = 0.2 - 6$ GeV, see Figure 4.5d. It most likely contains a contribution from a new γ-ray source, denoted below by S, found in my analysis. It is shifted by only $\sim 0.5^\circ$ from NGC 4151. Interestingly, however, the *Fermi Science* tool, `gtfindsrc`, searching for the most likely position of the source of this signal (assuming that it comes from a single source) indicates NGC 4151 rather than S. Namely, the best-fit position (shown by the black cross), is shifted from NGC 4151 by only $8'$. Source S is strongly variable, which hinders a proper assessment of its contribution to the γ-ray signal. The details of my analysis are as follows.

I first examined the significances of γ-ray signals around NGC 4151 by means of their TS values. This revealed three new sources in the region, which were not reported in the *Fermi*/LAT Second Source Catalog and hence not included in the model used in Ackermann *et al.* (2012b). For each of these sources I used the `gtlike` and `gtfindsrc` tools to find their significance, best-fit

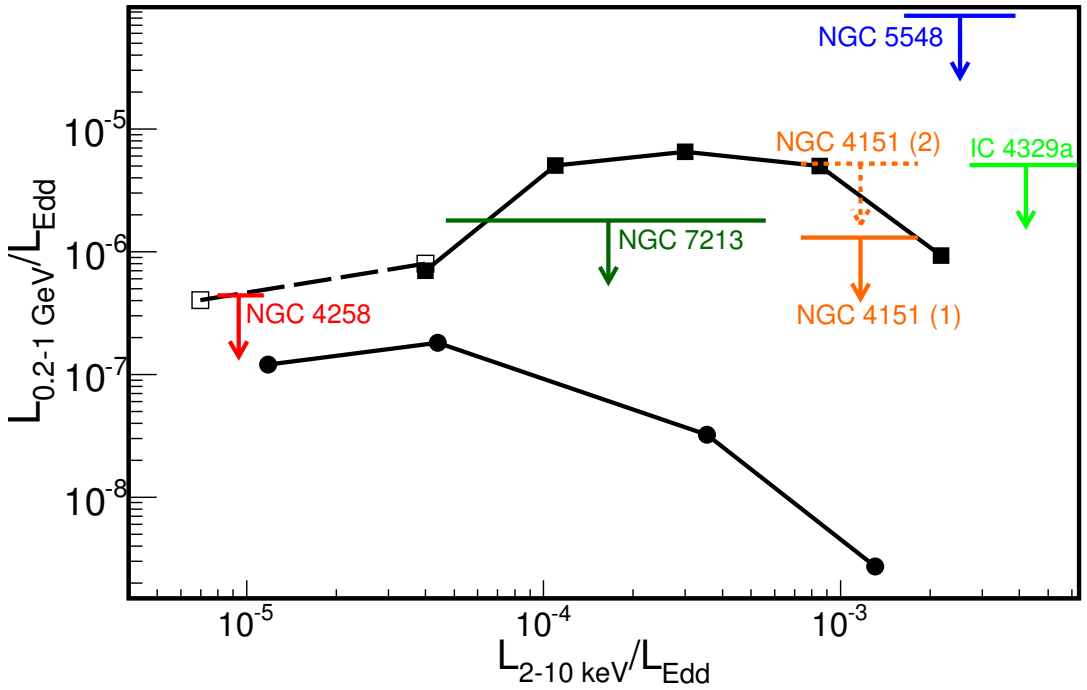

Figure 4.4: $\lambda_{0.2-1\ \mathrm{GeV}}$ as a function of $\lambda_{2-10\ \mathrm{keV}}$, see Tables 4.1 and 4.2 for the observational data. The solid lines are for model T with $\delta = 10^{-3}$; the same as in Figure 3.2. The dashed line with open squares shows an approximate extension to lower $\dot{m}$ (see text) for an edge-on observer for $\beta = 9$ ($\dot{m} = 0.033$, and 0.1).

position, and spectral parameters. Two of them (indicated by the red symbols in Figure 4.5a) have been recently reported in 3FGL, with parameters approximately consistent with those estimated in my analysis. They are 3FGL J1220.2+3434, shifted from NGC 4151 by $\sim 5°$, for which my analysis gives $TS \simeq 164$, $\Gamma \simeq 2.2 \pm 0.1$ and $F_{>0.1\ \mathrm{GeV}} \simeq (8.4 \pm 1.5) \times 10^{-9}$ ph s^{-1} cm^{-2}, and 3FGL J1203.2+3847, shifted from NGC 4151 by $\sim 1.5°$, for which I derived $TS \simeq 32$, $\Gamma \simeq 2.3 \pm 0.2$ and $F_{>0.1\ \mathrm{GeV}} \simeq (3.5 \pm 1.4) \times 10^{-9}$ ph s^{-1} cm^{-2}. These sources are included in the model used for all results presented in this work.

The position of the third source, S, $\sim 0.5°$ from NGC 4151, is determined by several photons with energies between 10 and 20 GeV, which arrived from the same direction (within $\sim 8'$) between December 2011 and June 2013; I assume that the source exhibited an outburst activity during this 1.5-year period, which I denote as period S. Source S is clearly seen in the TS map built for period S alone, see Figure 4.5c, whereas the map built without this period shows only a weak residual, centered on NGC 4151 and not on S, see Figure 4.5a. After subtracting all 3FGL sources, I find for source S (1) TS $\simeq 30$, $\Gamma = 1.78 \pm 0.37$, $F_{>0.1\ \mathrm{GeV}} \simeq 1.2 \times 10^{-9}$ ph s^{-1} cm^{-2} using the data from period S, and (2) TS $\simeq 22$, $\Gamma = 2.17 \pm 0.20$, $F_{>0.1\ \mathrm{GeV}} \simeq 2.1 \times 10^{-9}$ ph s^{-1} cm^{-2} using the full 6.4-year data set. Source S is not reported in 3FGL, which was built using data up to 2012 July, that is, covering only $\sim 30\%$ of period S. For the data from period S, `gtfindsrc` gives the location of S at $\alpha_{J2000} = 12^{\mathrm{h}}11^{\mathrm{m}}27^{\mathrm{s}}$, $\delta_{J2000} = 38°56'48''$. A possible candidate for this source is a BL Lac object, 2E 1209.0+3917, only $\simeq 4'$ from this location.

For a 4.9-year data set, without the period S, `gtlike` shows no signal (TS $\simeq 1.5$) at the S position. The residual seen in the TS map for this data set, Figure 4.5(a), can be fully compensated for by adding the point source at the position of NGC 4151 (compare with panel b), and `gtlike`

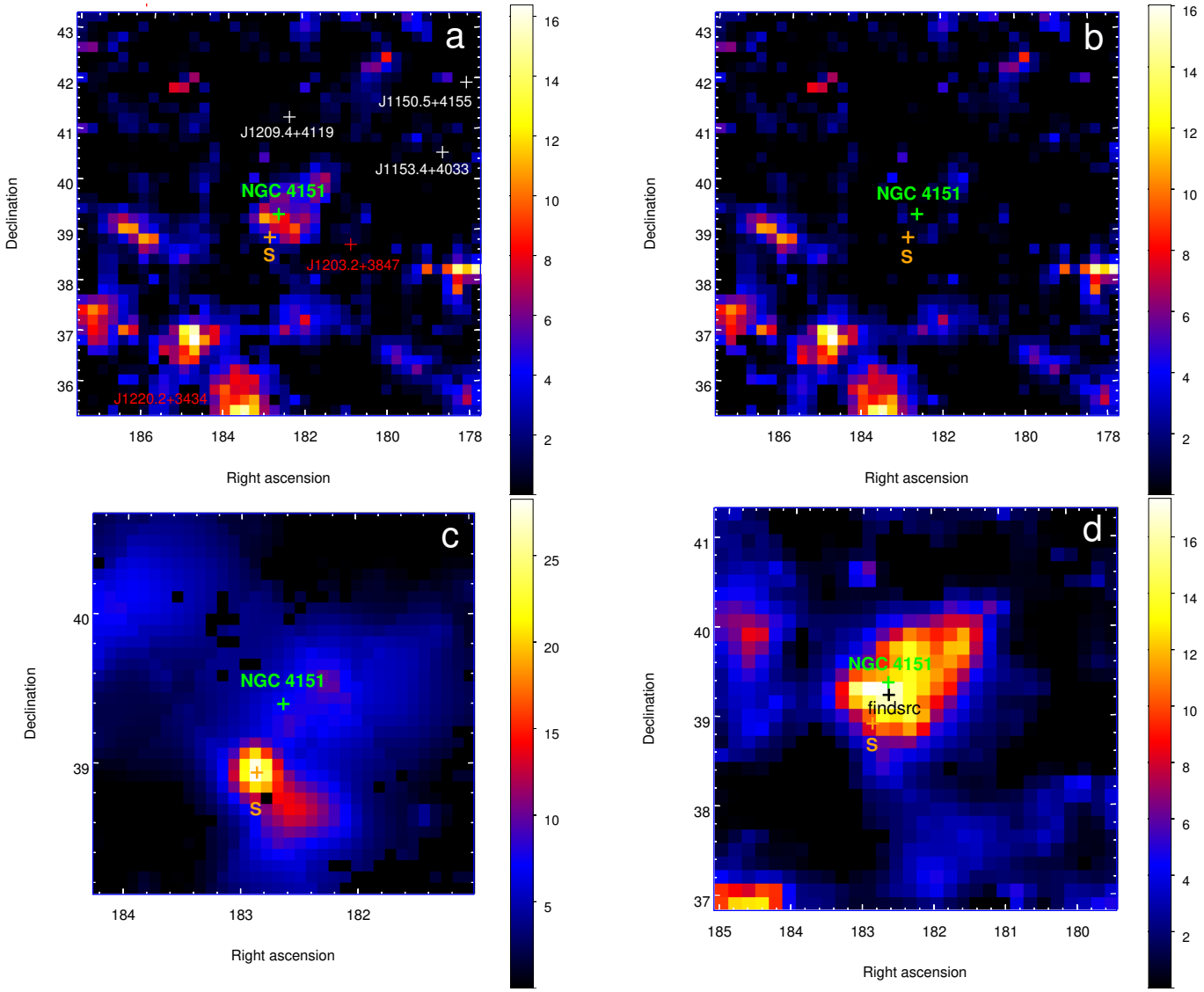

Figure 4.5: TS maps for the region around NGC 4151; in all panels the green cross shows the location of NGC 4151 and the orange cross shows the location of source S. In all panels only the 3FGL sources were subtracted from the maps, except for panel (b), where an additional point source was added at the position of NGC 4151. (a) The $8° \times 8°$ degrees region with a pixel size of $0.2°$. The map was built for the energy range 0.2 – 30 GeV, neglecting period S (see text); the red and white crosses indicate the location of 3FGL sources. (b) The same as in (a), but the model includes a point source at the position of NGC 4151 to compensate for the residual seen in (a). (c) The $2.55° \times 2.55°$ degree region with a pixel size of $0.075°$ for 0.2-30 GeV for period S. (d) The $4.8° \times 4.8°$ region with a pixel size of $0.16°$ for 0.2 - 6 GeV and the full period of 6.4 years; the black cross shows the location of a point source found with `gtfindsrc` under the assumption that the residual seen in the map is produced by a single source; source S is not seen in this map because photons with $E > 10$ GeV are excluded.

gives $TS \simeq 8$, $\Gamma = 2.7 \pm 0.3$ and $F_{>0.1\ \mathrm{GeV}} = (1.5 \pm 0.6) \times 10^{-9}$ for this source.

The presence of a variable source S results in an ambiguity for the UL on the γ-ray flux from NGC 4151, especially below 1 GeV, where the point spread function of LAT is much higher than the angular separation between S and NGC 4151. In my analysis I considered two variants:

(1) assuming that S strongly softened before and after period S, but still provided some contribution

at low energies, I used the full 6.4-year data set and included source S in the model in addition to the 3FGL sources, which yielded the UL values denoted by superscript 'a' in Table 4.2;

(2) assuming that S completely faded away before and after period S, I used the data for 4.9 years without period S and included only the 3FGL sources in the model (i.e., without source S), which yielded the UL values denoted by superscript 'b' in Table 4.2.

ULs on $\lambda_{0.2-1\,\mathrm{GeV}}$ in these two variants differ by a factor of ~ 4, both values are shown in Figure 4.4. The UL on $\lambda_{1-10\,\mathrm{GeV}}$ is much less model-dependent. In Figure 4.3 I use the UL obtained for the above case (1), other ULs for this energy range differ by at most 50% which does not affect my conclusions. I also note that adding source S in the model for the first three years has a negligible effect, see cases 'cd' in Table 4.2. I also checked that my results are not changed if I introduce additional sources to account for several weak residuals located at $\sim 1^\circ$ to $\sim 4^\circ$ from NGC 4151, seen in Figure 4.5(a).

I used the recent dust-parallax distance measurement and the implied stellar-velocity-based mass (see Table 4.1), both higher by $\sim$ 50% than assumed in previous works on high-energy emission from NGC 4151. NGC 4151 shows a moderate X-ray variability with changes of the X-ray flux by up to a factor of ~ 4 between the dim and bright states. Using the adopted distance and M values and the power-law fits of Lubiński *et al.* (2010), I found the intrinsic $\lambda_{2-10\,\mathrm{keV}} \simeq (0.5, 1, 2) \times 10^{-3}$ for the (dim, medium, and bright) state; the parameters of these three states are shown in Figure 4.1). The average *Swift*/BAT flux during the considered *Fermi*/LAT observations is higher by a factor 1.2 than the flux of the medium state, see Figure 4.2b.

As we see in Figures 4.3 and 4.4, the ULs on both $\lambda_{0.2-1\,\mathrm{GeV}}$ and $\lambda_{1-10\,\mathrm{GeV}}$ found for NGC 4151 give some interesting constraints on the parameters of the hot flow model. For $\delta = 10^{-3}$, model N overpredicts $\lambda_{1-10\,\mathrm{GeV}}$ by a factor of several, regardless of a or β values. Then, if the accretion power is provided mostly to protons (and then transferred to electrons in Coulomb interactions) the efficiency of relativistic acceleration of protons is limited to $\eta_\mathrm{p} \lesssim 0.2$.

For $\delta = 0.5$, the model predictions for $\lambda_{1-10\,\mathrm{GeV}}$ are below the UL value (except for model N with $a = 0$). However, as noted in Chapter 3.3.2, the much lower $\lambda_{1-10\,\mathrm{GeV}}$ predicted by large-δ models is accompanied by much lower τ. The X-ray spectrum of NGC 4151 is precisely measured, at least in the bright state, and allows testing this property. Fits of the bright-state spectrum with the slab `compPS` model in Lubiński *et al.* (2010) give $\tau^\mathrm{PS} \simeq 1.3$. To compare it with my model predictions, I simulated the X-ray spectra for my models with $\lambda_{2-10\,\mathrm{keV}} \simeq 0.002$; I used the *INTEGRAL*/ISGRI response function and assumed the normalization corresponding to the bright state of NGC 4151. Then, the simulated spectra were fitted with the slab `compPS` model. For $\delta = 10^{-3}$, the best fit has $\tau^\mathrm{PS} \simeq 1.1$ (model $\mathrm{H}_{0.1}$ with $a = 0.95, \beta = 1, \dot{m} = 0.65$). For $\delta = 0.5$, all simulated spectra were fitted with $\tau^\mathrm{PS} \lesssim 0.5$. I conclude that large-$\delta$ models appear to be inconsistent with the X-ray data.

The above conclusions favor models with mostly thermal distribution of protons. Figure 4.4 shows that $\lambda_{0.2-1\,\mathrm{GeV}}$ predicted by model T, compared with with the *Fermi* UL for the above case (1), disfavors models with both a large a and a large β. For case (2), however, the UL is above the model prediction. Unfortunately, NGC 4151 radiates at $\lambda_{2-10\,\mathrm{keV}} \simeq 10^{-3}$, at which r_ph is close to the size of the γ-ray emitting region for thermal protons, so the escaping flux of γ-rays is severely reduced. Stronger constraints on the model can be obtained if NGC 4151 enters the flux level of

the dim state (implying a higher transparency to γ-rays) for a period of at least 1 year.

4.2.3 Updated analysis of NGC 4151 using an extended dataset

Hint of a $\sim 3\sigma$ signal found in my analysis of NGC 4151, noted above and published in Paper 1, motivated me to update this analysis by using a longer dataset. I used data from LAT observations performed between 2008 August 4 and 2017 September 26, which extends the previously used observing time by 2.7 years. I also used here Pass 8 data containing significant improvements over the P7REP release used in my previous analysis. The recently announced FL8Y (Chapter 2.3.5) reports a new source (i.e. not reported in 3FGL), FL8Y J1211.6+3902, at the position of the source S found in my previous analysis. It is associated with the BL Lac object, which was suggested in my analysis in Chapter 4.2.2. For brevity and consistency with previous notation I refer to it also in this Chapter as source S. FL8Y based on eight years of LAT observations reports it with the detection significance of 5.5σ and spectral index $\Gamma = 2.05 \pm 0.19$.

Results of my unbinned analysis are presented in Table 4.3 and Figure 4.6. I first note that the TS map, built by subtracting only 3FGL sources (i.e. S is not subtracted), shows a signal which below 1 GeV (left panel in Figure 4.6) is clearly concentrated around NGC 4151 rather than S. In the 1 – 10 GeV range (right panel in Figure 4.6), the signal appears broader (despite a lower PSF) and covers positions of both NGC 4151 and S.

Source	Γ	F_γ 10^{-9} ph/cm^2/s	TS
NGC 4151	2.46 ± 0.15	2.40 ± 0.79	17.6
S	1.65 ± 0.29	0.25 ± 0.23	18.2

Table 4.3: The photon spectral index, Γ, photon flux above 100 MeV, F_γ, and TS values of power-law fits to NGC 4151 and S using unbinned analysis in the 0.1 – 100 GeV range of 9.1 years of *Fermi*/LAT data.

Table 4.3 shows the power-law fits in the model including both NGC 4151 and S. For NGC 4151, the fit gives a $\simeq 4.2\sigma$ signal, with an increase of the TS value by a factor of ~ 2 compared to my previous findings, despite extending the observation time by less than 50%. S is fitted with a much harder spectrum and a lower significance than given in FL8Y. All these results are consistent with NGC 4151 being an actual, but much softer than S γ-ray source. When both sources are included in the model, they are both fitted with similar TS values which are slightly lower than the formal detection threshold of 5σ. In turn, blind searches used in the catalog construction find the source at the position of S, whose hardness implies that its high energy photons dominate localization of the γ-ray signal. Then, the fit of S with the model neglecting NGC 4151, such as in FL8Y, includes a strong contribution of low energy photons likely emitted by NGC 4151, which gives both an apparently softer spectrum and a larger detection significance for S than my analysis including both sources. I also investigated individual photons from NGC 4151, as facilitated by the *gtsrcprob* tool of the *Fermi Science* package. In particular, it gives 5 photons with energies above 3 GeV and probability of being emitted by NGC 4151 larger than 50% (and probability of coming from S lower than 1%), with the largest energy of about 8 GeV and the probability of 75%. Three of these photons were detected during the additional time included in this updated analysis, i.e.

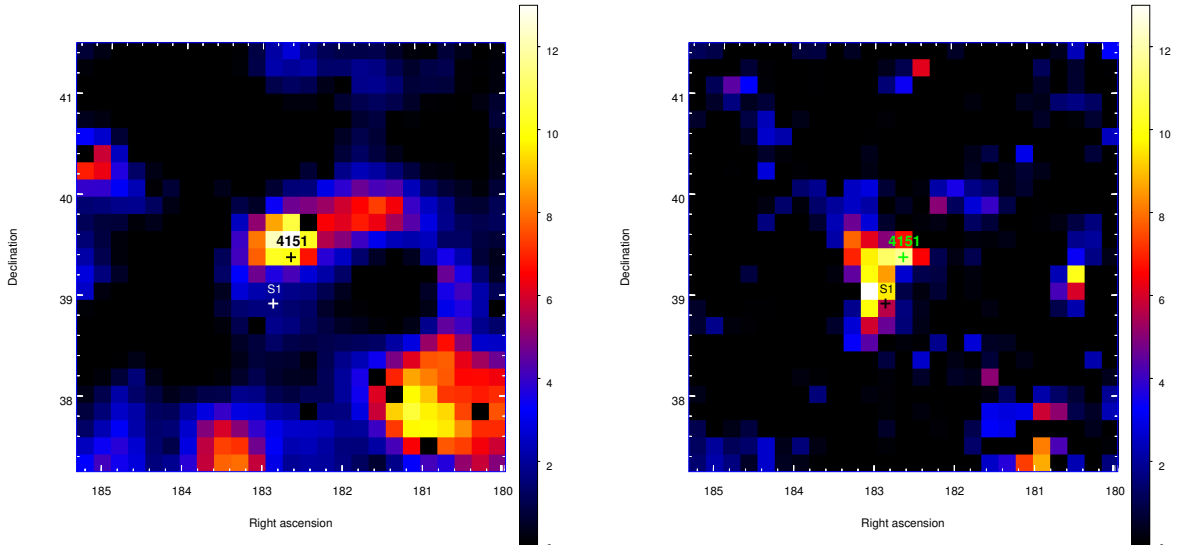

Figure 4.6: TS maps for the 4.25° × 4.25° region around NGC 4151 built using 9.1 years of LAT observations for photons in the 0.3 – 1 GeV (left) 1 – 10 GeV (right) energy range. In both panels only the 3FGL sources were subtracted from the maps. Crosses indicate locations of NGC 4151 and S (which is my model name for FL8Y J1211.6+3902). The pixel size is 0.17°.

after MJD 58017, which is consistent with the significant increase of TS compared to my previous study. As seen in Figure 4.7, the X-ray flux of NGC 4151 was typically lower than its average value during this additional time. As I discussed in Chapter 3, lower X-ray luminosity makes an accretion flow less opaque to $\gamma\gamma$ absorption and, then, favors the escape of γ-ray photons.

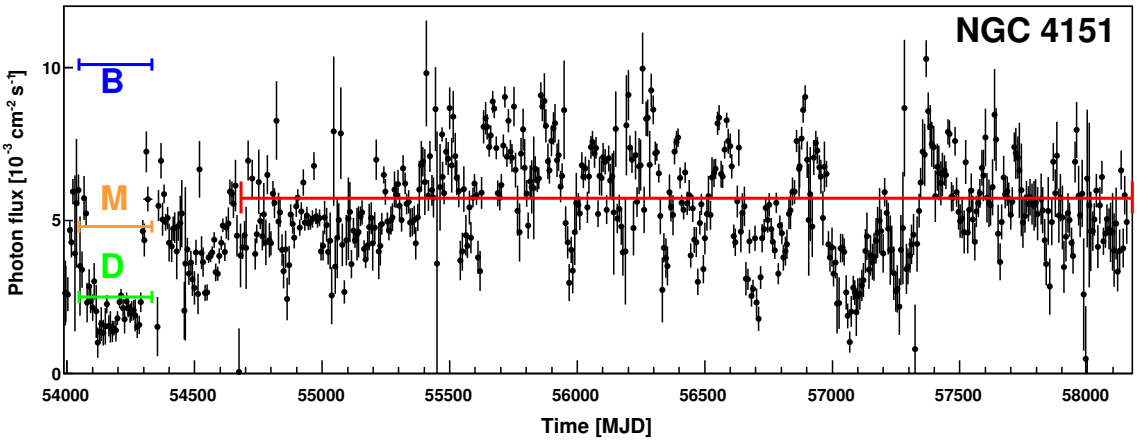

Figure 4.7: The 15 – 50 keV light curve in seven-day bins for NGC 4151 from *Swift*/BAT observations, similar to Figure 4.2b but including an extended LAT observation time considered in Section 4.2.3.

To estimate typical contribution from background in this region of the sky I also made a similar analysis for a fake source inserted in the position of (RA=184°, DEC=40°), i.e. shifted by 1.2° from NGC 4151. No high energy photons were found at this location; all photon probabilities are lower than 0.1%.

4.2.4 NGC 6814

The γ-ray signal from the direction of NGC 6814 with TS = 25.6 was found by Ackermann *et al.* (2012b). However, the source is not reported in 3FGL. It may not have passed the TS > 25 criterion, assumed in 3FGL, as the above value is close to the limit. My analysis, using data for 6.4 years, confirms the signal with TS $\simeq$ 32.3, and my best-fit parameters for a power-law spectrum (see Table 4.2) are approximately consistent with those of Ackermann *et al.* (2012b).

In Figure 4.1 I show the parameters of the intrinsic X-ray emission from spectral fits to *Suzaku* observations in 2011 (Walton *et al.*, 2013). Interestingly, the source is located in the region for an inefficient (thermal synchrotron) source of seed photons. During this observation the source was in a relatively dim state, with the average *Swift*/BAT flux lower by a factor of ~ 1.5 than the average during the *Fermi*/LAT observations, see Figure 4.2d.

As noted above, I considered two values of M for NGC 6814. For both, the measured $F_{1-10\,\mathrm{GeV}}$ gives $\lambda_{1-10\,\mathrm{GeV}}$ exceeding the maximum value predicted for the hot flow (in models N with $\delta = 10^{-3}$), which rules out an origin of the observed γ-ray signal in an inner hot flow. If the γ-ray signal indeed comes from this AGN, one possibility to relate it with the active nucleus involves escape of accelerated protons and their interaction with circumnuclear matter. About 0.1% of the accretion power would need to be carried away by escaping protons to explain the observed γ-ray flux.

4.2.5 NGC 5548 and IC 4329a

The likelihood analysis of the *Fermi*/LAT data does not reveal any significant signal around these two X-ray-bright Seyfert galaxies (in both TS < 1) and therefore I computed the ULs given in Table 4.2.

For NGC 5548, I show in Figure 4.1 the parameters of the power-law fits from Brenneman *et al.* (2012) for seven *Suzaku* observations in 2007. The average *Swift*/BAT flux during the 6.4 years of *Fermi*/LAT observations is equal to the average flux during the *Suzaku* observations, and I used the intrinsic $\lambda_{2-10\,\mathrm{keV}}$ from the fit of Brenneman *et al.* (2012) for the average *Suzaku* spectrum.

For IC 4329a, I show in Figure 4.1 the parameters of the power-law fits from Brenneman *et al.* (2014) for lower and higher flux states during *Suzaku* and *NuSTAR* observations in 2012. I used $\lambda_{2-10\,\mathrm{keV}}$ larger by a factor 1.3 to account for the difference between the average *Swift*/BAT flux for 6.4 years and the flux from measurement simultaneous with *Suzaku*/*NuSTAR* observations, see Figure 4.2c.

Both sources are observed with large $\lambda_{2-10\,\mathrm{keV}}$ corresponding to only approximate applicability of our model. During one observation, NGC 5548 is seen in the area of hot flow solutions with inefficient cooling.

For both objects the ULs on the γ-ray photon flux is lower by a factor of 2–3 times than for NGC 4151. In addition, both sources have a similar L_γ/L_X ratio to NGC 4151 (for IC 4329a it is even lower). However, we see in Figure 4.3 and Figure 4.4 that they insignificantly constrain the hot flow models.

4.2.6 NGC 7213

Despite the large uncertainty in M, NGC 7213 gives interesting constraints on the hot flow model; crucially, it is observed at $\lambda_{2-10\,\mathrm{keV}} \simeq 10^{-4}$, between the X-ray bright Seyfert 1 galaxies discussed above and NGC 4258. The likelihood analysis of the *Fermi*/LAT data does not reveal any significant signal around NGC 7213 (TS < 1), and I computed the ULs given in Table 4.2. In Figure 4.1 I show the parameters from a *Suzaku* observation in 2006 Lobban *et al.* (2010) during which the average flux level was similar to the average during 6.4 years, see Figure 4.2a.

Conclusions from the comparison of the derived UL with the model predictions are similar to those for NGC 4151. As seen in Figure 4.3, the UL for $\lambda_{1-10\,\mathrm{GeV}}$ constrains the nonthermal energy content to $\eta_\mathrm{p} \lesssim 0.1$ for $\delta = 10^{-3}$. Models with $\delta = 0.5$ predicts $\lambda_{1-10\,\mathrm{GeV}}$ below the *Fermi* limit, but again this case may be probably tested using the X-ray data. Namely, these (large-δ) models predict $\tau < 0.1$ for the luminosity of NGC 7213, and at such low optical thickness the thermal Compton spectra deviate significantly from a power-law shape, whereas the *Suzaku* spectrum between 0.6 and 50 keV is described by a simple power-law (Lobban *et al.*, 2010). However, quantitative assessment of the potential disagreement requires a direct fitting of the X-ray data, which is outside the scope of my study.

The UL for $\lambda_{0.2-1\,\mathrm{GeV}}$ rules out a weakly magnetized (high β) flow around a rapidly rotating (high a) black hole, similarly as for NGC 4151.

4.2.7 NGC 4258

The precisely determined parameters of this AGN made it an essential object for the development of the hot flow models (e.g., Lasota *et al.*, 1996). However, it has not been included in previous analyses of the *Fermi*/LAT data. At the position of NGC 4258 I found a weak γ-ray excess above the background, with TS = 9.4. A likelihood analysis of the signal with `gtlike` gives $\Gamma = 2.5 \pm 0.2$, $F \simeq (2.8 \pm 1.2) \times 10^{-9}$ ph s^{-1} cm^{-2}. Despite the presence of this weak residual, the derived ULs on the photon flux yield the tightest constraint on $\lambda_{1-10\,\mathrm{GeV}}$ and $\lambda_{0.2-1\,\mathrm{GeV}}$ of all considered objects, see Table 4.2.

In Figure 4.1 I show parameters of the analysis reported by Reynolds *et al.* (2009) of the *Suzaku* observation in 2006, who also noted that during this observation NGC 4258 increased its intrinsic X-ray luminosity by a factor of ~ 2 relative to the average from *Swift*/BAT measurements. Then, predictions of the model are compared with the LAT ULs using $\lambda_{2-10\,\mathrm{keV}}$ from the *Suzaku* fit reduced by a factor of 2.

For $\delta = 10^{-3}$, model N predicts $\lambda_{1-10\,\mathrm{GeV}}$ strongly exceeding the derived UL, ruling out $\eta_\mathrm{p} \sim 1$. For $\delta = 0.5$, the predicted γ-ray flux is an order of magnitude below the UL value. Again, the X-ray spectrum can be possibly used for an independent assessment of the value of δ.

At $\lambda_{2-10\,\mathrm{keV}} \simeq 10^{-5}$ photons with $E \lesssim 1$ GeV are weakly affected by $\gamma\gamma$ absorption and may escape from the ergosphere (the extremely relativistic region located within $r < 2$). Then, some specific effects of the Kerr metric can be observed, including the gravitational focusing of the photon trajectories toward the equatorial plane which enhances the flux received by edge-on observers - which is likely the case of NGC 4258. Taking it into account, I show the estimated *maximum* $\lambda_{0.2-1\,\mathrm{GeV}}$ that can be expected at $\lambda_{2-10\,\mathrm{keV}} \sim 10^{-5}$ by the dashed line in Figure 4.4.

For $\beta = 9$ this $\lambda_{2-10\,\mathrm{keV}}$ is in the regime where advection of electron energies dominates, i.e. this estimation is not based on a precise solution of our model; I used the scaling of radiative efficiency, $\propto \dot{m}^{0.7}$, found in Xie & Yuan (2012) for low $\dot{m}$, to roughly estimate the X-ray luminosity. We see that even this strongest expected signal is only at the level of the LAT UL.

Finally, I note that similarly as in the case of NGC 4151, for NGC 4258 I also found an increased significance of the γ-ray signal in a longer dataset, however, I also found that in this object the influence from nearby objects is more complex than in NGC 4151, therefore, I skip the discussion of these results here.

4.2.8 Circinus, NGC 1068 and NGC 4945

For the Seyfert 2 galaxies I used the parameters of my analysis in Chapter 5. Of these three AGNs, only NGC 4945 shows rapid variability in the hard X-rays, which indicates that it is a transmission-dominated source and we can directly probe the nuclear emission. In Figure 4.1 I show fits from Puccetti *et al.* (2014) for *NuSTAR* observations in 2013. The average *Swift*/BAT flux agrees with the average flux during the *NuSTAR* observations.

In NGC 1068, the direct X-ray emission is completely obscured along our line of sight and we only see the reflected component. Then, the assessed intrinsic emission is strongly model dependent. I used $\lambda_{2-10\,\mathrm{keV}}$ corresponding to the best-fit of Bauer *et al.* (2015). This assessment, based on the observed reflected component, gives the level of emission from the active nucleus averaged over a long time, possibly over hundreds of years, because a significant fraction of reflection arises at a $\sim$ 100 pc scale (see Bauer *et al.*, 2015). Similarly, the X-ray emission from Circinus is reflection dominated; I used results from Arévalo *et al.* (2014). NGC 1068 and Circinus are not shown in Figure 4.1 because the estimates for their intrinsic Γ_X are model dependent.

Figure 5.2b shows that all three γ-ray-loud Seyfert 2 galaxies agree remarkably well after scaling by their central black hole masses, with $\lambda_{2-10\,\mathrm{keV}} \simeq 0.02$ and $\lambda_{1-10\,\mathrm{GeV}} \simeq 3 \times 10^{-5}$ in all three. I also note that their $L_{1-10\,\mathrm{GeV}}/L_{2-10\,\mathrm{keV}}$ ratio does not exceed the limit on the luminosity ratio in other AGNs, except for that corresponding to the UL in IC 4329a for $\Gamma = 2.7$.

4.2.9 Centaurus A

The interpretation of the high-energy spectrum of Cen A has some open questions. Its X-ray emission may contain contribution from both the jet and the accretion flow. The latter origin is supported e.g. by the thermal-like cutoff, claimed in Beckmann *et al.* (2011). As seen in Figure 4.1, Cen A is located in the area of the $\lambda_{2-10\,\mathrm{keV}}$–$\Gamma_\mathrm{X}$ plane occupied by Seyfert galaxies. In Figure 4.1 I show the parameters from three *Suzaku* observations in 2009 (Fukazawa *et al.*, 2011). Fukazawa *et al.* (2011) also noted hints for a harder power-law component, with $\Gamma_\mathrm{X} < 1.6$, weakly contributing below 100 keV, which may represent emission from the jet. The main contribution to the γ-ray emission of Cen A most likely comes from the jet. However, Sahakyan *et al.* (2013) found evidence for a second component, an order of magnitude less luminous than the main γ-ray component. This weaker component has a hard spectrum and dominates above $\sim$ 4 GeV. Assuming that this component extends down to 1 GeV with the same slope, I find $\lambda_{1-10\,\mathrm{GeV}} \simeq 1.7 \times 10^{-6}$. Based on a comparison with predictions of model $\mathrm{H}_{0.1}$, this component can be emitted from a flow with small δ and $\eta_\mathrm{p} \simeq 0.1 - 0.2$ (slightly dependent on plasma magnetization).

The *Swift*/BAT flux level during the 2009 *Suzaku* observations is equal to the average flux during the *Fermi*/LAT data-taking period used for the analysis in Sahakyan *et al.* (2013).

4.3 Nonthermal electrons

I now briefly discuss constraints on the acceleration of electrons resulting from the *Fermi*/LAT ULs. Here I assume that the electrons are accelerated to the power-law distribution with the acceleration index s_e and that their acceleration efficiency is η_e, i.e. the power used for the nonthermal acceleration is $Q_{acc} = \eta_e \delta Q_{diss}$, where Q_{diss} is the total power dissipated in the flow.

Conditions in the inner parts of hot flows surrounding supermassive black holes allow for acceleration of electrons to GeV energies; for instance, using equation (7) from Zdziarski *et al.* (2009) for the maximum Lorentz factor limited by the synchrotron losses I found $\gamma_{max} \sim 10^5 - 10^6$ for the typical magnetic field strength of $B \sim (10^2 - 10^4)$ G. The synchrotron emission of these electrons extends up to ~ 10 MeV, so they can produce photons in the LAT energy range only by Compton scattering. The description of nonthermal Compton emission was implemented in our MC code and I performed simulations with $\gamma_{max} = 2 \times 10^4$, for which the nonthermal Compton spectrum extends up to ~ 10 GeV.

The level of γ-ray emission from the nonthermal Compton scattering in the LAT energy range depends primarily on s_e. I found that for $s_e \gtrsim 2.4$ and $\eta_e = 1$, the predicted values of both $\lambda_{0.2-1\,\mathrm{GeV}}$ and $\lambda_{1-10\,\mathrm{GeV}}$ are below any UL derived in my analysis of the LAT data. For $s_e \lesssim 2.4$, the γ-ray Compton component for $\eta_e = 1$ exceeds the ULs for NGC 4258, NGC 7213 and NGC 4151, then, for such s_e the fraction of accretion power used for nonthermal acceleration can be constrained. For example, it is limited to $\lesssim 0.05 Q_{diss}$ (i.e. $\eta_e \lesssim 0.1$ for $\delta = 0.5$) if $s_e \simeq 2$.

4.4 Discussion

Observational assessment of nonthermal acceleration processes in astrophysical plasmas is an essential issue. Hot flows in which ultra-relativistic acceleration of protons takes place can be considered a source of neutrinos detected by *IceCube* (e.g., Kimura *et al.*, 2015). Accretion flows should also be strong acceleration sites according to hybrid thermal and nonthermal Comptonization models (e.g., Vurm & Poutanen, 2009; Malzac & Belmont, 2009; Veledina *et al.*, 2011) that are widely applied to explain X-ray spectra of accreting black holes.

Observational evidence of the presence of non-thermal particles in accretion flows includes detection of MeV tails (e.g., Droulans *et al.*, 2010; Zdziarski *et al.*, 2012) and patterns of optical/infrared evolution (Poutanen *et al.*, 2014), both observed in stellar black-hole systems. However, these features are produced by nonthermal electrons, which may come from pion decay, and in principle, they do not require direct acceleration.

Observations in the GeV range provide the means to directly measure the efficiency of proton acceleration in hot flows. The obtained ULs for $F_{1-10\,\mathrm{GeV}}$ in NGC 4258, NGC 7213 and NGC 4151 constrain the fraction of accretion power used for relativistic acceleration of protons to at most $\eta_p \simeq 0.1$ if δ is small. Remarkably, these three AGNs allow probing various parts of the flow because at their $\lambda_{2-10\,\mathrm{keV}} \sim 10^{-5}$, 10^{-4} and 10^{-3}, the GeV radiation produced at a few, about ten,

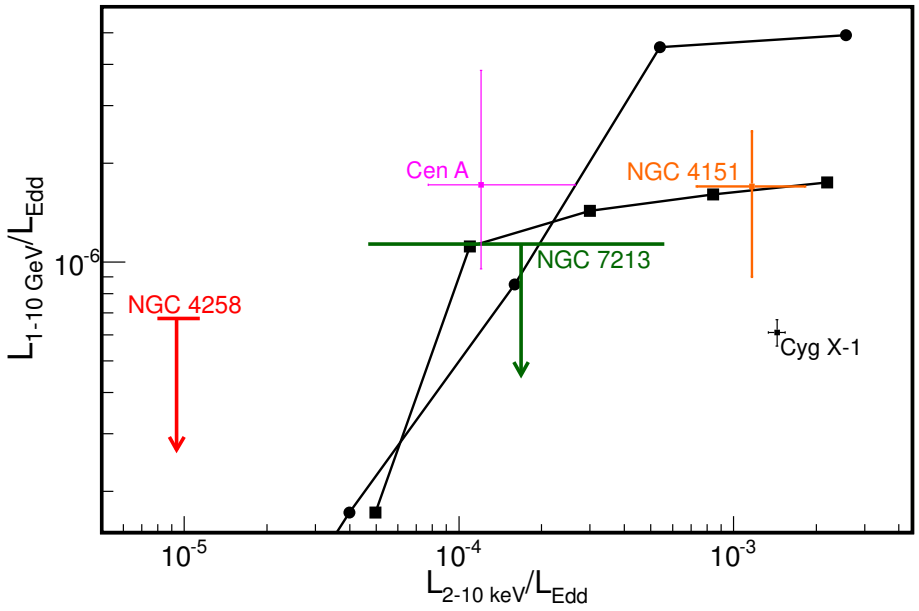

Figure 4.8: $\lambda_{1-10\,\mathrm{GeV}}$ as a function of $\lambda_{2-10\,\mathrm{keV}}$, similar to Figure 4.3, but instead of the UL for NGC 4151 here I show $\lambda_{1-10\,\mathrm{GeV}}$ of the $\sim 4\sigma$ fit from the updated analysis in Chapter 4.2.3. I also show here $\lambda_{1-10\,\mathrm{GeV}}$ for Cen A (see text) and for Cyg X-1 in the hard state. Parameters for the latter, adopted from Malyshev *et al.* (2013), are consistent with more recent measurements discussed in Chapter 6. The solid line with squares is for model $\mathrm{H}_{0.1}$ with $\delta = 10^{-3}$, $a = 0.95$ and $\beta = 9$, the same as in Figure 4.3. The solid line with circles is for the only model with large δ which predicts $\lambda_{1-10\,\mathrm{GeV}}$ comparable with the current LAT sensitivity for some Seyferts; specifically, model N with $\delta = 0.5$, $a = 0$, $\beta = 9$.

and several tens of R_g, respectively, would dominate the 1–10 GeV flux predicted by the model.

The component dominating the core emission of Centaurus A above ~ 4 GeV may come from a hot flow in which $\eta_\mathrm{p} \simeq 0.1 - 0.2$. If it does, the efficiency of nonthermal processes in this AGN would be higher at least by a factor of ~ 2 than in NGC 7213 (see Figure 4.8), which has similar $\lambda_{2-10\,\mathrm{keV}}$. This might reflect differences between flows powering radio-loud and radio-quiet AGNs.

Interestingly, the γ-ray flux corresponding to my $\sim 4\sigma$ fit of NGC 4151 in Chapter 4.2.3, shown in Figure 4.8, agrees with our model prediction for $\eta_\mathrm{p} \simeq 0.1$. Also interestingly, its $L_{1-10\,\mathrm{GeV}}/L_{2-10\,\mathrm{keV}} \sim 10^{-3}$ is almost the same as in the γ-ray loud Seyfert 2s.

In Figure 4.8 I also show the measurement for Cyg X-1 discussed in Chapter 6. However, I note that in this source the transition between the hard and soft state occurs at relatively low λ (see Chapter 6) and the cold disc in its hard state may extend already quite close to the black hole. Then, comparison with our model prediction should be made with some caution. In particular, the GeV photons may be strongly absorbed in the soft X-ray radiation of such a disc.

Finally, the γ-ray loud Seyfert galaxies, NGC 4945, NGC 1068 and Circinus, appear to be the most active AGNs in the local Universe (as measured by λ). All three exhibit starburst activities, which likely explains enhanced fueling of their active nuclei, as Seyfert galaxies show a strong correlation between nuclear star-formation and the AGN luminosity (e.g., Diamond-Stanic & Rieke, 2012). Masses of supermassive black holes in Circinus, NGC 1068 and NGC 4945 are precisely determined by H_20 megamaser measurements. These measured M imply an interesting similarity of the values of both $\lambda_{2-10\,\mathrm{keV}}$ and $\lambda_{1-10\,\mathrm{GeV}}$ in all three objects, which motivates my

analysis in the next Chapter.

Chapter 5

The X/γ-ray correlation in NGC 4945 and the nature of its γ-ray source

5.1 Introduction

NGC 4945 is one of the nearest AGNs (D = 3.8 Mpc), with the black hole mass of $M = 1.4{\times}10^6 M_\odot$ from megamaser measurements (Greenhill *et al.*, 1997). It is the brightest Seyfert 2 galaxy in the hard X-ray range, radiating at a variable rate of $L/L_{\rm Edd} \sim 0.1$ (Madejski *et al.*, 2000). Its X-ray spectrum shows a strong photoelectric absorption, with a column density $N_{\rm H} \simeq 4 \times 10^{24}$ cm^{-2} (Done *et al.*, 2003), at which its nucleus can be directly seen above $\sim$ 8 keV. The observed hard X-ray radiation is highly variable, by a factor of several on a time scale of days, confirming that it is a transmission-dominated Compton-thick AGN.

NGC 4945 is also one of a few radio-quiet AGNs detected by *Fermi*/LAT (Abdo *et al.*, 2010b; Lenain *et al.*, 2010). The origin of this γ-ray signal is unclear, as this galaxy hosts a circumnuclear starburst (e.g. Lenc & Tingay, 2009) which may also account for this emission (e.g. Ohm, 2016). Variability studies are crucial to disentangle the role of the AGN and starburst activities, but overcoming the weakness of the γ-ray signal is a major issue for such studies. The apparent lack of the γ-ray variability, assessed in Ackermann *et al.* (2012a), could favor the γ-ray production dominated by starburst processes. However, the 3-month intervals used in Ackermann *et al.* (2012a) are too short to accumulate a statistically significant γ-ray signal from this galaxy, whereas its AGN exhibits an approximately constant activity on such a time-scale.

In this Chapter I revisit the issue of γ-ray variability in NGC 4945 and I search for a correlation between its X-ray and γ-ray emission. I did not attempt to find it in observations carried out continuously over the time sufficient for an adequate significance of the LAT measurement (i.e. at least a year), as this could only probe the averaged out X-ray as well as γ-ray emission, even if the latter followed the changes of the former. Instead, I considered intermittent data sets including LAT data corresponding to different X-ray flux levels. This allowed us to reveal the change of the γ-ray spectrum related with the change of the X-ray flux. The implied constraints on the γ-ray source, and comparison with other radio-quiet galaxies detected in γ-rays, are discussed in Chapter 5.4

5.2 Observational data

I use the *Fermi*/LAT and *Swift*/BAT data from observations performed by these detectors between 2008 August 4 and 2016 August 15. NGC 4945 exhibits hard X-ray flux variations of a factor of two on a timescale of 2×10^4 s and of a factor of five on a timescale of several days (Madejski *et al.*, 2000; Puccetti *et al.*, 2014). Then, the daily count rate values, $\mathcal{F}_{\rm X}$, from the BAT survey program (Krimm *et al.*, 2013) are convenient to probe changes in this source. Using them I divide all days with contemporaneous LAT and BAT measurements into MJD sets comprising days with various $\mathcal{F}_{\rm X}$ ranges, which then allows us to study the γ-ray spectral parameters corresponding to different activity levels of the AGN.

5.2.1 BAT

The good quality data (with `DATA_FLAG=0`) from BAT light curves[1] in the 15–50 keV range allow to determine $\mathcal{F}_{\rm X}$ for 2783 days out of 2821 days in the considered period of time. I split them into two approximately equal MJD sets, containing days with $\mathcal{F}_{\rm X}$ lower (set L; 1393 days) and higher (set H; 1390 days) than 1.71×10^{-3} cts cm^{-2} s^{-1}. To test the effect of possible misclassification of the X-ray flux level due to a short exposure time, I also define sets denoted by L5,H5 and L10,H10, using a similar procedure but only for days with the total exposure time of at least 5 and 10 ksec, respectively. Here, with the median rate of $\mathcal{F}_{\rm X} = 1.67 \times 10^{-3}$ cts cm^{-2} s^{-1}, I get 920 days in both L5 and H5, and with $\mathcal{F}_{\rm X} = 1.69 \times 10^{-3}$ cts cm^{-2} s^{-1}, I get 418 days in L10 and 420 days in H10. The average BAT count rate for each set, $\overline{\mathcal{F}}_{\rm X}$, computed using equations A2 in Ajello *et al.* (2008), is given in Table 5.1. $\overline{\mathcal{F}}_{\rm X}$ in L,L5,L10 is lower by a factor of ∼5 than in H,H5,H10.

5.2.2 LAT

I performed the maximum likelihood analysis using `Pass 8` LAT data in the 0.1–100 GeV range and `v10r0p5` *Fermi* Science Tools with the P8R2_SOURCE_V6 instrument response function. I used the standard templates for the Galactic (`gll_iem_v06.fits`) and the isotropic (`iso_P8R2_SOURCE_V6_v06.txt`) backgrounds.

My results presented in Chapter 5.3 were obtained using unbinned likelihood analysis, for which events were selected from the region with the radius of 10° centered on the position of NGC 4945. I took into account all sources reported in the 4-year LAT Catalog (Acero *et al.*, 2015: 3FGL) within the radius of 15° around NGC 4945. To check the effect of energy dispersion[2], which currently cannot be included in the unbinned analysis, I also performed the binned analysis, using 20° × 20° square region centered on NGC 4945. I found that the dispersion correction insignificantly affects my results.

In the TS maps of the region of interest, obtained by subtracting the best-fit model from the data, I do not find residuals indicating presence of unmodeled sources which could affect my analysis. However, I note contamination of the γ-ray signal below 1 GeV, resulting in an apparent extension toward the bottom left corner in Figures 5.1ab, by 3FGL J1251.0-4943 (the γ-ray counterpart of BL Lac object PMN J1326 5256) located at (R.A., Decl.) = (201.7°, −52.9°).

[1] http://swift.gsfc.nasa.gov/results/transients

[2] http://fermi.gsfc.nasa.gov/ssc/data/analysis/documentation/ Pass8_edisp_usage.html

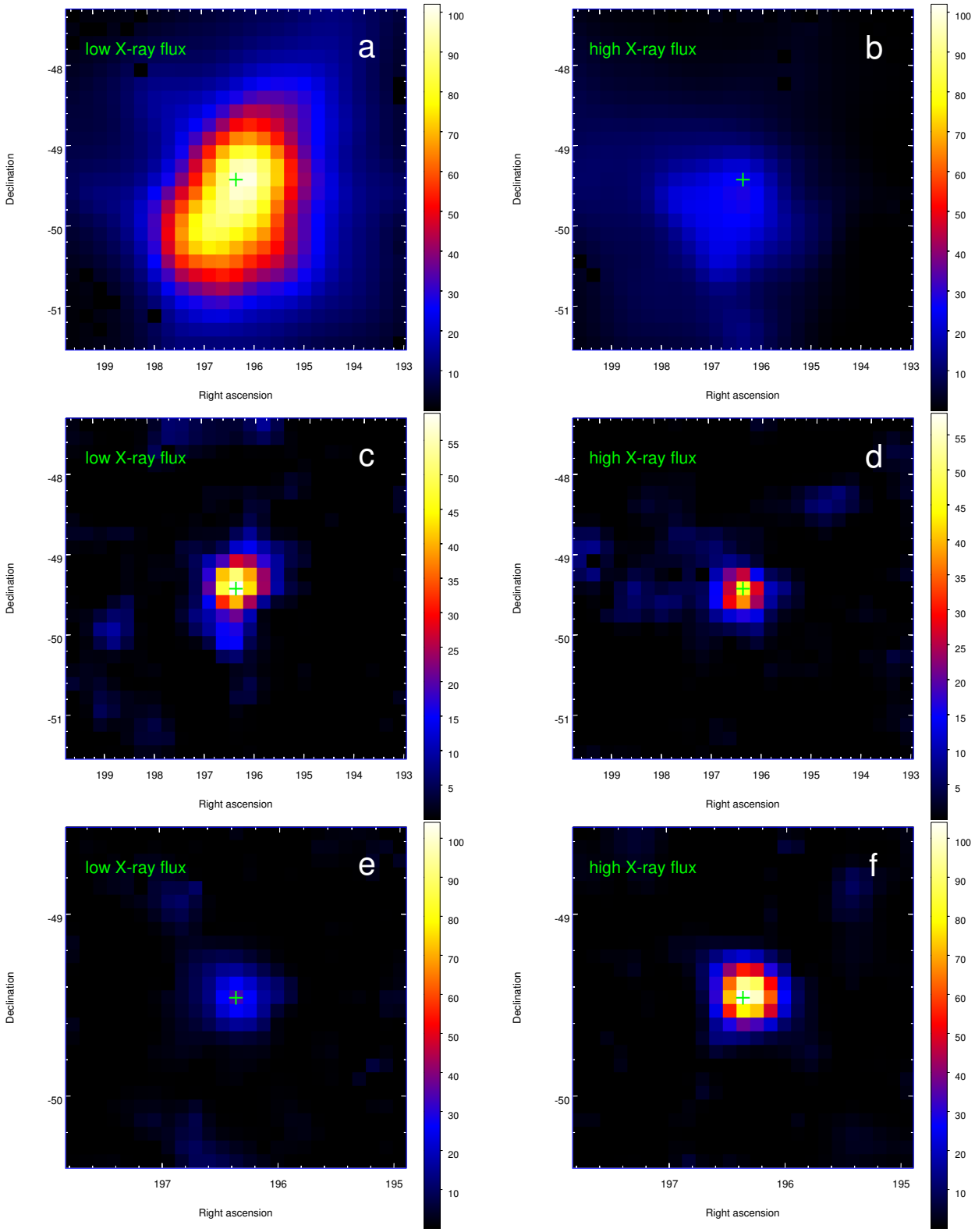

Figure 5.1: TS maps for the region around NGC 4945 built using the events detected during the low (dataset L; left maps) and high (dataset H; right maps) X-ray flux levels. Top maps are for events with $E < 1$ GeV with a pixel size of 0.17°; middle maps are for events with E between 1 and 3 GeV with a pixel size of 0.17°; bottom maps are for events with $E > 3$ GeV with a pixel size of 0.075°. In all panels the green cross shows the location of NGC 4945. In all panels, the 3FGL sources were subtracted from the maps (except for 3FGL J1305.4-4926 which is the γ-ray counterpart of this galaxy).

It is a factor of $\sim$ 2.6 brighter in γ-rays than NGC 4945 and at the distance of 4.8° it may weakly contribute to the flux below 1 GeV measured in NGC 4945. The fitted parameters of this source are the same in all considered data sets, so its presence does not affect my conclusions on spectral changes in NGC 4945.

Results reported in Chapter 5.3 were obtained in models with spectral parameters of all sources adjusted to maximize the likelihood of the fit for a given dataset. The spectral energy distributions (SED) were obtained by fixing the spectral index, Γ, for NGC 4945 to the value from the power-law fit to a given dataset. However, to verify if variability in nearby sources could affect my results, I also repeated the analysis for datasets L, L5, L10, H, H5, and H10 using the model with spectral parameters of the background sources frozen to the values of the best-fit model to the total LAT data set (i.e. 2821 days; dataset T); below I refer to this variant as model T. For SEDs computed with model T I also fixed $\Gamma = 2.33$ (from the power-law fit to dataset T) for NGC 4945. I found that it did not affect my results, i.e. using model T for the background sources I obtained parameters of the power-law fits consistent with those given in Table 5.1 as well as TS maps consistent with those shown in Figure 5.1 (i.e. showing similar TS values at the position of NGC 4945). Also SEDs (Figure 5.2b) are weakly affected by applying model T, except for the lowest bin, 0.1–0.3 GeV, which shows a moderate dependence on the applied model. The difference of fluxes between L and H in this (0.1–0.3 GeV) bin decreases from a factor of $\simeq$ 2.5 (in the best-fit models shown in Figure 5.2) to 1.7 (with model T). The change resulting from applying model T to SED of dataset L is shown in Figure 5.6.

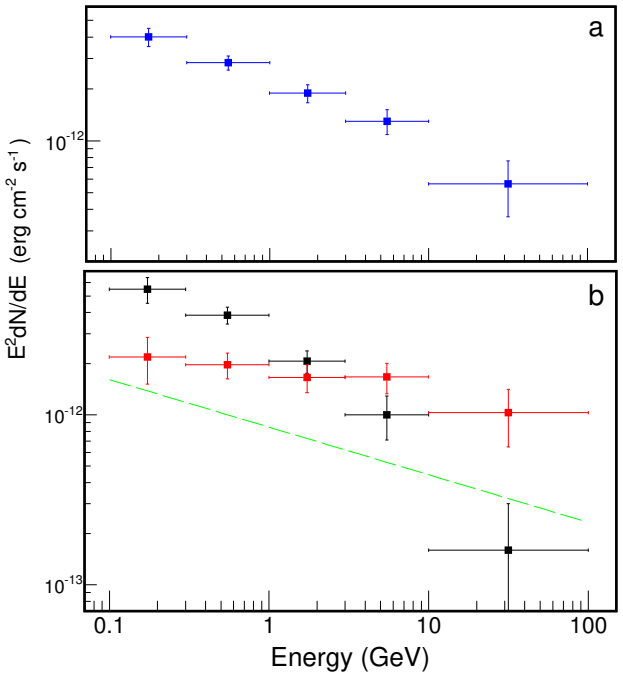

Figure 5.2: NGC 4945 spectral energy distributions for the total LAT dataset T (panel a) and datasets resolved by the X-ray flux (panel b); SED for L is shown in black and SED for H is shown in red. The dashed green line in (b) represents the γ-ray spectrum of M 82 (the power-law fit in Table 5.1) scaled by the difference of IR luminosities (linear scaling with $L_{\rm IR}$ assumed) and distances between M 82 and NGC 4945.

For a comparison of γ-ray loud galaxies in Chapter 5.4, I analyzed the LAT data from 8 years

Table 5.1: Results of the power-law fits in the 0.1–100 GeV range to NGC 4945 using data sets defined in Section 5.2 (the number of days is given in parentheses) and to other starbursts and Seyfert 2 galaxies.

	$\overline{\mathcal{F}}_X$	Γ	$\mathcal{F}_\gamma$	TS
NGC 4945 data sets				
L (1393)	0.54 ± 0.03	2.47 ± 0.07	2.6 ± 0.3	221
H (1390)	2.87 ± 0.04	2.11 ± 0.08	1.2 ± 0.2	189
L5 (920)	0.57 ± 0.04	2.46 ± 0.09	2.5 ± 0.4	136
H5 (920)	2.75 ± 0.04	2.05 ± 0.09	1.1 ± 0.2	140
L10 (418)	0.60 ± 0.04	2.56 ± 0.10	3.1 ± 0.4	80
H10 (420)	2.66 ± 0.05	2.07 ± 0.11	1.0 ± 0.2	46
T (2821)	1.59 ± 0.02	2.33 ± 0.05	1.9 ± 0.2	410
other objects				
M 82		2.28 ± 0.04	1.8 ± 0.1	1010
NGC 253		2.14 ± 0.05	1.1 ± 0.1	616
Circinus		2.43 ± 0.09	2.0 ± 0.3	103
NGC 1068		2.47 ± 0.05	1.6 ± 0.1	357

$\overline{\mathcal{F}}_X$ is the average BAT count rate in the 15–50 keV range in units of 10^{-3} cts cm^{-2} s^{-1}; Γ is the γ-ray power-law photon index and $\mathcal{F}_\gamma$ is the photon flux in the 0.1–100 GeV range in units of 10^{-8} ph cm^{-2} s^{-1}.

of observations of NGC 253, M 82, NGC 1068 and Circinus; in the model for NGC 1068, in addition to 3FGL sources, I included the new γ-ray source, at the distance of $\sim 4^\circ$, found in Lamastra *et al.* (2016). My luminosities in the 0.1–100 GeV range, L_γ, for NGC 4945 and NGC 1068, placing them at/above the calorimetric limit in Figure 5.7, are by a factor of 1.5 and 1.7, respectively, larger than found in Ackermann *et al.* (2012a). The difference results from analysis improvements in Pass 8 data with respect to Pass 7 data used by Ackermann *et al.* (2012a). For NGC 1068 I note a marginal hint for the change of the γ-ray spectrum. For the first 3 years of LAT observations, the same as used in Ackermann *et al.* (2012a), I found $\Gamma = 2.37 \pm 0.09$ and $\mathcal{F}_\gamma = (1.3 \pm 0.2) \times 10^{-8}$ ph cm^{-2} s^{-1}, whereas for the last four years of my dataset (i.e. after August 2012), $\Gamma = 2.51 \pm 0.08$ and $\mathcal{F}_\gamma = (1.7 \pm 0.2) \times 10^{-8}$ ph cm^{-2} s^{-1}.

5.3 Results

My main results are presented in Figures 5.1 and 5.2 and Table 5.1. All my results indicate that the γ-ray spectrum of NGC 4945 changes with the change of its hard X-ray flux. The significance of the spectral difference between the power-law fits for datasets H and L is $\simeq 5\sigma$. SEDs shown in Figure 5.2b indicate that a large difference of the detection significance between H and L should be seen both below 1 GeV and above 3 GeV. Indeed, with an equal exposure time in both datasets, the change of the γ-ray signal is seen in the TS maps (see Figure 5.1) for both 0.1–1 GeV and 3–100 GeV with a formal statistical significance of $\simeq 9\sigma$ (determined as $\sqrt{|\mathrm{TS_L} - \mathrm{TS_H}|}$, where $\mathrm{TS_X}$

is the test statistic at the position of NGC 4945 in dataset X). Note that these results, indicating the change of the γ-ray signal at low and high energies, are mutually independent. My results for data sets L5/H5 and L10/H10 are consistent with those shown in Figures 5.1 and 5.2, see e.g. Figure 5.3 (NGC 4945 is not detected below 1 GeV in H10 and above 3 GeV in L10, so SEDs cannot be shown in full energy ranges for the 10 ks datasets).

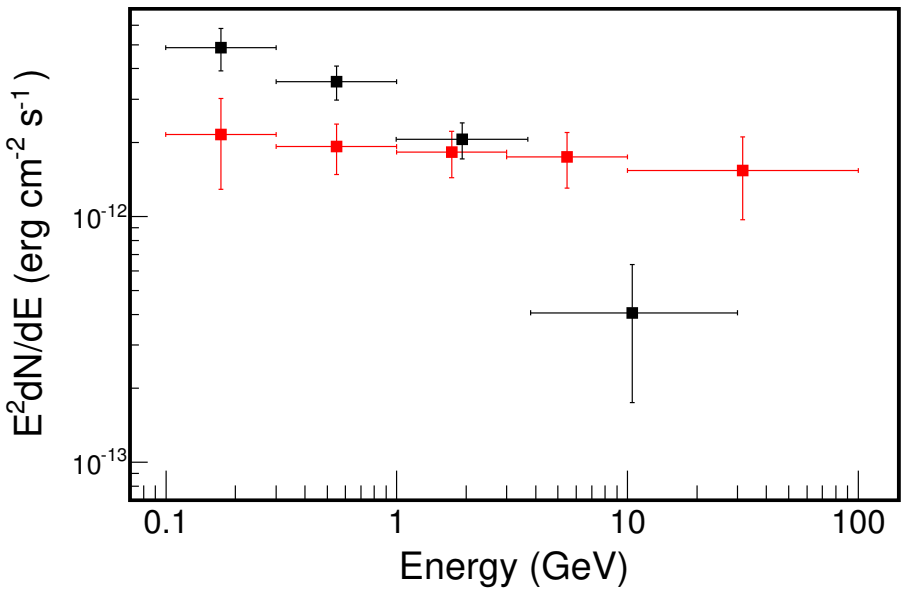

Figure 5.3: SEDs for X-ray flux resolved datasets, similar to Figure 5.2, but for L5 (black) and H5 (red).

I also performed the division of LAT observations into datasets corresponding to smaller ranges of $\mathcal{F}_X$ than those of L and H. Again, I find a systematic indication of hardening of the γ-ray spectrum with the increase of the X-ray flux, see Figure 5.4, although obviously the statistical uncertainty on spectral parameters increases with a decreasing size of datasets. Using all fitting results shown in Figure 5.4 I find the Pearson correlation coefficient for the Γ–$\overline{\mathcal{F}}_X$ relation, weighted by the inverse of spectral index uncertainty, of $r \simeq -0.97$ with the p-value of $\simeq 2 \times 10^{-6}$.

I have made a number of tests for LAT datasets selected without the X-ray flux criterion and in all cases I found that they are consistent, within uncertainties, with the results for the total LAT dataset T. An example is shown in Figure 5.5b, were power-law fits to datasets of 800 days randomly drawn from set T are compared with fits to datasets of 800 days randomly drawn from set L or H. We see that the latter, i.e. black and red points, occupy two separate areas in the parameter plane. The green points for datasets mixing various X-ray flux levels have a larger spread of fitted parameters than those for NGC 253 and M 82 (whose γ-ray signals should be constant in time; Figure 5.5a), reflecting larger uncertainties on Γ in 800-day datasets for NGC 4945. However, it is much smaller than the overall spread of parameters for $\mathcal{F}_X$-resolved datasets.

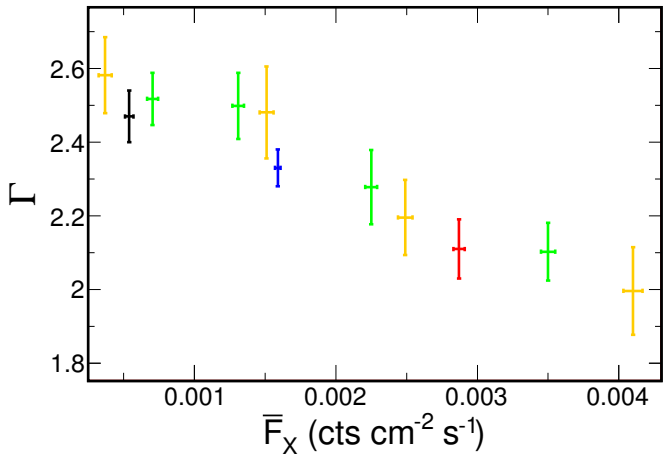

Figure 5.4: Photon spectral index of power-law fits in the 0.1–100 GeV range as a function of $\overline{\mathcal{F}}_X$. The yellow points are for datasets containing 620 days in consecutive, non-overlapping ranges of $\mathcal{F}_X$. The green points are for datasets containing 900 days in similar but partially overlapping ranges of $\mathcal{F}_X$. The black, blue and red point is for dataset L, T and H.

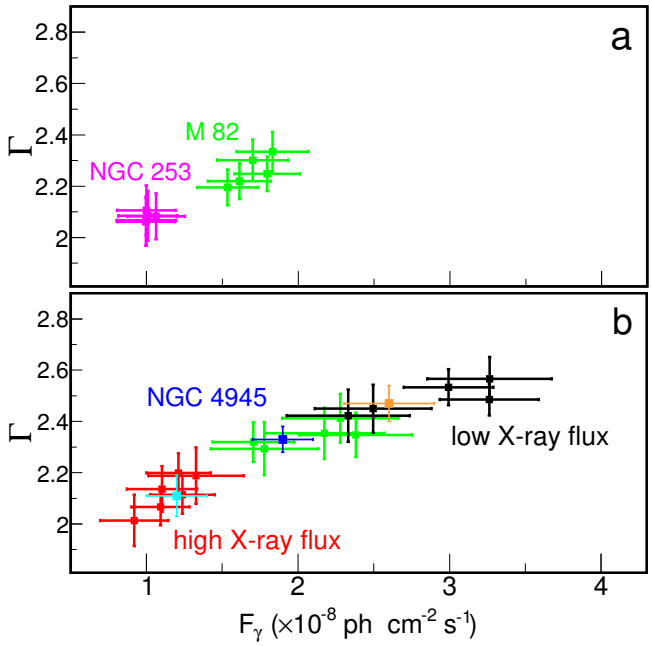

Figure 5.5: Parameters of the power-law fits in the 0.1–100 GeV range. Panel (a) is for datasets comprising 800 days randomly drawn from the total LAT dataset of NGC 253 (magenta) and M 82 (green). Panel (b) is for datasets comprising 800 days randomly drawn from set T (green), L (black) and H (red) in NGC 4945. The blue, orange and cyan points in (b) show parameters of power-law fits to dataset T, L and H, respectively, as given in Table 5.1.

Using additional 10 datasets of 400 days drawn from set L and 10 such datasets drawn from H, which again give parameters distributed in separate areas in the parameter plane similar to that shown in Figure 5.5b, I find that these two samples (i.e. drawn from either L or H) are significantly different, with the p-value of $\simeq 10^{-6}$ from the two-dimensional Kolmogorov-Smirnov test (Fasano & Franceschini, 1987; Press *et al.*, 1992). Although dataset L or H could be affected by a background fluctuation or short time-scale outbursts of nearby sources (on a time scale of days,

longer outbursts should give similar contribution to both L and H), it is highly unlikely that such a fluctuation/outburst affects also all these shorter data sets in a manner illustrated in Figure 5.5.

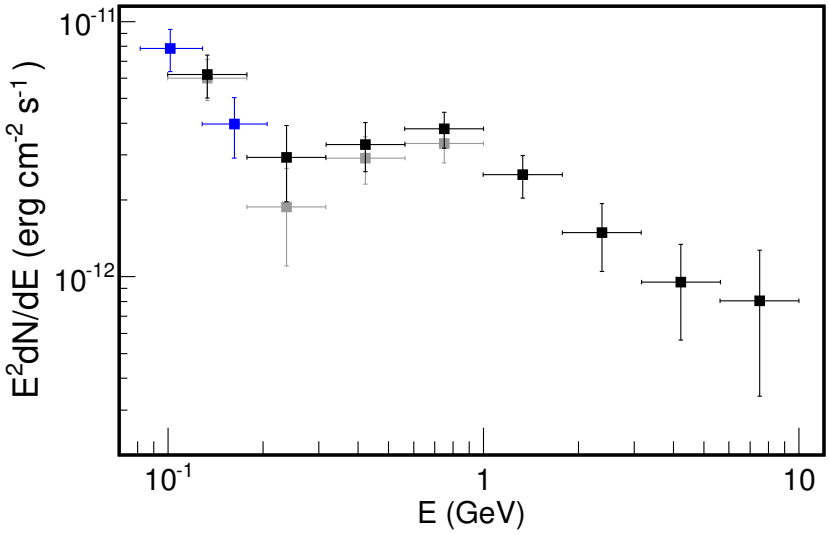

Figure 5.6: SED for dataset L. The black and blue points are for the best-fit model; the gray points below 1 GeV are obtained with model T (see Chapter 5.2.2).

Finally, I note hints for departures from a simple power-law shape of the γ-ray spectrum for dataset L. Figure 5.6 shows the SED with energy bins twice smaller than in Figure 5.2, indicating the break at $\sim$ 800 MeV, and an additional very soft component below $\sim$ 200 MeV. Testing the reality of the latter, I used two bins in the 80–200 MeV range, which consistently indicate an excess increasing toward low energies (the blue points in Figure 5.6). Power-law fits for dataset L give $\Gamma \simeq 1.9 \pm 0.2$ in the 0.2–1 GeV and $\Gamma \simeq 2.7 \pm 0.2$ in the 1–100 GeV range. Interestingly, the spectral break at $\sim$ 800 MeV seen in Figure 5.6 is characteristic for pion-decay emission. However, I found only $TS_{curve} \simeq 10$ for this departure from a power-law, where TS_{curve} is defined as in 3FGL, i.e. using the difference of the likelihoods for a simple power-law and double-broken power-law fits. Then, the significance of these spectral features is rather low. For dataset H I did not find signatures of departure from the simple power-law spectrum.

5.4 Discussion

Apart from NGC 4945, two other Seyfert 2 galaxies, NGC 1068 and Circinus, have been detected by LAT (Hayashida *et al.*, 2013; Lenain *et al.*, 2010). Similar to NGC 4945, these galaxies exhibit a composite starburst/AGN activity and the interpretation of their γ-ray emission is uncertain. Among the three γ-ray loud Seyfert 2s, the X/γ-ray correlation can be investigated only in NGC 4945, which has the largest γ-ray detection significance, and whose variable X-ray emission from the nucleus can be directly observed. In contrast, the X-ray radiation from NGC 1068 is fully reflection dominated and no variability is observed. Circinus, in turn, is strongly contaminated by the Galactic plane and its detection significance is too low to search for changes of the γ-ray spectrum.

The correlation revealed in my study implies that the γ-ray production in NGC 4945 is dom-

inated by the active nucleus. On the other hand, at the supernova rate estimated for NGC 4945 (Lenc & Tingay, 2009), the injected cosmic ray power is sufficient to produce the observed L_γ through π^0-decay emission (cf. Lenain *et al.*, 2010; Eichmann & Becker Tjus, 2016). Below I briefly discuss this issue in the context of γ-ray observations of other Seyfert and starburst galaxies.

The GeV and TeV detections of two nearby starburst galaxies, M82 and NGC 253 (Acero *et al.*, 2009; VERITAS Collaboration *et al.*, 2009; Abdo *et al.*, 2010a), have confirmed the link between the star-formation activity and the γ-ray emission likely related to pionic interactions of cosmic rays with the interstellar medium; a universal scaling of L_γ with the star-formation rate was then proposed in Ackermann *et al.* (2012a). However, an efficient γ-ray emission in this class of objects appears to be not as ubiquitous as could be expected after these first detections (cf. Rojas-Bravo & Araya, 2016) indicating that non-radiative losses (i.e. diffusive or advective escape) dominate in some starbursts.

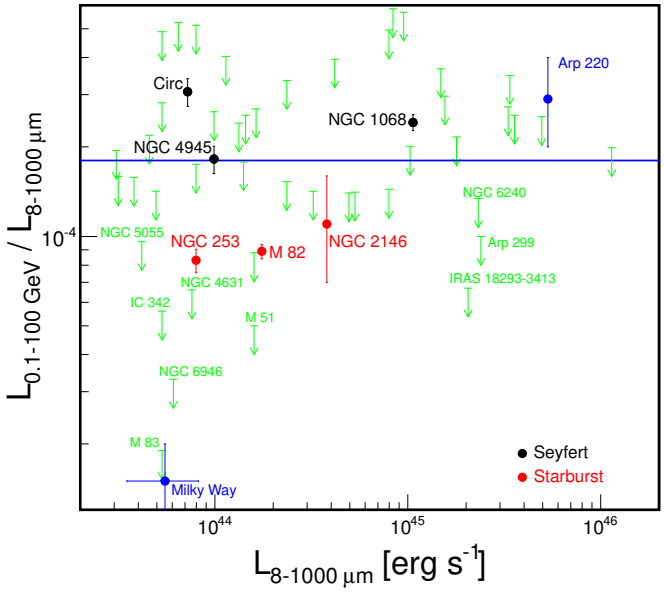

Figure 5.7: Comparison of the γ-ray (0.1–100 GeV) and IR (8–1000 μm) luminosities for star-forming and Seyfert galaxies. I adopted data from Tang *et al.* (2014) for NGC 2146, Griffin *et al.* (2016) for Arp 220, Ackermann *et al.* (2012a) for IR luminosities and Milky Way γ-ray luminosity, upper limits (green arrows) from Rojas-Bravo & Araya (2016) for non-detected galaxies and I used my results for NGC 4945 (dataset T), NGC 1068, Circ, M 82 and NGC 253 (Table 5.1). The blue line shows the calorimetric limit.

Figure 5.7 compares the γ-ray luminosity of star-forming galaxies with their IR luminosity, which is a good tracer of the star-formation rate (e.g. Kennicutt, 1998) and, hence, estimates the injected cosmic ray power. The blue line corresponds to the calorimetric limit, in which the total energy of cosmic rays is used for the pion production and assuming that each supernova injects 10^{50} ergs of cosmic ray energy (e.g., Ackermann *et al.*, 2012a). The γ-ray luminosities of starburst galaxies, M 82 and NGC 253, a factor of ~ 2 below this limit, indicate that $\sim 50\%$ of cosmic ray energy is channeled for pion production, as also found in the starburst models for these objects (e.g., Lacki *et al.*, 2011; Yoast-Hull *et al.*, 2014). These starbursts have harder γ-ray spectra than the Seyfert galaxies, so the (energy-dependent) diffusive losses would be more important in the

starburst scenario for the latter. Yet, Seyferts are at or above the calorimetric limit, which presents a major problem for the starburst model (cf. Hayashida *et al.*, 2013) and points toward a significant contribution from their AGN components. Studies of γ-ray emission from NGC 1068 (e.g., Lenain *et al.*, 2010; Yoast-Hull *et al.*, 2014; Eichmann & Becker Tjus, 2016) indeed find that it cannot be explained by the starburst activity and indicate the active nucleus as the primary source of γ-rays.

A constant in time contribution of the starburst component in NGC 4945, which obviously cannot exceed the level of γ-ray emission found in X-ray resolved data sets, can still significantly contribute to the total L_γ. For parameters similar to those of M 82 (the dashed line in Figure 5.2b) such a diffuse emission would only slightly over predict the flux above 10 GeV in dataset L. Then, with a small reduction of the γ-ray production efficiency, it could fully account for emission above 10 GeV measured for low X-ray flux levels and give a $\sim$ 20% contribution to the total L_γ. For much lower efficiencies of γ-ray production, e.g. such as assessed for M 83, which has a high surface density (but lower than NGC 4945; cf. Lacki *et al.*, 2011), contribution from the starburst component would be insignificant.

The Seyfert galaxies exhibit also an interesting similarity of their Eddington-scaled X-ray and γ-ray luminosities, as discussed in the previous Chapter, with $L_\gamma/L_{\rm Edd} \simeq 10^{-4}$ (0.1–100 GeV) and $\lambda_{\rm X} \equiv L_{\rm X}/L_{\rm Edd} \simeq 0.02$ (2–10 keV) in all three objects. These are the largest values of $\lambda_{\rm X}$ observed in nearby AGNs. At such $\lambda_{\rm X}$ transition between the hard and soft spectral state is observed in black-hole binaries; softening of the X-ray spectrum with increasing luminosity observed in NGC 4945 (Puccetti *et al.*, 2014; Caballero-Garcia *et al.*, 2012), see Figure 4.1 resembles the behavior of black-hole transients during this spectral state change.

A prominent γ-ray signal has not been detected from other radio-quiet Seyfert galaxies (Ackermann *et al.*, 2012b). However, in the context of high-energy emission from accretion flows, the available LAT upper limits provide only a moderate constraint of $\lesssim$ 10% on the fraction of accretion power which can be used for acceleration of protons and/or electrons emitting in the GeV range, as found in the previous Chapter. Presence of such nonthermal particles in accretion flows can be expected both from a theoretical point of view (e.g., Kimura *et al.*, 2016) and from modeling of some observed spectra (e.g., Poutanen & Veledina, 2014), but any γ-ray radiation produced within accretion flow, or in its vicinity, would be strongly attenuated by $\gamma\gamma$ interactions with the ambient radiation field.

I used the model of internal $\gamma\gamma$ absorption, described in previous Chapters, to assess possible locations of the γ-ray emitting site in the NGC 4945 active nucleus. Geometry of the inner accretion flow and the nature of the X-ray source are highly uncertain for NGC 4945 due to the obscuration of its nucleus. I considered the case of an optically thick disc extending down close to the black hole, motivated by the commonly accepted model of black-hole binaries relating transition to the soft spectral state, at $L \sim 0.1 L_{\rm Edd}$, with rebuilding of such a disc, as described in Chapter 1.

Due to paucity of photons with $E > 10$ GeV I was not able to rule out or confirm a presence of a spectral break at these energies. Using `gtsrcprob` I found that the largest photon energy detected from NGC 4945 with high probability ($> 80\%$) is $E \simeq 40$ GeV. Below I assume that the γ-ray spectrum of the high X-ray flux levels does not possess a high-energy cut-off up to at least a few tens of GeV. This requires the source to be at least $\sim (10^3 - 10^4) R_{\rm g}$ away from the

inner accretion disc, depending on inclination, where $R_g = GM/c^2$ is the gravitational radius; the distance may be lower than $10^3 R_g$ if we observe the accretion disc from a face-on direction, which is unlikely for a Seyfert 2 galaxy. I assumed that the γ-ray source is located at the symmetry axis, and I used the standard disc model of Shakura & Sunyaev (1973). To assess the maximum effect of γ-ray attenuation in thermal-radiation field of such a disc, I assumed that it accretes with the rate $\dot{M} = L_{Edd}/c^2$, and extends down to the innermost stable circular orbit (ISCO) at $6R_g$. I took into account a compact, centrally located X-ray source matching the internal X-ray luminosity and spectral index reported in Puccetti *et al.* (2014); the exact geometry of this source is not important for opacity to γ-rays emitted far from it. Due to anisotropy of the radiation field, the cut-off energy related with $\gamma\gamma$ absorption depends on the viewing angle, see e.g. Cerutti *et al.* (2011), but note that the inner disc of the binary system considered in that work emits in soft X-rays whereas that in NGC 4945 nucleus would emit in UV, so quantitative results are different.

On the other hand, by the causality argument, the γ-ray source located more than ~ 1 light day away from the X-ray source would not be able to respond to its changes in the manner indicated by my results. Again assuming that the X-rays are produced by a compact source close to the black hole, this constrains the distance of the γ-ray source to $\lesssim 10^4 R_g$. This, in turn, rules out edge-on observing directions, with inclination angles $\gtrsim 70^\circ$, for which a larger distance is required by the γ-ray transparency condition. I note also that a detection of NGC 4945 above 100 GeV, with a power-law spectrum extending from the LAT range, would contradict my findings, as photons with such energies cannot escape from the region within 1 light day. In this context it is interesting to note that NGC 4945 (as well as the other two Seyferts) has not been detected in this range so far, although a detection is within reach of currently operating imaging atmospheric Cherenkov telescopes.

A γ-ray source located $\sim (10^3 - 10^4) R_g$ from the central engine would be possibly related with formation of a weak jet. A jet-like structure is indeed observed in NGC 4945 nucleus, and also in NGC 1068 and Circinus, but such nuclear jets are commonly found in other Seyfert galaxies as well (e.g. Gallimore *et al.*, 2006; Elmouttie *et al.*, 1998; Lenc & Tingay, 2009). The specific conditions underlying the γ-ray loudness of NGC 4945, NGC 1068 and Circinus may then involve their high L/L_{Edd} values and the related changes in accretion flow. In particular, it may involve a rapid increase of the jet velocity occurring when an inwards-moving inner disc edge in a source making a hard to soft state transition approaches the ISCO, which is the preferred interpretation of the disc-jet coupling, well-established in black-hole X-ray binary systems (e.g. Fender *et al.*, 2004) and observed also in AGNs (e.g. Marscher *et al.*, 2002). Particles would then be accelerated by an internal shock formed in the collision of a fast jet with a previously existing slower outflow. Notably, Cerutti *et al.* (2011) estimate a similar distance (in units of R_g) of the γ-ray source for Cyg X-3, where the γ-ray emission is related with hard/soft state transitions (e.g. Corbel *et al.*, 2012) occurring at L/L_{Edd} similar to that of NGC 4945. The origin of γ-ray emission in the active nucleus was favored for NGC 1068 by Lenain *et al.* (2010) and Lamastra *et al.* (2016). Both these works argue that the γ-rays are most likely related with an AGN outflow. However the γ-ray emission sites in the specific scenarios proposed in these studies are located at a much larger distance, i.e. ~ 100 pc, than estimated in my analysis of NGC 4945; for the mass of $10^7 M_\odot$, measured in NGC 1068, $10^4 R_g$ corresponds to 0.01 pc.

The γ-ray spectrum of the low X-ray flux levels can be observed from a source located at a smaller distance, $\sim 10^2 R_{\rm g}$; more precise estimates depend on the assumed geometry. E.g., the γ-rays may come from an inner optically-thin flow, located within a few tens of $R_{\rm g}$, if the starburst activity of this galaxy accounts for the emission above $\sim$ 10 GeV (see above). I note that similar signals, pronounced only below $\sim$ 1 GeV, cannot be excluded in other Seyfert galaxies, as presence of nearby sources often does not allow for a proper assessment of a signal at such energies. Such a signal indeed may be present in the brightest in hard X-rays Seyfert galaxy NGC 4151, as discussed in the previous Chapter.

Chapter 6

10 years of *AGILE* observations of Cygnus X-1

In this chapter I describe my search of a γ-ray signal in *AGILE* data from the direction of Cyg X-1. Between July 2007 and October 2009 *AGILE* operated in the pointing mode and it performed several pointing observations of Cyg X-1. Since November 4 2009 *AGILE* has been operating in a spinning mode, yielding a continuous increase of the accumulated dataset.

There have been several studies of Cyg X-1 data based on the first few years of *AGILE* observations. Steady γ-ray emission has been investigated in (Sabatini *et al.*, 2010; Del Monte *et al.*, 2010; Chen *et al.*, 2011; Piano *et al.*, 2012; Sabatini *et al.*, 2013). They found no significant persistent signal. However, three γ-ray flares above 100 MeV on a timescale of a few days were found, as discussed in Section 6.2.2.

Sabatini *et al.* (2013) considered observations performed until 2012 and no later analyses can be found in literature. Motivated by the recent detection of γ-rays from Cyg X-1 in LAT data, I investigated the data from observations performed by *AGILE* over the time almost $\simeq$ 3.5 times longer than in data used in previous studies, with about twice larger exposure time (details of this estimation are explained in Chapter 6.3).

6.1 Cygnus X-1

Cyg X-1 is an archetypal (as described in Chapter 1), persistent black-hole binary, powered by accretion from the OB supergiant HDE 226868. The binary is located at a distance of 1.86 ± 0.12 kpc from the Earth (Reid *et al.*, 2011), has a 5.6-day period and an inclination angle of the orbital plane to our line of sight of $(27.1 \pm 0.8)^\circ$ (Orosz *et al.*, 2011). The plausible mass ranges are 21–35 $M_\odot$ for the donor star and 10–23 $M_\odot$ for the black hole, with the most likely values of 27 $M_\odot$ and 16 $M_\odot$, respectively (Ziółkowski, 2014). Cyg X-1 is the only high-mass X-ray binary in our Galaxy with the compact object identified as a black hole. Being persistent and one of the brightest X-ray sources, Cyg X-1 is an excellent object to study accretion processes.

As outlined in Chapter 1, Cyg X-1 displays the two main spectral states, hard and soft, which are observed also in black-hole transients. In Cyg X-1, however, changes of the observed luminosity between the two states are small, by a factor of ~ 3. The isotropic bolometric luminosity is estimated to $L_{\rm hard} \simeq 2\times10^{37}$ erg/s for the hard state and $L_{\rm soft} \simeq (6-7)\times10^{37}$ erg/s for the soft state

(e.g. Gierlinski *et al.*, 1997; Gierliński *et al.*, 1999; Frontera *et al.*, 2001; Zdziarski *et al.*, 2002). The corresponding Eddington ratios are estimated to $\lambda_{\rm hard} \simeq 0.01$ and $\lambda_{\rm soft} \simeq 0.03$.

Cyg X-1 is a variable radio source. In the hard state, the radio emission is produced by synchrotron emission in a jet, which has been resolved at the milliarcsec scale and extends ~ 15 mas from the source (Stirling *et al.*, 2001). In the soft state, the radio emission is suppressed, indicating that the radio jet is not produced. A similar radio suppression in the soft state is observed in other black hole binaries (e.g. Fender *et al.*, 2004). Cyg X-1, however, does not show the radio flaring (probably related with ejections of radio-emitting blobs) which is seen in other black-hole systems. The jet likely inflates a shell-like structure aligned with it (Gallo *et al.*, 2005), with a ~ 5 pc diameter. The total kinetic power of the jet estimated from measurements of the jet-powered nebulae is $(0.9 - 3) \times 10^{37}$ erg/s (Russell *et al.*, 2007), which is comparable to $L_{\rm hard}$.

6.2 γ-ray observations

6.2.1 Persistent emission

γ-ray emission from Cyg X-1 was first observed in the soft-state by *CGRO*/COMPTEL, which measured the high-energy tail with a photon index of $\Gamma \simeq 2.5$ extending up to ~ 10 MeV (McConnell *et al.*, 2002). The energy up to which the soft-state tail extends was unknown. The upper limit for the soft state from *AGILE*, reported by Sabatini *et al.* (2013), ruled out extension of this tail above 100 MeV.

A $\sim 4\sigma$ hint of γ-ray signal from Cyg X-1 above 100 MeV was found by Malyshev *et al.* (2013) in 3.8 yr of *Fermi*/LAT data. The signal appeared only when the source was in the hard state. A significant, 8σ-level, evidence for a persistent γ-ray emission was later confirmed by Zanin *et al.* (2016) and Zdziarski *et al.* (2017), who used 7.5 yr of *Fermi*/LAT data; again, the signal above 100 MeV was found only for the hard state. They also found hints of γ-ray orbital modulation, which rules out production of γ-rays in interaction between the jet and the surrounding medium at large scales, and which could indicate that the γ-rays are produced in the jet through (anisotropic) inverse Compton scattering of stellar blackbody photons. However, Zdziarski *et al.* (2017) found that the observed modulation is significantly weaker than that predicted if this was the dominant source of γ-rays and favor production of γ-rays by the synchrotron-self-Compton process. Zdziarski *et al.* (2017) also claim a detection of Cyg X-1 in both the soft and hard state in the 40-80 MeV range, which emission is interpreted as the high-energy tails of the emission of the accretion flow; in both states the spectra are very steep and may correspond to the high-energy cutoffs of the tails due to photon-photon absorption.

Although the 8 year LAT catalog has not been officially published yet, the FL8Y source list (see Chapter 2.3.5) reports parameters of sources present in the region relevant for the analysis of Cyg X-1 which consistent with those found by Zanin *et al.* (2016) and Zdziarski *et al.* (2017). Then, I use them in my analysis. In particular, FL8Y includes the source FL8Y J1958.5+3512, with $\sigma = 8.1$ and $\Gamma = 2.29 \pm 0.12$, found at the position of Cyg X-1 in the total 8-years dataset (i.e. without the spectral state criterion).

Searches for steady signals at very high energies (above ~ 100 GeV), reported for 40 hr of

observations in 2006 with the first stand-alone MAGIC telescope by Albert *et al.* (2007) and for 97 hr of observations between 2007 and 2014 in the MAGIC stereo mode by Ahnen *et al.* (2017), yielded no positive results. However, the published upper limits are rather weakly constraining and do not exclude extension of the power-law component measured by LAT into this energy range.

6.2.2 Flares

Strong hard X-ray flares are observed in Cyg X-1 on timescales of days and hours in both the soft and the hard states (Cui *et al.*, 2002; Golenetskii *et al.*, 2003; Stern *et al.*, 2001). There have been several claims of flaring γ-ray activity of Cyg X-1. Albert *et al.* (2007) reported a $\sim 4\sigma$ evidence for an 80-minutes flare seen by MAGIC on September 24, 2006 from the Cyg X-1 direction. The flare took place close to the superior conjunction (with the black hole behind the massive star), when the opacity to photon-photon absorption in the stellar photon field is the highest. This makes a detection of TeV photons produced in the jet within the binary system very unlikely, and favors the emission originating far from the compact object, e.g. due to interactions of the jet with the the surrounding medium. Then, mechanism producing the TeV photons would have to be different from that producing GeV photons detected by LAT.

Three cases of transient emission were reported for *AGILE* observations, each lasting $\sim$ 1 day. In each case the reported photon flux above 100 MeV was about two orders of magnitude larger than *AGILE* upper limits for steady emission. The first two events occurred in the hard state on October 16, 2009 (Sabatini *et al.*, 2010) and on March 24, 2010 (Bulgarelli *et al.*, 2010). The third one took place during the transition from the hard to soft state on June 30, 2010 (Sabatini *et al.*, 2013).

About 20 flares with TS > 9 where also found in the LAT data by Bodaghee *et al.* (2013). Their distribution is consistent with that of random fluctuations so these detections could be spurious. However, three of them took place one or two days before the flares reported by *AGILE*; then Bodaghee *et al.* (2013) note that these three flares represent real detections.

6.3 Data analysis

I analyzed Cyg X-1 observations including all the available data gathered between the beginning of *AGILE* operation in July 2007 and September 2017. I took into account three datasets: (1) the total dataset including all available data, (2) the dataset including data collected during the hard state and (3) the dataset including data collected during the soft state. I used the criterion for distinguishing the soft state from the hard state defined by Grinberg *et al.* (2013), indicating the source to be in the soft (hard) state when the publicly available *Swift*/BAT daily count rate[1] is lower (higher) than 0.09 counts/cm^2/s. The resulting time intervals for the soft and hard state are given in Table 6.1. My analysis extends previous studies of GRID data by including observations performed after mid-2012. As seen in Figure 6.1, Cyg X-1 spent roughly equal amount of time in the soft and hard states during this additional time.

Sensitivity of GRID observations depends on the off-axis angle (i.e. the angle between the source position and the field-of-view center); see e.g. Tavani *et al.* (2009b) for the dependence

[1] `https://swift.gsfc.nasa.gov/results/transients/CygX-1/`

of the effective area on the off-axis angle. Due to the *AGILE* pointing strategy, the off-axis angle of Cyg X-1 during the pointing observations ranges between 2.4° and 33°, (see (Del Monte *et al.*, 2010)). During the spinning observations, the Cygnus region is most of the time in the field-of-view of GRID, however, the sensitivity is reduced (due to larger, on-average, off-axis angle) compared to the pointing observations, see Bulgarelli *et al.* (2012).

The effective exposure (taking into account off-axis angles, occultation by the Earth etc.) in observations mixing the pointing and spinning modes can be compared using the output of the *AG_multi4* tool of the *AGILE* analysis software (see below), which gives the product of the exposure time and the effective area averaged over the energy range (for an assumed shape of γ-ray spectrum). Using this information I found that the effective exposure for data used in my analysis is larger by a factor of $\simeq$ 1.8 for the hard state, compared to previous studies by Sabatini *et al.* (2010) and Del Monte *et al.* (2010), and by a factor of $\simeq$ 2.5 for the soft state compared to the previous study by Sabatini *et al.* (2013). Observations in the hard state contribute about 75% and those in the soft state about 25% to such estimated effective exposure of the total dataset.

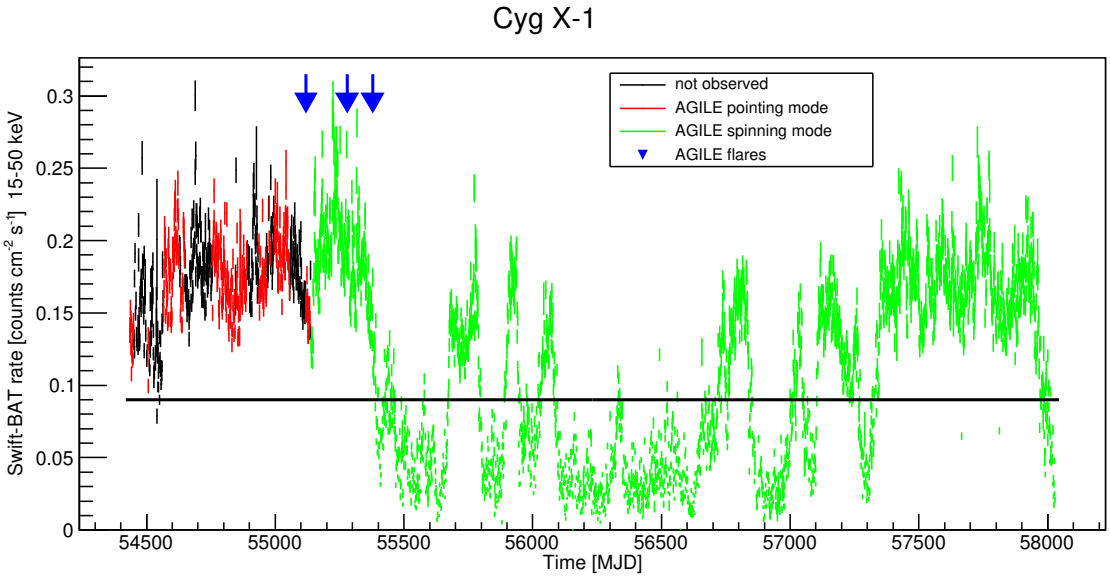

Figure 6.1: *Swift*/BAT lightcurve of Cyg X-1 during the *AGILE* observations; the daily count rate was taken from the BAT webpage (see text). *AGILE* observations in pointing and spinning mode are indicated by the red and green color, respectively. The three flare events observed by *AGILE* are indicated by the blue arrows. The black horizontal line represents the level used to distinguish the hard (above the line) and soft (below the line) spectral states due to the counts criterion described in Grinberg *et al.* (2013).

In the analysis I used the latest available version, `AGILE_SW_5.0`, of *AGILE* multi source analysis software[2]. GRID data are released with 2 available filters: FT3AB and FM (Chen *et al.*, 2013). Both filters have been used in published analysis results, e.g. Sabatini *et al.* (2010) apply the former, while Sabatini *et al.* (2013) apply the latter filter[3]. Both filters take into account the South Atlantic Anomaly event cuts as well as 90° Earth albedo filtering. The *AGILE* Team

[2]http://agile.asdc.asi.it/publicsoftware.html

[3]Early publications, e.g. the first *AGILE*/GRID catalog (1AGL) Pittori *et al.* (2009), used another filter, F4.

Hard state	Soft state
54435–55375	55391–55672
55672–55790	55797–55889
55889–55945	55945–56020
56020–56086	56086–56330
56718–56753	56338–56718
56759–56839	56839–57009
57009–57053	57053–57103
57103–57265	57265–57325
57325–57980	57980-58028

Table 6.1: MJD intervals for hard and soft states.

recommends the use of the FM filter[4], which applies a more advanced background events selection, for a standard likelihood analysis. However, the FT3AB filter, which is more permissive and keeps a larger set of events, is considered to be more effective in detecting sources with soft spectra (which may be the case for Cyg X-1, given its LAT index of $\simeq 2.4$). I used both filters in my analysis. In some cases they gave different results, so below I present results obtained with both. In both versions of the analysis I used only events confirmed as γ-rays[5]. Count maps and exposure maps were built for the $30^\circ \times 30^\circ$ area, centered on the position of Cyg X-1 (Galactic coordinates $l = 71.335^\circ$ and $b = 3.067^\circ$), with the bin size of 0.3°. For each filter the corresponding calibration and diffuse model files were used.

The analysis software gives the photon flux for model components fitted with $\sqrt{\mathrm{TS}} > 2$ and 95% ULs for lower detection significance values. I follow this convention and in the next Section I present the fitted flux for all cases with $\sqrt{\mathrm{TS}} > 2$.

Models used in my analysis to fit the GRID data take into account γ-ray sources located within the radius of 10° around Cyg X-1. I considered two basic models of this region. The first one, referred to as model G, includes only sources detected by GRID. This allows to compare my results with previous studies of the *AGILE* observations. The second model, referred to as model L, takes into account additional sources detected by LAT. This allows to investigate contamination by all nearby γ-ray sources.

Sources included in the models are shown in Table 6.2 and in the map in Figure 6.2. Note that unlike TS maps for LAT observations, presented in Sections 4 and 5, the intensity maps produced by the *AGILE* software do not subtract contribution from the background. Therefore, only strong sources are visible on these maps.

Model G includes 5 sources, S1–S5, from the updated *AGILE*/GRID catalog[6] (1AGLR) of bright γ-ray sources Verrecchia *et al.* (2013). I included also 2 sources, detected after the publication of this catalog, S6 and S7, which are added into the model by the automatic `LV9 AGILE` online pipeline tool[7], but they appear unimportant for the results. On the other hand, I neglected in model G source S15, which has been detected in the GRID data in the study of Cygnus region by Bulgarelli *et al.* (2012) (however, it is not reported in 1AGLR), but it has not been included in

[4] `http://www.asdc.asi.it/doc/AGILE_data_release_note_v14.0.pdf`
[5] by setting `filtercode=5` in `AG_ctsmapgen`
[6] `http://www.asdc.asi.it/agile1rcat`
[7] `http://www.asdc.asi.it/mmia/index.php?mission=agilelv3mmia`

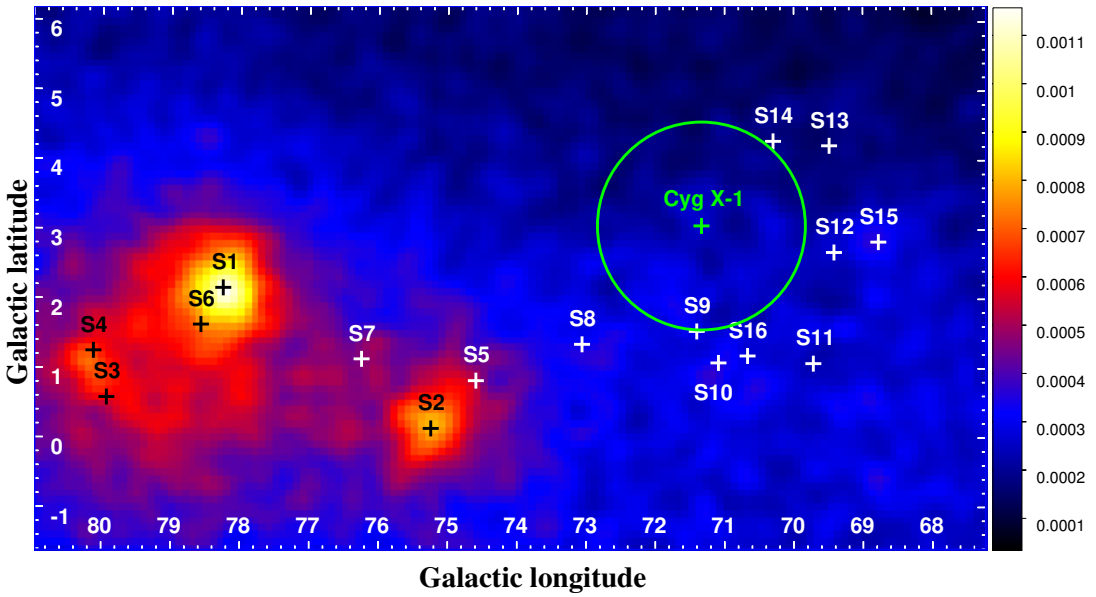

Figure 6.2: Intensity map of Cygnus X-1 for the total dataset with sources used in models G and L, computed for the pixel size of 0.1° using filter FM, displayed with 3-bin Gaussian smoothing. 1AGLR sources are marked in black, FL8Y sources are marked in cyan, see Table 6.2. The scale is in the units of counts cm^{-2} s^{-1} sr^{-1}. The circle around Cyg X-1 has the radius of 1.5°, which corresponds to *AGILE*/GRID 68% point spread function at ~300 MeV, Sabatini *et al.* (2015).

previous studies of Cyg X-1. This is a relatively bright source located about 2.5° from Cyg X-1, and its inclusion in the model could affect the comparison with previous studies of the *AGILE* observations. The remaining *AGILE* sources are concentrated in the region clearly visible in the left bottom corner in Figure 6.2 and their distance from Cyg X-1 exceeds 4 degrees, so they should not contaminate strongly the signal. Following the procedure used in 1AGLR (and the previous 1AGL catalog Pittori *et al.*, 2009), I fixed the spectral indexes of all model G sources to 2.1, except for the three brightest sources, S1–S3, for which spectral indexes were adopted from FL8Y, see Table 6.2.

Model L includes additionally all known γ-ray sources located within the radius of 3° around Cyg X-1. FL8Y[8] reports 9 sources in this area (apart from FL8Y J1958.5+3512, which is the γ-ray counterpart of Cyg X-1). Sources S15 and S16 were reported already in 3FGL (3FGL J1952.9+3253 and 3FGL J2004.4+3338). Sources S8, S9, S12, S13 and S14 were detected in Zanin *et al.* (2016) and Zdziarski *et al.* (2017) and they were included in previous analysis of LAT data of Cyg X-1. S10 and S11 are new sources.

All bright γ-ray sources located close to Cyg X-1 are young pulsars, some associated with supernova remnants resolved by LAT, which are not expected to be variable. The most prominent flaring source is S3 (i.e. Cyg X-3) located $\simeq$ 9° from Cyg X-1.

[8] https://fermi.gsfc.nasa.gov/ssc/data/access/lat/fl8y/

Model name	Catalog name	Γ	G	L	Counterpart name
AGILE Sources from 1AGLR					
S1	1AGLRJ2021+4030	2.41	✓	✓	PSR J2021+4026
S2	1AGLRJ2021+3653	2.37	✓	✓	PSR J2021+3651
S3	1AGLRJ2033+4057	2.61	✓	✓	Cyg X-3
S4	1AGLRJ2031+4130	2.1	✓	✓	
S5	1AGLRJ2016+3644	2.1	✓	✓	
S6	AGLJ2024+4027	2.1	✓	✓	
S7	AGLJ2019+3816	2.1	✓	✓	
LAT sources from FL8Y					
S8	FL8Y J2009.9+3544	2.20		✓	
S9	FL8Y J2004.8+3427	2.67		✓	
S10	FL8Y J2005.8+3356	2.07		✓	
S11	FL8Y J2002.4+3247	2.44		✓	
S12	FL8Y J1955.1+3322	2.47		✓	
S13	FL8Y J1948.9+3412	2.38		✓	
S14	FL8Y J1950.6+3456	1.85		✓	
S15	FL8Y J1952.9+3252	2.30		✓	PSR J1952+3252
S16	FL8Y J2004.3+3339	2.34		✓	

Table 6.2: List of sources used for modeling the area around Cyg X-1, including the *AGILE*-detected sources and FL8Y sources located closer than 3° from Cyg X-1. The third column shows the value of Γ fixed for the source in the analysis. Columns G and L indicate, whether the source is included in the corresponding model.

Table 6.3 shows the fitting results for sources with significant detections in my analysis of the total dataset, and compares them with GRID and LAT catalog parameters. The remaining sources were typically fitted with TS $\lesssim 1$. Among these sources not revealed in the GRID data, only S16 is reported in FL8Y with both the photon flux and detection significance larger than those of Cyg X-1 (and with a similar spectral index). This source is located at $b \simeq 1°$, hence it is affected by a stronger contamination by the Galactic background. Interestingly, although it is not detected in fitting the total dataset, the intensity maps for the soft-state dataset in Figures 6.4 (dominated by low energy photons) and 6.5 show a signal at its position. The remaining LAT sources which were non-detected in my analysis are weaker than Cyg X-1, with only marginal detection significances ($\lesssim 6\sigma$) reported in FL8Y.

γ-ray source	$\sqrt{\text{TS}}$	F_γ	$\sqrt{\text{TS}}$	F_γ	$\sqrt{\text{TS}}$	F_γ
	my analysis		1AGLR		FL8Y	
S1	53.9	17.2 ± 0.4	15.3	15.8 ± 1.3	123	51.1 ± 0.8
S2	33.7	9.4 ± 0.3	8.5	6.5 ± 0.9	175.6	33.4 ± 0.5
S3	13.6	3.3 ± 0.3	5.5	7.9 ± 1.7	6.9	1.6 ± 0.3
S15	9.4	1.7 ± 0.2	–	–	109.3	9.3 ± 0.2

Table 6.3: The detection significance and the measured photon flux for strong γ-ray sources from my analysis with filter FM of the total dataset in the energy range 0.1–50 GeV, compared with the results from 1AGLR and FL8Y. F_γ is the photon flux above 100 MeV in the unit of 10^{-7} ph/cm^2/s.

Filter	Γ	$\sqrt{TS}$	UL or F_γ model G	$\sqrt{TS}$	UL or F_γ model L
hard state					
FM	2.1	1.1	< 5.5	0	< 2.8
FM	2.4	1	< 7.3	0	< 3
FT3AB	2.1	0	< 3.1	0	< 1.7
FT3AB	2.4	0	< 4.3	0	< 2.5
soft state					
FM	2.1	2.5	7.6 ± 3.2	1.4	< 11.1
FM	2.4	5.1	21.8 ± 4.6	1.8	< 17.7
FT3AB	2.1	2.4	8.9 ± 3.9	0.8	< 11.2
FT3AB	2.4	4.3	21.7 ± 5.1	3	19.0 ± 6.4
total					
FM	2.1	1.5	< 5.3		
FM	2.4	1	< 6.1		
FT3AB	2.1	0.3	< 4		
FT3AB	2.4	0	< 5.8		

Table 6.4: The detection significance and either the photon flux, F_γ (for $\sqrt{TS} > 2$), or 95% confidence level UL on F_γ (for $\sqrt{TS} < 2$) in 0.1–50 GeV energy range, for the hard and soft state and the total GRID dataset for Cyg X-1, analyzed using two GRID filters, two values of Γ fixed for Cyg X-1 and two models of the region. F_γ/UL is given in the unit of 10^{-8} ph/cm^2/s.

For the strong γ-ray pulsars, S1, S2 and S15, we see in Table 6.3 a large increase of the statistical significance of GRID detections corresponding to the increase of the exposure time compared to 1AGLR, which was constructed using only the pointing observations. S3 is a flaring source, which likely affects the comparison with previous results.

6.4 Results

Tables 6.4 and 6.5 show results of my analysis of the three GRID datasets for Cyg X-1 with both filters, FT3AB and FM, and for two values of spectral index, $\Gamma = 2.1$ and 2.4; the former was used in previous works on *AGILE* observations, the latter is close to the value measured by LAT in the hard state.

Neither of the fitting results for the hard state shows any significant signal and the results are consistent with previous studies, e.g. the UL for the hard state with model G, filter FT3AB and $\Gamma = 2.1$ in Table 6.5 is the same as found in Sabatini *et al.* (2010) for the same energy range and using the same filter, Γ and model components. We can also see that including additional γ-ray sources, known to be present close to Cyg X-1, in model L, allows to reduce the UL by a factor of ~ 2 as compared to the values obtained with model G. Then, I use model L to compare GRID upper limits with the LAT SED, adopted from Zdziarski *et al.* (2017), see Figure 6.3. We can see that, below 1 GeV, the GRID upper limits for the hard state are by a factor of ~ 2 larger than the flux measured by LAT. I conclude that *AGILE* is approaching the sensitivity needed for detection of Cyg X-1 in the 0.1–1 GeV range and it could possibly be done with a few more years of observations in the hard state.

Filter	Γ	$\sqrt{TS}$	UL or F_γ model G	$\sqrt{TS}$	UL or F_γ model L
hard state					
FM	2.1	1.3	< 5.7	0	< 2.5
FM	2.4	1	< 7.1	0	< 2.7
FT3AB	2.1	0	< 3.5	0	< 2.3
FT3AB	2.4	0	< 5.2	0	< 3.2
soft state					
FM	2.1	2.1	6.5 ± 3.2	0.7	< 8.7
FM	2.4	2.2	9.2 ± 4.3	0.4	< 10.8
FT3AB	2.1	2.2	7.9 ± 3.8	0	< 8.2
FT3AB	2.4	2.4	12.6 ± 5	0	< 11.5

Table 6.5: Similar to Table 6.4 but in 0.1–3 GeV energy range. This range was used in some previous works, e.g. Sabatini *et al.* (2010). Results for the total dataset are the same as shown in Table 6.4.

As noted above, the total dataset is dominated by observations performed in the hard state, therefore, the fitting results as well as the intensity maps for these two datasets are similar.

Surprisingly, a weak γ-ray signal is revealed in the soft state in some variants of the analysis. However, these results are model-dependent, in a manner pointing to the influence of neighboring sources. Fitting of model G with $\Gamma = 2.4$ set for Cyg X-1 indicates a marginal detection with $\sqrt{TS} > 4$ for both filters. Model L, however, reduces the significance of Cyg X-1 detection to $\sqrt{TS} < 2$, except for filter FT3AB and $\Gamma = 2.4$ in the 0.1–50 GeV range, where it is still $\simeq 3$. I found that the reduction of the signal from Cyg X-1 is most likely due to a proper inclusion of S15, which is fitted in model L with parameters similar to those fitted for the total dataset.

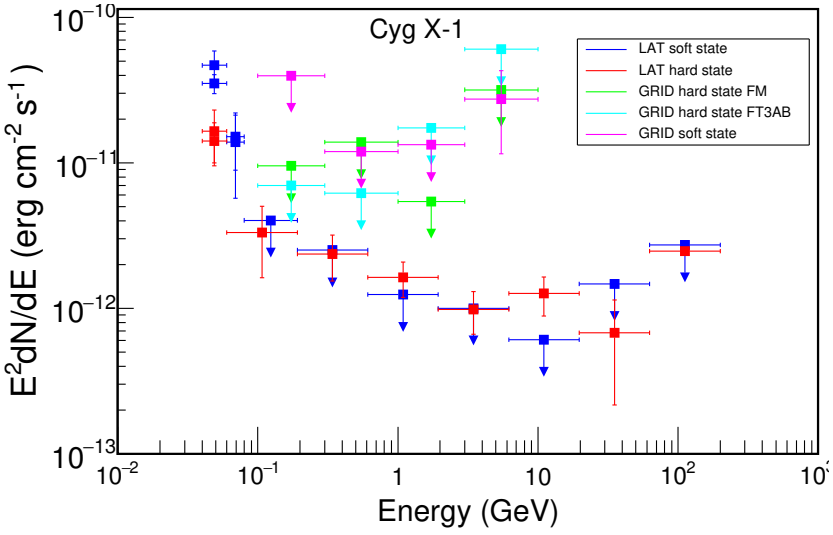

Figure 6.3: *AGILE*/GRID ULs for the energy flux, calculated with model L, compared with LAT measurements of Zdziarski *et al.* (2017). The GRID data for the soft state were computed with filter FM, filter FT3AB gives similar results. LAT data kindly provided by Andrzej Zdziarski.

Results of fitting in narrow energy ranges presented in Table 6.6, and consistently the com-

parison of results presented in Tables 6.4 and 6.5 (higher TS in the former, including events with energies above 3 GeV), indicates that the γ-ray signal in the soft state of Cyg X-1 is mainly induced by contributions of both photons with $E < 0.3$ GeV and those with $E > 3$ GeV. Contribution of the lowest energy photons, with $E < 0.3$ GeV, is significantly reduced in model L compared to model G. This again reflects a contaminating effect of S15, whose distance of $\simeq 2.5^\circ$ is comparable to the GRID PSF below 300 MeV. Interestingly, though, the intensity map for the soft state in Figure 6.4, which is dominated by the (most numerous) low energy photons, shows a clear signal[9] concentrated on the position of Cyg X-1. Also the UL for the soft state in the 0.1–0.3 GeV range, shown in Figure 6.3, is a few times larger than the UL in the hard state, although both were derived using the same model L (taking into account presence of S15).

Events with energies above 3 GeV are sparsely detected and even a single photon with such energies can significantly affect the results. The *AGILE* analysis software does not allow to examine individual events in a manner similar, e.g., to `gtsrcprob` of the LAT analysis package. Therefore, I was not able to investigate the nature of signal at $E > 3$ GeV in more details (number of events, their energies, distance from Cyg X-1, time of detection).

Energy GeV	$\sqrt{\text{TS}}$	UL or F_γ model G	$\sqrt{\text{TS}}$	UL or F_γ model L
0.1–0.3	4.4	18.5 ± 0.8	0.6	< 16.5
0.3–1	0	< 2.2	0	< 1.7
1–3	0	< 0.7	0	< 0.6
3–10	2.7	0.4 ± 0.2	2.6	0.4 ± 0.2
10–50	0.7	< 3.9	0	< 2.9

Table 6.6: The detection significance and either the photon flux, F_γ (for $\sqrt{\text{TS}} > 2$), or 95% confidence level UL on F_γ (for $\sqrt{\text{TS}} < 2$) for the soft state with the assumed Γ=2.4 for 5 energy bands performed with FM filter for model G and L. F_γ/UL is given in the unit of 10^{-8} ph/cm^2/s. The corresponding ULs on the energy flux are shown in Figure 6.3.

As discussed above, inclusion of additional γ-ray sources, most importantly S15, in modeling the region around Cyg X-1, significantly affects the fitting results. This motivated me to revisit also the three *AGILE* flares noted in Chapter 6.2.2. Results of my analysis are shown in Table 6.7.

I first fitted the GRID data for the flares using model G and for flares 1 and 2 I obtained parameters similar to those reported by Sabatini *et al.* (2010) and Bulgarelli *et al.* (2010). For flare 3 I did not find a significant detection; Sabatini *et al.* (2013) notes a low statistical significance for their results concerning this flare candidate, but they do not report the flux or specific TS value. With model L I found that the significance of flare 2 is also reduced below the detection threshold. For flare 1 the signal remains marginally significant.

Then, I also analyzed the LAT data for the three *Fermi* 3σ flares, reported by Bodaghee *et al.* (2013), approximately coincident with the *AGILE*. In all three cases I found that using an updated model of the region, i.e. including all FL8Y sources, gives TS=0.

[9] this apparent signal, at the level of 3.5×10^{-4} counts cm^{-2} s^{-1} sr^{-1}, is better visible on the electronic version of this figure

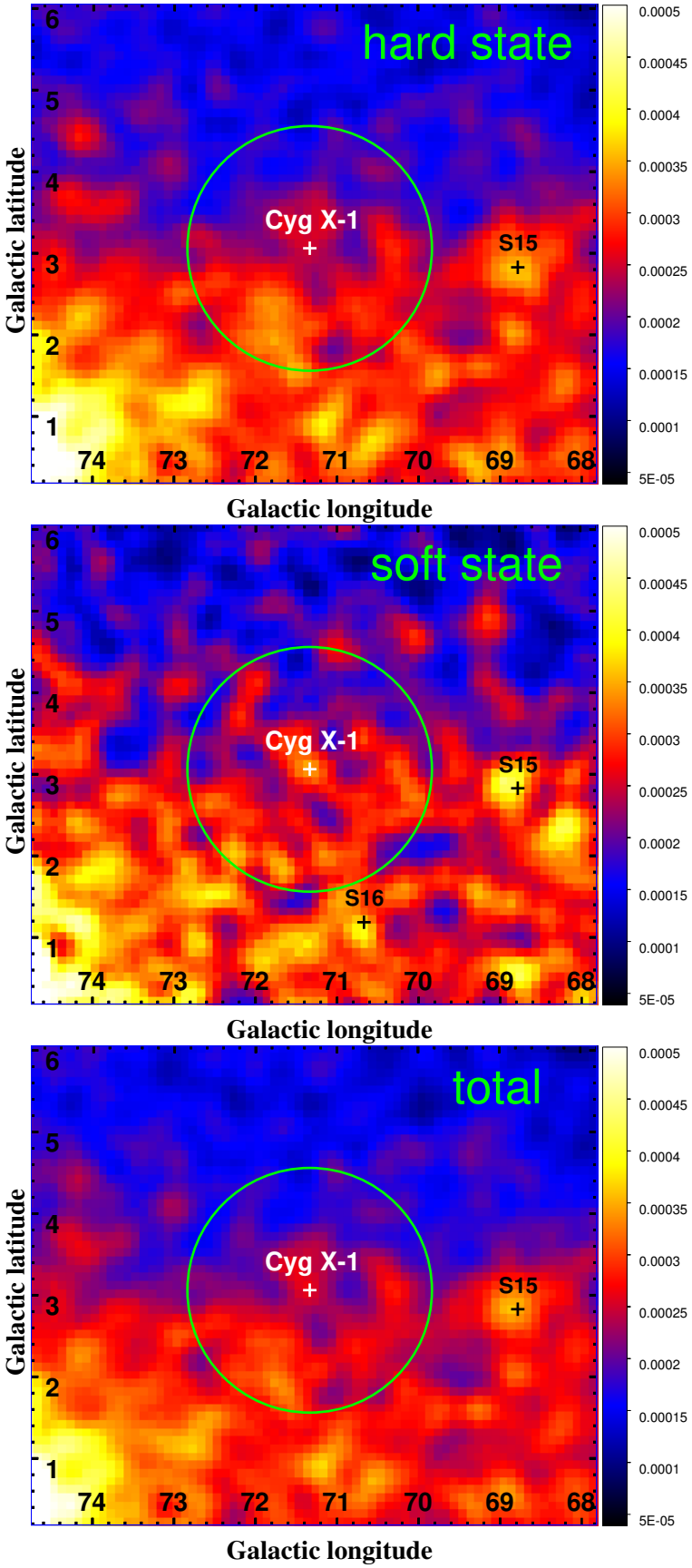

Figure 6.4: Intensity maps of the Cyg X-1 region computed with filter FM for the hard (top) and the soft (middle) spectral states and the total dataset (bottom) with the pixel size of 0.1°, displayed with the 3-bin Gaussian smoothing. The circle with the radius of 1.5° around the position of Cyg X-1 is the same as in Figure 6.2.

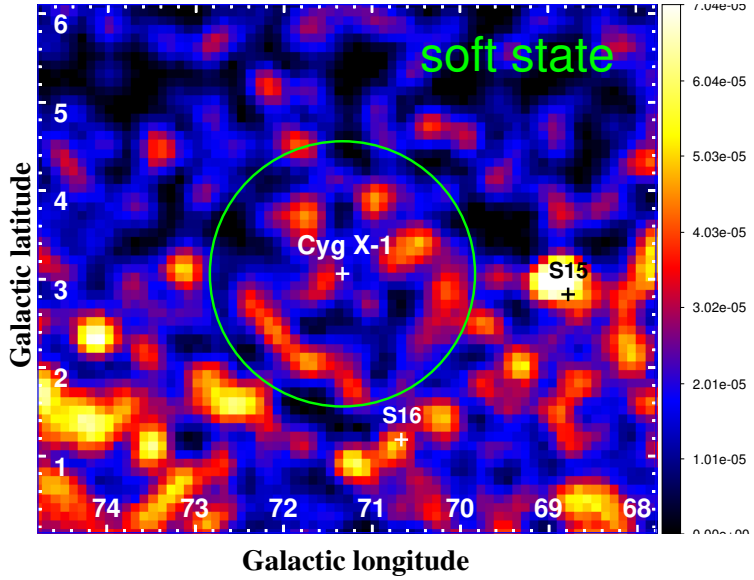

Figure 6.5: Intensity map of the Cyg X-1 region computed for the soft spectral state, similar to the middle panel of Figure 6.4 but using only events with $E > 1$ GeV.

Filter	Γ	$\sqrt{TS}$	F_γ model G	$\sqrt{TS}$	F_γ model L
Flare 1					
FM	2.1	3.8	1.6 ± 0.6	2.9	1.3 ± 0.6
FM	2.4	3.7	2.1 ± 0.7	2.8	1.7 ± 0.7
FT3AB	2.1	4.8	2.5 ± 0.8	3.1	1.7 ± 0.7
FT3AB	2.4	4.7	3.2 ± 0.9	2.9	2.3 ± 0.9
Flare 2					
FM	2.1	4.5	4.7 ± 0.2	1	
FM	2.4	4.4	5.9 ± 0.2	0.8	
FT3AB	2.1	2.3	3 ± 1.9	0.9	
FT3AB	2.4	2.4	4.3 ± 2.5	0.8	
Flare 3					
FM	2.1	2.0	< 3.3	2.0	< 1.6
FM	2.4	1.9	< 4.1	1.9	< 4.1
FT3AB	2.1	0.8	< 2.7	0.7	< 2.6
FT3AB	2.4	0.7	< 3.5	0.6	< 3.4

Table 6.7: Fitting results for the three GRID flares, observed on 15/16 October 2009 (flare 1), 24/25 March 2010 (flare 2) and 30 June/2 July 2010 (flare 3), see Chapter 6.2.2, for two values of Γ fixed for Cyg X-1 and both GRID filters. The photon flux above 100 MeV, F_γ (for $\sqrt{TS} > 2$), or UL (for $\sqrt{TS} \leq 2$), are given in the unit of 10^{-6} ph/cm^2/s.

6.5 Summary and discussion

Recent detection of persistent γ-ray emission from Cyg X-1 by *Fermi*/LAT motivated me to search for a signal in the *AGILE* data. I extended previous works by including about 5 years of GRID observations which were not analyzed before. I have not found a signal in the hard state and the lack of detection is likely mostly due to a smaller effective area of GRID. Cyg X-1 is located in the Galactic plane, therefore, details of modeling of the Galactic background may also affect the analysis results. Here it is worth noting that LAT analysis uses probably a more accurate model of ISM distribution, which is calculated on a finer spatial grid with $0.125^\circ \times 0.125^\circ$ binning, as compared to $0.25^\circ \times 0.25^\circ$ bins used for GRID analysis; also, the ISM templates used for both instrument use the CO 2.6-mm line as a tracer of ISM, but the LAT model improves it by including an additional tracer involving the dust distribution[10].

The effective area of LAT[11] is by a factor of $\sim 5-10$ larger than that of GRID (given, e.g., in Chen *et al.*, 2013) below 1 GeV, and the difference increases with increasing photon energy above 1 GeV. Still, there were some cases when simultaneous observations gave detection by GRID and no signal in LAT data, most notably for MWC 656 (see Chapter 1.4). Munar-Adrover *et al.* (2016) argue that this may be explained by a favorable exposure in GRID, as both instruments are characterized by a significant dependence of their effective areas on the off-axis angle.

AGILE is optimized for observations in the 100–400 MeV range. Indeed, my results presented in Figure 6.3 indicate that the sensitivity of the accumulated GRID observations approaches the level needed for a detection most closely in this energy range and the detection could be achieved with a few more years of hard state data (assuming that LAT measurement properly represents the persistent γ-ray flux in this state).

A particularly interesting result could be obtained by including in my analysis the data for energies below 100 MeV, where Zdziarski *et al.* (2017) claim a detection of Cyg X-1 in the LAT data in both the hard and soft state (see their discussion of related uncertainties and of the physical interpretation of this component), see Figure 6.3. However, the LAT PSF of several degrees in this energy range makes this result subject to significant uncertainty related with confusion by nearby sources and an independent hint for this γ-ray flux would valuably complement this LAT finding. The GRID effective area at 60 MeV is by less than a factor of 2 lower than at 100 MeV, then, looking at LAT flux values and GRID ULs in Figure 6.3 it seems that a detection might be within reach of GRID. Unfortunately, the GRID data below 100 MeV are not publicly available.

I updated the model of the region by including all γ-ray sources reported by LAT. Actually, the γ-ray pulsar PSR J1952+3252 (S15) which has been detected in some previous studies of GRID data, but missed in the studies of Cyg X-1 (see e.g. an explicit discussion of this issue in Del Monte *et al.*, 2010) appears the most important for the fitting results. Taking into account the presence of this source, I obtained significantly undermined detection of the previously reported *AGILE* flares, with a marginal $\sim 3\sigma$ significance remaining only for the first flare, observed in October 2009. Crucially, only this flare was detected in the pointing mode.

Interpretation of the γ-ray signal revealed in the soft state is somewhat ambiguous. After subtracting the contribution from PSR J1952+3252, its significance is lower than 3σ, indicating

[10] https://fermi.gsfc.nasa.gov/ssc/data/access/lat/Model_details/FSSC_model_diffus_reprocessed_v12.pdf
[11] http://www.slac.stanford.edu/exp/glast/groups/canda/lat_Performance.htm

that it can be a statistical fluctuation. Nevertheless, a clear concentration of the low energy photons around Cyg X-1, seen in the intensity map, accompanied by detection of some events with $E > 3$ GeV, is worth noting and encourages to search for flare events in the soft state data added in my analysis.

Chapter 7

Summary and conclusions

The most widely accepted model of accretion at low accretion rates is that of optically-thin, hot flows. Such flows are supported by the proton pressure, so proton energies must be high. Then, the production of pions in collisions of these energetic protons should be the generic property of such flows. If this is true, a lack of detection of a related γ-ray signal could be regarded as an argument against this class of models. In Chapter 3 I thoroughly investigated this prediction, considering the dependence on several phenomenological parameters of MHD processes as well as black hole spin and accretion rate. This was the first such a detailed study in literature. I found that although indeed large amounts of γ-ray photons are produced in hot flows, their escaping flux is severely reduced by internal $\gamma\gamma$ absorption. I conclude that the apparent γ-ray quietness of low-luminosity systems in general does not contradict the model predictions.

Still, for some parameters the predicted fluxes can be probed with the current sensitivity of LAT. The major uncertainty of the model concerns the direct heating of electrons, which determines the accretion rate (and hence the density) for a given X-ray luminosity. I noted some effects which seem to disfavor a strong direct heating (however, a conclusive estimation of this property would require a direct X-ray fitting, which is beyond the scope of my thesis). The discussion below assumes that the accretion power goes mostly to protons (and I emphasize that it is not valid if this assumption is incorrect).

In Chapter 4 I compared the prediction of the model with several well-studied AGNs, for which the available data allowed a robust determination of the nuclear luminosity scaled by the Eddington value. I found that if most of the accretion power is used for the relativistic acceleration of a small fraction of protons, the predicted γ-ray flux exceeds the LAT upper limit for NGC 4258, NGC 7213 and NGC 4151 by a factor of several. Thus, the *Fermi* upper limits provide an interesting constraint on the MHD processes that convert the accretion power into the kinetic energy of protons. Namely, it should uniformly heat all protons rather than relativistically accelerate some of them (at most a few per cent of the power may be used for such processes). Again, this is the first observational estimation of such effects in literature.

If the nonthermal acceleration is weak, observable fluxes of γ-ray photons are predicted for weakly magnetized flows around rapidly rotating black holes. I found that for two Seyfert galaxies, NGC 7213 and NGC 4151, the LAT upper limits rule out this combinations of parameters.

For NGC 4151 I found a γ-ray signal with over 4σ significance in the LAT data. This result is somewhat ambiguous due to the presence of nearby BL Lac object, but I note further arguments

(in particular, a clear concentration of the signal below 1 GeV around NGC 4151) supporting the reality of the γ-ray signal originating from NGC 4151. I note that future observations with e-ASTROGAM can verify if the signal is related with hadronic processes, as characteristic π^0-decay features below 1 GeV would be easily measured with the planned sensitivity of this instrument.

The γ-ray loud Seyfert 2 galaxies radiate at a much higher Eddington ratio than other nearby AGNs, possibly as a result of enhanced fueling that is related with starburst activity in their nuclear regions. I considered in detail one of these galaxies, NGC 4945, where X-ray emission from the nucleus can be directly probed. In Chapter 5 I presented a novel approach to investigate its γ-ray variability by analyzing the LAT data selected based on the X-ray flux level. The γ-ray spectrum appears to be correlated with the X-ray luminosity, with changes of the γ-ray signal independently seen at low and high γ-ray energies. The X/γ-ray correlation is indicated by all datasets (comprising between $\sim$ 1 and 4 years of LAT data) selected using the X-ray flux criterion, while datasets neglecting this criterion are consistent with representing a non-varying γ-ray emission. I have thoroughly tested the dependence of my results on the approach to data analysis.

The correlation implies that dominating contribution to the observed γ-ray emission comes from the active nucleus of NGC 4945 and this constrains the efficiency of γ-ray production related with starburst activity. The implied limit on the radiative efficiency (with $\lesssim 20\%$ of the cosmic ray power lost in pionic interactions, if the IR luminosity is used as a measure of the star-formation rate) is slightly lower than the efficiencies assessed for NGC 253 and M 82.

The nature of this nuclear γ-ray source may be different at low and high X-ray luminosities. At the latter, the γ-ray transparency and the causality conditions require the source to be located $\sim (10^3 - 10^4) R_{\rm g}$ away from the central black hole, if an inner optically-thick disc is present and the X-ray source is close to the black hole. I speculate that such a γ-ray emitting site may appear as a result of an inwards collapse of accretion disc, associated with the increase of luminosity. Then, it may manifest the disc-jet connection established in other accreting systems. At low X-ray luminosities, the source may be located much closer to the black hole.

I noted similarities between NGC 4945, NGC 1068 and Circinus (similar Eddington ratios of high-energy emission, lack of TeV detections, unlikely high efficiencies of γ-ray production in starburst scenario) which I regard as a further argument for a dominating contribution of their active nuclei to the γ-ray emission.

I also took into account observations from the other operating γ-ray satellite, *AGILE*. Although I used data set for Cyg X-1 about twice longer than used in previous studies, I found that, it is still not sufficient to confirm the LAT detection of this source, by using the current public software, diffuse emission model and calibrations. My assessments indicate that *AGILE* may be able to measure the γ-ray flux below 100 MeV at the level reported by Zdziarski *et al.* (2017). Such an analysis requires the use of data which are not public and I hope to make this investigation in collaboration with the AGILE Data Center Team. I investigated and discussed effects related with a proper modeling, including all γ-ray sources in this region of sky, which affects, in particular, parameters of flares previously reported from this black hole binary.

Symbols, definitions and abbreviations

Symbols and constants

L	Luminosity; bolometric luminosity is meant if the energy range is not specified by the subscript
a	Dimensionless black hole spin parameter, equation (1.1)
β	The ratio of the gas pressure (electron and proton) to the magnetic pressure
δ	The fraction of the dissipated energy that directly heats electrons
$\eta_{\rm p}$	Energy content of nonthermal protons; it also gives the efficiency of their relativistic acceleration, because protons retain the distribution achieved in the heating/acceleration process
Γ	γ-ray photon spectral index
$\mathcal{F}_\gamma$	Integrated photon flux in the γ-ray range; the flux above 100 MeV is meant if the energy range is not specified
$\mathcal{F}_{\rm X}, \overline{\mathcal{F}}_{\rm X}$	Daily and average, respectively, BAT count rates, used in Chapter 5
$\sigma_{\rm T}$	Thomson cross-section for electron scattering
τ	Thomson optical depth
$M_\odot$	Mass of the Sun
$L_{\rm Edd}$	Eddington luminosity, equation (1.3)
$m_{\rm p}$	Proton mass
G	Gravitational constant
c	Speed of light
Z	Atomic number
$\dot{M}_{\rm Edd}$	$\equiv L_{\rm Edd}/c^2$
λ	$\equiv L/L_{\rm Edd}$
$\dot{M}$	Accretion rate in physical units

$\dot{m}$ $\equiv \dot{M}/\dot{M}_{\rm Edd}$

$R_{\rm g}$ Gravitational radius, equation (1.2)

R Distance in physical units

r $\equiv R/R_{\rm g}$

Abbreviations

1AGLR Updated catalog of *AGILE*/GRID bright γ-ray sources

3FGL The Third *Fermi* Gamma-Ray LAT Catalog

AGN Active Galaxy Nucleus

BAT hard X-ray detector on board *Swift* satellite

BHB Black hole binary

CTA Cherenkov Telescope Array

FL8Y *Fermi*/LAT 8-year Point Source List; see the note in Chapter 2.3.5

FOV Field of view

FT3AB, FM Filters used in *AGILE*/GRID data analysis

GR General relativity

GRID Gamma-ray Imaging Detector on board *AGILE* satellite

HMXB High-mass X-ray binary

IACT Imaging Air Cherenkov Telescope

IR Infrared

IRF Instrument response function

LAT γ-ray detector on board *Fermi* satellite

LMXB Low-mass X-ray binary

MC Monte Carlo

MHD Magnetohydrodynamic

P7REP *Fermi*/LAT data releases, see Chapter 2.3.3

Pass 7 –"–

Pass 8 –"–

PSF Point Spread Function

ROI	Region of interest
SED	Spectral energy distribution
TS	Test statistics
UL	Upper limit, 95% confidence level ULs given in all cases

References

1. Abbott, B. P. *et al.* Multi-messenger Observations of a Binary Neutron Star Merger. *The Astrophysical Journal Letters* **848,** L12 (Oct. 2017).
2. Abbott, B. P. *et al.* Observation of Gravitational Waves from a Binary Black Hole Merger. *Physical Review Letters* **116,** 061102 (Feb. 2016).
3. Abdo, A. A. *et al.* Detection of Gamma-Ray Emission from the Starburst Galaxies M82 and NGC 253 with the Large Area Telescope on Fermi. *Astrophysical Journal, Letters* **709,** L152–L157 (Feb. 2010).
4. Abdo, A. A. *et al.* Fermi Large Area Telescope First Source Catalog. *Astrophysical Journal, Supplement* **188,** 405–436 (June 2010).
5. Abdo, A. A. *et al.* Fermi Observations of High-Energy Gamma-Ray Emission from GRB 080916C. *Science* **323,** 1688 (Mar. 2009).
6. Abdo, A. A. *et al.* The Fermi Gamma-Ray Space Telescope Discovers the Pulsar in the Young Galactic Supernova Remnant CTA 1. *Science* **322,** 1218 (Nov. 2008).
7. Abramowicz, M. A., Chen, X., Kato, S., Lasota, J.-P. & Regev, O. Thermal equilibria of accretion disks. *Astrophysical Journal* **438,** L37–L39 (Jan. 1995).
8. Acero, F. *et al.* Detection of Gamma Rays from a Starburst Galaxy. *Science* **326,** 1080 (Nov. 2009).
9. Acero, F. *et al.* Fermi Large Area Telescope Third Source Catalog. *Astrophysical Journal, Supplement* **218,** 23 (June 2015).
10. Ackermann, M. *et al.* Deep view of the Large Magellanic Cloud with six years of Fermi-LAT observations. *Astronomy and Astrophysics* **586,** A71 (Feb. 2016).
11. Ackermann, M. *et al.* GeV Observations of Star-forming Galaxies with the Fermi Large Area Telescope. *Astrophysical Journal* **755,** 164 (Aug. 2012).
12. Ackermann, M. *et al.* Observations of M31 and M33 with the Fermi Large Area Telescope: A Galactic Center Excess in Andromeda? *Astrophysical Journal* **836,** 208 (Feb. 2017).
13. Ackermann, M. *et al.* Search for Gamma-ray Emission from X-Ray-selected Seyfert Galaxies with Fermi-LAT. *Astrophysical Journal* **747,** 104 (Mar. 2012).
14. Ackermann, M. *et al.* The Fermi Large Area Telescope on Orbit: Event Classification, Instrument Response Functions, and Calibration. *The Astrophysical Journal Supplement* **203,** 4 (Nov. 2012).

15. Ackermann, M. *et al.* The Spectrum and Morphology of the Fermi Bubbles. *Astrophysical Journal* **793,** 64 (Sept. 2014).

16. Ackermann, M. *et al.* The Third Catalog of Active Galactic Nuclei Detected by the Fermi Large Area Telescope. *Astrophysical Journal* **810,** 14 (Sept. 2015).

17. Actis, M. *et al.* Design concepts for the Cherenkov Telescope Array CTA: an advanced facility for ground-based high-energy gamma-ray astronomy. *Experimental Astronomy* **32,** 193–316 (Dec. 2011).

18. Ahnen, M. L. *et al.* Search for very high-energy gamma-ray emission from the microquasar Cygnus X-1 with the MAGIC telescopes. *Monthly Notices of the RAS* **472,** 3474–3485 (Dec. 2017).

19. Ajello, M. *et al.* 3FHL: The Third Catalog of Hard Fermi -LAT Sources. *The Astrophysical Journal Supplement Series* **232,** 18 (2017).

20. Ajello, M. *et al.* Impulsive and Long Duration High-energy Gamma-Ray Emission from the Very Bright 2012 March 7 Solar Flares. *Astrophysical Journal* **789,** 20 (July 2014).

21. Ajello, M. *et al.* The Swift BAT X-Ray Survey. III. X-Ray Spectra and Statistical Properties. *Astrophysical Journal* **673,** 96–113 (Jan. 2008).

22. Albert, J. *et al.* Very High Energy Gamma-Ray Radiation from the Stellar Mass Black Hole Binary Cygnus X-1. *Astrophysical Journall* **665,** L51–L54 (Aug. 2007).

23. Alexander, M. J. & McSwain, M. V. An updated gamma-ray analysis of the Be-BH binary HD 215227. *Monthly Notices of the RAS* **449,** 1686–1690 (May 2015).

24. Antonucci, R. Unified models for active galactic nuclei and quasars. *Annual Review of Astron and Astrophys* **31,** 473–521 (1993).

25. Arévalo, P. *et al.* The 2-79 keV X-Ray Spectrum of the Circinus Galaxy with NuSTAR, XMM-Newton, and Chandra: A Fully Compton-thick Active Galactic Nucleus. *Astrophysical Journal* **791,** 81 (Aug. 2014).

26. Atwood, W. B. *et al.* The Large Area Telescope on the Fermi Gamma-Ray Space Telescope Mission. *Astrophysical Journal* **697,** 1071–1102 (June 2009).

27. Barbiellini, G. *et al.* A wide aperture telescope for high energy gamma rays detection. *Nuclear Physics B Proceedings Supplements* **43,** 253–256 (June 1995).

28. Barbiellini, G. *et al. NINA: a lightweight silicon strip detector for cosmic ray research in space* in *Space Telescopes and Instruments* (eds Bely, P. Y. & Breckinridge, J. B.) **2478** (June 1995), 239–249. doi:10.1117/12.210929.

29. Barbiellini, G. *et al.* The GILDA mission: a new technique for a gamma-ray telescope in the energy range 20 MeV-100 GeV. *Nuclear Instruments and Methods in Physics Research A* **354,** 547–552 (Feb. 1995).

30. Bauer, F. E. *et al.* NuSTAR Spectroscopy of Multi-component X-Ray Reflection from NGC 1068. *Astrophysical Journal* **812,** 116 (Oct. 2015).

31. Beckmann, V., Jean, P., Lubiński, P., Soldi, S. & Terrier, R. The hard X-ray emission of Centaurus A. *Astronomy and Astrophysics* **531,** A70 (July 2011).

32. Belloni, T. *et al.* An Intermediate State of Cygnus X-1. *Astrophysical Journal, Letters* **472,** L107 (Dec. 1996).

33. Bentz, M. C. *et al.* The Lick AGN Monitoring Project: Broad-line Region Radii and Black Hole Masses from Reverberation Mapping of Hβ. *Astrophysical Journal* **705,** 199–217 (Nov. 2009).

34. Bisnovatyi-Kogan, G. S. & Lovelace, R. V. E. Influence of Ohmic Heating on Advection-dominated Accretion Flows. *Astrophysical Journal, Letters* **486,** L43–L46 (Sept. 1997).

35. Bodaghee, A. *et al.* Gamma-Ray Observations of the Microquasars Cygnus X-1, Cygnus X-3, GRS 1915+105, and GX 339-4 with the Fermi Large Area Telescope. *Astrophysical Journal* **775,** 98 (Oct. 2013).

36. Bowyer, S., Byram, E. T., Chubb, T. A. & Friedman, H. Cosmic X-ray Sources. *Science* **147,** 394–398 (1965).

37. Brenneman, L. W., Elvis, M., Krongold, Y., Liu, Y. & Mathur, S. NGC 5548: Lack of a Broad Fe Kα Line and Constraints on the Location of the Hard X-Ray Source. *Astrophysical Journal* **744,** 13 (Jan. 2012).

38. Brenneman, L. W. *et al.* The Broad-band X-Ray Spectrum of IC 4329A from a Joint NuSTAR/Suzaku Observation. *Astrophysical Journal* **788,** 61 (June 2014).

39. Briggs, M. S. *et al.* Electron-positron beams from terrestrial lightning observed with Fermi GBM. *Geophysical Research Letters* **38,** L02808 (Jan. 2011).

40. Briggs, M. S. *et al.* Terrestrial gamma-ray flashes in the Fermi era: Improved observations and analysis methods. *Journal of Geophysical Research (Space Physics)* **118,** 3805–3830 (June 2013).

41. Bulgarelli, A. *et al.* AGILE detection of a gamma ray flare from the Cygnus X-1 region. *The Astronomer's Telegram* **2512** (Mar. 2010).

42. Bulgarelli, A. *et al.* AGILE detection of Cygnus X-3 γ-ray active states during the period mid-2009/mid-2010. *Astronomy and Astrophysics* **538,** A63 (Feb. 2012).

43. Burke, M. J., Gilfanov, M. & Sunyaev, R. A dichotomy between the hard state spectral properties of black hole and neutron star X-ray binaries. *Monthly Notices of the RAS* **466,** 194–212 (Apr. 2017).

44. Caballero-Garcia, M. D., Papadakis, I. E., Nicastro, F. & Ajello, M. Hard X-ray spectral variability of the brightest Seyfert AGN in the Swift/BAT sample. *Astronomy and Astrophysics* **537,** A87 (Jan. 2012).

45. Cappellari, M. *et al.* The mass of the black hole in Centaurus A from SINFONI AO-assisted integral-field observations of stellar kinematics. *Monthly Notices of the RAS* **394,** 660–674 (Apr. 2009).

46. Casares, J. & Jonker, P. G. Mass Measurements of Stellar and Intermediate-Mass Black Holes. *Space Science Reviews* **183,** 223–252 (Sept. 2014).

47. Cash, W. Parameter estimation in astronomy through application of the likelihood ratio. *Astrophysical Journal* **228,** 939–947 (Mar. 1979).

48. Cerutti, B. *et al.* Absorption of high-energy gamma rays in Cygnus X-3. *Astronomy and Astrophysics* **529,** A120 (May 2011).

49. Chen, A. W. *et al.* Calibration of AGILE-GRID with in-flight data and Monte Carlo simulations. *Astronomy and Astrophysics* **558,** A37 (Oct. 2013).

50. Chen, A. W. *et al.* Study of the γ-ray source 1AGL J2022+4032 in the Cygnus region. *Astronomy and Astrophysics* **525,** A33 (Jan. 2011).

51. Corbel, S. *et al.* A giant radio flare from Cygnus X-3 with associated γ-ray emission. *Monthly Notices of the RAS* **421,** 2947–2955 (Apr. 2012).

52. Cui, W., Feng, Y.-X. & Ertmer, M. A Peculiar Flaring Episode of Cygnus X-1. *The Astrophysical Journal* **564,** L77–L80 (Jan. 2002).

53. De Angelis, A. *et al.* The e-ASTROGAM mission. Exploring the extreme Universe with gamma rays in the MeV - GeV range. *Experimental Astronomy* **44,** 25–82 (Oct. 2017).

54. Del Monte, E. *et al.* A year-long AGILE observation of Cygnus X-1 in hard spectral state. *Astronomy and Astrophysics* **520,** A67 (Sept. 2010).

55. Dermer, C. D., Miller, J. A. & Li, H. Stochastic Particle Acceleration near Accreting Black Holes. *Astrophysical Journal* **456,** 106 (Jan. 1996).

56. Di Matteo, T., Springel, V. & Hernquist, L. Energy input from quasars regulates the growth and activity of black holes and their host galaxies. *Nature* **433,** 604–607 (Feb. 2005).

57. Diamond-Stanic, A. M. & Rieke, G. H. The Relationship between Black Hole Growth and Star Formation in Seyfert Galaxies. *Astrophysical Journal* **746,** 168 (Feb. 2012).

58. Done, C. *Scaling accretion flow models from BHB to AGN - Why doesn't it work?* - in *Suzaku-MAXI 2014: Expanding the Frontiers of the X-ray Universe* (eds Ishida, M., Petre, R. & Mitsuda, K.) (Sept. 2014), 300. arXiv: 1405.2762 [astro-ph.HE].

59. Done, C., Wardziński, G. & Gierliński, M. GRS 1915+105: the brightest Galactic black hole. *Monthly Notices of the RAS* **349,** 393–403 (Apr. 2004).

60. Done, C., Gierliński, M. & Kubota, A. Modelling the behaviour of accretion flows in X-ray binaries. Everything you always wanted to know about accretion but were afraid to ask. *Astronomy and Astrophysics* **15,** 1–66 (Dec. 2007).

61. Done, C., Madejski, G. M., Życki, P. T. & Greenhill, L. J. Simultaneous Chandra and Rossi X-Ray Timing Explorer Observations of the Nearby Bright Seyfert 2 Galaxy NGC 4945. *Astrophysical Journal* **588,** 763–770 (May 2003).

62. Droulans, R., Belmont, R., Malzac, J. & Jourdain, E. Variability and Spectral Modeling of the Hard X-ray Emission of GX 339-4 in a Bright Low/Hard State. *Astrophysical Journal* **717,** 1022–1036 (July 2010).

63. Dubus, G., Cerutti, B. & Henri, G. Relativistic Doppler-boosted emission in gamma-ray binaries. *Astronomy and Astrophysics* **516,** A18 (June 2010).

64. Edelson, R. *et al.* Space Telescope and Optical Reverberation Mapping Project. II. Swift and HST Reverberation Mapping of the Accretion Disk of NGC 5548. *Astrophysical Journal* **806,** 129 (June 2015).

65. Eichmann, B. & Becker Tjus, J. The Radio-Gamma Correlation in Starburst Galaxies. *Astrophysical Journal* **821,** 87 (Apr. 2016).

66. Elmouttie, M., Haynes, R. F., Jones, K. L., Sadler, E. M. & Ehle, M. Radio continuum evidence for nuclear outflow in the Circinus galaxy. *Monthly Notices of the RAS* **297,** 1202–1218 (July 1998).

67. Esin, A. A., McClintock, J. E. & Narayan, R. Advection-Dominated Accretion and the Spectral States of Black Hole X-Ray Binaries: Application to Nova Muscae 1991. *Astrophysical Journal* **489,** 865–889 (Nov. 1997).

68. Fasano, G. & Franceschini, A. A multidimensional version of the Kolmogorov-Smirnov test. *Monthly Notices of the RAS* **225,** 155–170 (Mar. 1987).

69. Fender, R. P., Belloni, T. M. & Gallo, E. Towards a unified model for black hole X-ray binary jets. *Monthly Notices of the RAS* **355,** 1105–1118 (Dec. 2004).

70. Fermi LAT Collaboration *et al.* Modulated High-Energy Gamma-Ray Emission from the Microquasar Cygnus X-3. *Science* **326,** 1512 (Dec. 2009).

71. Ferrarese, L. & Merritt, D. A Fundamental Relation between Supermassive Black Holes and Their Host Galaxies. *Astrophysical Journal Letters* **539,** L9–L12 (Aug. 2000).

72. Fichtel, C. E. *et al.* High-energy gamma-ray results from the second small astronomy satellite. *Astrophysical Journal* **198,** 163–182 (May 1975).

73. Fisher, R. *Statistical Methods For Research Workers* ISBN: 9788130701332. <https://books.google.pl/books?id=4bTttAJR5kEC> (Cosmo Publications, 1925).

74. Frank, J., King, A. & Raine, D. J. *Accretion Power in Astrophysics: Third Edition* 398 (Jan. 2002).

75. Frontera, F. *et al.* Broadband Spectrum of Cygnus X-1 in Two Spectral States with BeppoSAX. *Astrophysical Journal* **546,** 1027–1037 (Jan. 2001).

76. Fukazawa, Y. *et al.* Suzaku View of X-Ray Spectral Variability of the Radio Galaxy Centaurus A: Partial Covering Absorber, Reflector, and Possible Jet Component. *Astrophysical Journal* **743,** 124 (Dec. 2011).

77. Galli, M. *et al.* AGILE mini-calorimeter gamma-ray burst catalog. *Astronomy and Astrophysics* **553,** A33 (May 2013).

78. Gallimore, J. F., Axon, D. J., O'Dea, C. P., Baum, S. A. & Pedlar, A. A Survey of Kiloparsec-Scale Radio Outflows in Radio-Quiet Active Galactic Nuclei. *Astronomical Journal* **132,** 546–569 (Aug. 2006).

79. Gallo, E. *et al.* A dark jet dominates the power output of the stellar black hole Cygnus X-1. *Nature* **436,** 819–821 (Aug. 2005).

80. Gammie, C. F. & Popham, R. Advection-dominated Accretion Flows in the Kerr Metric. I. Basic Equations. *Astrophysical Journal* **498,** 313–326 (May 1998).

81. Gebhardt, K. *et al.* A Relationship between Nuclear Black Hole Mass and Galaxy Velocity Dispersion. *Astrophysical Journal Letters* **539,** L13–L16 (Aug. 2000).

82. Ghisellini, G., Tavecchio, F., Foschini, L. & Ghirlanda, G. The transition between BL Lac objects and flat spectrum radio quasars. *Monthly Notices of the RAS* **414,** 2674–2689 (July 2011).

83. Gierliński, M. *et al.* Radiation mechanisms and geometry of Cygnus X-1 in the soft state. *Monthly Notices of the RAS* **309,** 496–512 (Oct. 1999).

84. Gierlinski, M. *et al.* Simultaneous X-ray and gamma-ray observations of CYG X-1 in the hard state by GINGA and OSSE. *Monthly Notices of the RAS* **288,** 958–964 (July 1997).

85. Giuliani, A. *et al.* Neutral Pion Emission from Accelerated Protons in the Supernova Remnant W44. *Astrophysical Journal* **742,** L30 (Dec. 2011).

86. Golenetskii, S. *et al.* Observations of Giant Outbursts from Cygnus X-1. *The Astrophysical Journal* **596,** 1113–1120 (Oct. 2003).

87. Gondek, D. *et al.* The average X-ray/gamma-ray spectrum of radio-quiet Seyfert 1s. *Monthly Notices of the RAS* **282,** 646–652 (Sept. 1996).

88. Greenhill, L. J. *et al.* A Warped Accretion Disk and Wide-Angle Outflow in the Inner Parsec of the Circinus Galaxy. *Astrophysical Journal* **590,** 162–173 (June 2003).

89. Greenhill, L. J., Moran, J. M. & Herrnstein, J. R. The Distribution of H_2O Maser Emission in the Nucleus of NGC 4945. *Astrophysical Journal, Letters* **481,** L23–L26 (May 1997).

90. Greenhill, L. J., Gwinn, C. R., Antonucci, R. & Barvainis, R. VLBI Imaging of Water Maser Emission from the Nuclear Torus of NGC 1068. *Astrophysical Journal, Letters* **472,** L21 (Nov. 1996).

91. Griffin, R. D., Dai, X. & Thompson, T. A. Constraining Gamma-Ray Emission from Luminous Infrared Galaxies with Fermi-LAT; Tentative Detection of Arp 220. *Astrophysical Journal, Letters* **823,** L17 (May 2016).

92. Grinberg, V. *et al.* Long term variability of Cygnus X-1. V. State definitions with all sky monitors. *Astronomy and Astrophysics* **554,** A88 (June 2013).

93. Harris, G. L. H., Rejkuba, M. & Harris, W. E. The Distance to NGC 5128 (Centaurus A). *Pasa* **27,** 457–462 (Oct. 2010).

94. Hayashida, M. *et al.* Discovery of GeV Emission from the Circinus Galaxy with the Fermi Large Area Telescope. *Astrophysical Journal* **779,** 131 (Dec. 2013).

95. Helene, O. Determination of the upper limit of a peak area. *Nuclear Instruments and Methods in Physics Research A* **300,** 132–136 (Jan. 1991).

96. Herrnstein, J. R. *et al.* A geometric distance to the galaxy NGC4258 from orbital motions in a nuclear gas disk. *Nature* **400,** 539–541 (Aug. 1999).

97. Hillas, A. M. Cerenkov light images of EAS produced by primary gamma. *International Cosmic Ray Conference* **3** (Aug. 1985).

98. Hönig, S. F., Watson, D., Kishimoto, M. & Hjorth, J. A dust-parallax distance of 19 megaparsecs to the supermassive black hole in NGC 4151. *Nature* **515,** 528–530 (Nov. 2014).

99. Humphreys, E. M. L., Reid, M. J., Moran, J. M., Greenhill, L. J. & Argon, A. L. Toward a New Geometric Distance to the Active Galaxy NGC 4258. III. Final Results and the Hubble Constant. *Astrophysical Journal* **775,** 13 (Sept. 2013).

100. Ichimaru, S. Bimodal behavior of accretion disks - Theory and application to Cygnus X-1 transitions. *Astrophysical Journal* **214,** 840–855 (June 1977).

101. Kanbach, G. *et al.* The project EGRET (Energetic Gamma-Ray Experiment Telescope) on NASA's Gamma-Ray Observatory (GRO). *Space Science Reviews* **49,** 69–84 (1988).

102. Kazanas, D. & Ellison, D. C. The central engine of quasars and active galactic nuclei Hadronic interactions of shock-accelerated relativistic protons. *Astrophysical Journal* **304,** 178–187 (May 1986).

103. Kennicutt Jr., R. C. The Global Schmidt Law in Star-forming Galaxies. *Astrophysical Journal* **498,** 541–552 (May 1998).

104. Khiali, B. & de Gouveia Dal Pino, E. M. High-energy neutrino emission from the core of low luminosity AGNs triggered by magnetic reconnection acceleration. *Monthly Notices of the RAS* **455,** 838–845 (Jan. 2016).

105. Kimura, S. S., Murase, K. & Toma, K. Neutrino and Cosmic-Ray Emission and Cumulative Background from Radiatively Inefficient Accretion Flows in Low-luminosity Active Galactic Nuclei. *Astrophysical Journal* **806,** 159 (June 2015).

106. Kimura, S. S., Toma, K., Suzuki, T. K. & Inutsuka, S.-i. Stochastic Particle Acceleration in Turbulence Generated by Magnetorotational Instability. *Astrophysical Journal* **822,** 88 (May 2016).

107. King, A. The AGN-Starburst Connection, Galactic Superwinds, and M_{BH}-σ. *Astrophysical Journal Letters* **635,** L121–L123 (Dec. 2005).

108. Kormendy, J. & Ho, L. C. Coevolution (Or Not) of Supermassive Black Holes and Host Galaxies. *Annual Review of Astronomy and Astrophysics* **51,** 511–653 (Aug. 2013).

109. Krimm, H. A. *et al.* The Swift/BAT Hard X-Ray Transient Monitor. *Astrophysical Journal, Supplement* **209,** 14 (Nov. 2013).

110. Lacki, B. C., Thompson, T. A., Quataert, E., Loeb, A. & Waxman, E. On the GeV and TeV Detections of the Starburst Galaxies M82 and NGC 253. *Astrophysical Journal* **734,** 107 (June 2011).

111. Lamastra, A. *et al.* Galactic outflow driven by the active nucleus and the origin of the gamma-ray emission in NGC 1068. *Astronomy and Astrophysics* **596,** A68 (Dec. 2016).

112. Lasota, J.-P. *et al.* Is the Accretion Flow in NGC 4258 Advection Dominated? *Astrophysical Journal* **462,** 142 (May 1996).

113. Lasota, J.-P., Vieira, R. S. S., Sadowski, A., Narayan, R. & Abramowicz, M. A. The slimming effect of advection on black-hole accretion flows. *Astronomy and Astrophysics* **587,** A13 (Mar. 2016).

114. Lenain, J.-P., Ricci, C., Türler, M., Dorner, D. & Walter, R. Seyfert 2 galaxies in the GeV band: jets and starburst. *Astronomy and Astrophysics* **524,** A72 (Dec. 2010).

115. Lenc, E. & Tingay, S. J. The Sub-Parsec Scale Radio Properties of Southern Starburst Galaxies. II. Supernova Remnants, the Supernova Rate, and the Ionised Medium in the NGC 4945 Starburst. *Astronomical Journal* **137,** 537–553 (Jan. 2009).

116. Lobban, A. P. *et al.* Evidence for a truncated accretion disc in the low-luminosity Seyfert galaxy, NGC 7213? *Monthly Notices of the RAS* **408,** 551–564 (Oct. 2010).

117. Loh, A. *et al.* High-energy gamma-ray observations of the accreting black hole V404 Cygni during its 2015 June outburst. *Monthly Notices of the RAS* **462,** L111–L115 (Oct. 2016).

118. Lubiński, P. *et al.* A comprehensive analysis of the hard X-ray spectra of bright Seyfert galaxies. *Monthly Notices of the RAS* **458,** 2454–2475 (May 2016).

119. Lubiński, P. *et al.* Extreme flux states of NGC 4151 observed with INTEGRAL. *Monthly Notices of the RAS* **408,** 1851–1865 (Nov. 2010).

120. Lucarelli, F. *et al.* AGILE detection of the new unidentified gamma-ray source AGL J2241+4454. *The Astronomer's Telegram* **2761** (July 2010).

121. Madejski, G. *et al.* Structure of the Circumnuclear Region of Seyfert 2 Galaxies Revealed by Rossi X-Ray Timing Explorer Hard X-Ray Observations of NGC 4945. *Astrophysical Journal, Letters* **535,** L87–L90 (June 2000).

122. Mahadevan, R. & Quataert, E. Are Particles in Advection-dominated Accretion Flows Thermal? *Astrophysical Journal* **490,** 605–618 (Dec. 1997).

123. Mahadevan, R., Narayan, R. & Krolik, J. Gamma-Ray Emission from Advection-dominated Accretion Flows around Black Holes: Application to the Galactic Center. *Astrophysical Journal* **486,** 268–275 (Sept. 1997).

124. Malyshev, D., Zdziarski, A. A. & Chernyakova, M. High-energy gamma-ray emission from Cyg X-1 measured by Fermi and its theoretical implications. *Monthly Notices of the RAS* **434,** 2380–2389 (Sept. 2013).

125. Malzac, J. & Belmont, R. The synchrotron boiler and the spectral states of black hole binaries. *Monthly Notices of the RAS* **392,** 570–589 (Jan. 2009).

126. Manmoto, T. Advection-dominated Accretion Flow around a Kerr Black Hole. *Astrophysical Journal* **534,** 734–746 (May 2000).

127. Marisaldi, M. *et al.* Detection of terrestrial gamma ray flashes up to 40 MeV by the AGILE satellite. *Journal of Geophysical Research (Space Physics)* **115,** A00E13 (Mar. 2010).

128. Marisaldi, M. *et al.* Gamma-Ray Localization of Terrestrial Gamma-Ray Flashes. *Physical Review Letters* **105,** 128501 (Sept. 2010).

129. Marisaldi, M. *et al.* Gamma-ray Localization of Terrestrial Gamma-ray Flashes by AGILE. *AGU Fall Meeting Abstracts,* AE11A–0330 (Dec. 2010).

130. Marisaldi, M. *et al.* Properties of terrestrial gamma ray flashes detected by AGILE MCAL below 30 MeV. *Journal of Geophysical Research (Space Physics)* **119,** 1337–1355 (Feb. 2014).

131. Markowitz, A. The X-Ray Power Spectral Density Function and Black Hole Mass Estimate for the Seyfert Active Galactic Nucleus IC 4329a. *Astrophysical Journal* **698,** 1740–1748 (June 2009).

132. Marscher, A. P. *et al.* Observational evidence for the accretion-disk origin for a radio jet in an active galaxy. *Nature* **417,** 625–627 (June 2002).

133. Mattox, J. R. *et al.* The Likelihood Analysis of EGRET Data. *Astrophysical Journal* **461,** 396 (Apr. 1996).

134. McClintock, J. E., Narayan, R. & Steiner, J. F. Black Hole Spin via Continuum Fitting and the Role of Spin in Powering Transient Jets. *Space Science Reviews* **183,** 295–322 (Sept. 2014).

135. McConnell, M. L. *et al.* The Soft Gamma-Ray Spectral Variability of Cygnus X-1. *Astrophysical Journal* **572,** 984–995 (June 2002).

136. Medvedev, M. V. Particle Heating by Nonlinear Alfvénic Turbulence in Advection-dominated Accretion Flows. *Astrophysical Journal* **541,** 811–820 (Oct. 2000).

137. Meyer, L. *et al.* The Shortest-Known-Period Star Orbiting Our Galaxys Supermassive Black Hole. *Science* **338,** 84 (Oct. 2012).

138. Miyamoto, S., Kitamoto, S., Iga, S., Negoro, H. & Terada, K. Canonical time variations of X-rays from black hole candidates in the low-intensity state. *Astrophysical Journal, Letters* **391,** L21–L24 (May 1992).

139. Miyoshi, M. *et al.* Evidence for a black hole from high rotation velocities in a sub-parsec region of NGC4258. *Nature* **373,** 127–129 (Jan. 1995).

140. Moiseev, A. A. *et al.* The anti-coincidence detector for the GLAST large area telescope. *Astroparticle Physics* **27,** 339–358 (June 2007).

141. Munar-Adrover, P. *et al.* Discovery of X-Ray Emission from the First Be/Black Hole System. *Astrophysical Journal, Letters* **786,** L11 (May 2014).

142. Munar-Adrover, P. *et al.* The Gamma-Ray Source AGL J2241+4454 as the Possible Counterpart of MWC 656. *Astrophysical Journal* **829,** 101 (Oct. 2016).

143. Narayan, R. & Yi, I. Advection-dominated accretion: A self-similar solution. *Astrophysical Journal* **428,** L13–L16 (June 1994).

144. Narayan, R. & Yi, I. Advection-dominated Accretion: Underfed Black Holes and Neutron Stars. *Astrophysical Journal* **452,** 710 (Oct. 1995).

145. Neronov, A., Tinyakov, P. & Tkachev, I. TeV Signatures of Compact UHECR Accelerators. *Soviet Journal of Experimental and Theoretical Physics* **100,** 656–662 (Apr. 2005).

146. Neyman, J. & Pearson, E. S. On the Use and Interpretation of Certain Test Criteria for Purposes of Statistical Inference: Part I. *Biometrika* **20A,** 175–240. ISSN: 00063444 (1928).

147. Niedźwiecki, A., Xie, F.-G. & Stepnik, A. Gamma-ray emission from proton-proton interactions in hot accretion flows. *Monthly Notices of the RAS* **432,** 1576–1586 (June 2013).

148. Niedźwiecki, A., Xie, F.-G. & Zdziarski, A. A. General relativistic model of hot accretion flows with global Compton cooling. *Monthly Notices of the RAS* **420,** 1195–1206 (Feb. 2012).

149. Niedźwiecki, A., Stępnik, A. & Xie, F.-G. On the Role and Origin of Nonthermal Electrons in Hot Accretion Flows. *Astrophysical Journal* **799,** 217 (Feb. 2015).

150. Niedźwiecki, A., Xie, F.-G. & Stępnik, A. X-ray spectra of hot accretion flows. *Monthly Notices of the RAS* **443,** 1733–1747 (Sept. 2014).

151. Novikov, I. D. & Thorne, K. S. *Astrophysics of black holes.* in *Black Holes (Les Astres Occlus)* (eds Dewitt, C. & Dewitt, B. S.) (1973), 343–450.

152. Ohm, S. Starburst galaxies as seen by gamma-ray telescopes. *Comptes Rendus Physique* **17,** 585–593 (June 2016).

153. Oka, K. & Manmoto, T. Gamma-ray emission from an accretion flow around a Kerr black hole. *Monthly Notices of the RAS* **340,** 543–550 (Apr. 2003).

154. Orosz, J. A. *et al.* The Mass of the Black Hole in Cygnus X-1. *Astrophysical Journal* **742,** 84 (Dec. 2011).

155. Paczynski, B. Mass of Cygnus X-1. *Astronomy and Astrophysics* **34,** 161–162 (Aug. 1974).

156. Padovani, P. & Urry, C. M. Luminosity functions, relativistic beaming, and unified theories of high-luminosity radio sources. *Astrophysical Journal* **387,** 449–457 (Mar. 1992).

157. Padovani, P. *et al.* Active galactic nuclei: what's in a name? *The Astronomy and Astrophysics Review* **25,** 2 (Aug. 2017).

158. Pancoast, A. *et al.* Erratum: Modelling reverberation mapping data - II. Dynamical modelling of the Lick AGN Monitoring Project 2008 data set. *Monthly Notices of the RAS* **448,** 3070–3070 (Apr. 2015).

159. Perotti, F., Fiorini, M., Incorvaia, S., Mattaini, E. & Sant'Ambrogio, E. The AGILE anticoincidence detector. *Nuclear Instruments and Methods in Physics Research A* **556,** 228–236 (Jan. 2006).

160. Peterson, B. M. *et al.* Central Masses and Broad-Line Region Sizes of Active Galactic Nuclei. II. A Homogeneous Analysis of a Large Reverberation-Mapping Database. *Astrophysical Journal* **613,** 682–699 (Oct. 2004).

161. Piano, G. *et al.* The AGILE monitoring of Cygnus X-3: transient gamma-ray emission and spectral constraints. *Astronomy and Astrophysics* **545,** A110 (Sept. 2012).

162. Pittori, C. The Gamma-Ray Imaging Detector AGILE: Scientific Goals and Instrument Performance. *Chinese Journal of Astronomy and Astrophysics Supplement* **3,** 517–522 (Dec. 2003).

163. Pittori, C. *et al.* First AGILE catalog of high-confidence gamma-ray sources. *Astronomy and Astrophysics* **506,** 1563–1574 (Nov. 2009).

164. Poutanen, J. & Veledina, A. Modelling Spectral and Timing Properties of Accreting Black Holes: The Hybrid Hot Flow Paradigm. *Space Science Reviews* **183,** 61–85 (Sept. 2014).

165. Poutanen, J., Veledina, A. & Revnivtsev, M. G. Colours of black holes: infrared flares from the hot accretion disc in XTE J1550-564. *Monthly Notices of the RAS* **445,** 3987–3998 (Dec. 2014).

166. Press, W. H., Teukolsky, S. A., Vetterling, W. T. & Flannery, B. P. *Numerical recipes in FORTRAN. The art of scientific computing* (1992).

167. Ptitsyna, K. & Neronov, A. Particle acceleration in the vacuum gaps in black hole magnetospheres. *Astronomy and Astrophysics* **593,** A8 (Aug. 2016).

168. Puccetti, S. *et al.* The Variable Hard X-Ray Emission of NGC 4945 as Observed by NuSTAR. *Astrophysical Journal* **793,** 26 (Sept. 2014).

169. Quataert, E. Particle Heating by Alfvénic Turbulence in Hot Accretion Flows. *Astrophysical Journal* **500,** 978–991 (June 1998).

170. Quataert, E. & Gruzinov, A. Turbulence and Particle Heating in Advection-dominated Accretion Flows. *Astrophysical Journal* **520,** 248–255 (July 1999).

171. Rappoldi, A. *et al.* Search of MeV-GeV counterparts of TeV sources with AGILE in pointing mode. *Astronomy and Astrophysics* **587,** A93 (Mar. 2016).

172. Rees, M. J., Begelman, M. C., Blandford, R. D. & Phinney, E. S. Ion-supported tori and the origin of radio jets. *Nature* **295,** 17–21 (Jan. 1982).

173. Reid, M. J. *et al.* The Trigonometric Parallax of Cygnus X-1. *Astrophysical Journal* **742,** 83 (Dec. 2011).

174. Remillard, R. A. & McClintock, J. E. X-Ray Properties of Black-Hole Binaries. *Annual Review of Astron and Astrophys* **44,** 49–92 (Sept. 2006).

175. Reynolds, C. S. Measuring Black Hole Spin Using X-Ray Reflection Spectroscopy. *Space Science Reviews* **183,** 277–294 (Sept. 2014).

176. Reynolds, C. S. *et al.* Probing the Accretion Disk and Central Engine Structure of NGC 4258 with Suzaku and XMM-Newton Observations. *Astrophysical Journal* **691,** 1159–1167 (Feb. 2009).

177. Rojas-Bravo, C. & Araya, M. Search for gamma-ray emission from star-forming galaxies with Fermi LAT. *Monthly Notices of the RAS* **463,** 1068–1073 (Nov. 2016).

178. Russell, D. M., Fender, R. P., Gallo, E. & Kaiser, C. R. The jet-powered optical nebula of Cygnus X-1. *Monthly Notices of the RAS* **376,** 1341–1349 (Apr. 2007).

179. Sabatini, S. *et al.* Episodic Transient Gamma-ray Emission from the Microquasar Cygnus X-1. *Astrophysical Journal, Letters* **712,** L10–L15 (Mar. 2010).

180. Sabatini, S. *et al.* Gamma-Ray Observations of Cygnus X-1 above 100 MeV in the Hard and Soft States. *Astrophysical Journal* **766,** 83 (Apr. 2013).

181. Sabatini, S. *et al.* On the Angular Resolution of the AGILE Gamma-Ray Imaging Detector. *Astrophysical Journal* **809,** 60 (Aug. 2015).

182. Sahakyan, N., Yang, R., Aharonian, F. A. & Rieger, F. M. Evidence for a Second Component in the High-energy Core Emission from Centaurus A? *Astrophysical Journal, Letters* **770,** L6 (June 2013).

183. Schnorr-Müller, A., Storchi-Bergmann, T., Nagar, N. M. & Ferrari, F. Gas inflows towards the nucleus of the active galaxy NGC 7213. *Monthly Notices of the RAS* **438,** 3322–3331 (Mar. 2014).

184. Schoenfelder, V. *et al.* Instrument description and performance of the Imaging Gamma-Ray Telescope COMPTEL aboard the Compton Gamma-Ray Observatory. *Astrophysical Journal Supplement Series* **86,** 657–692 (June 1993).

185. Schonfelder, V. & Kanbach, G. *Imaging through Compton scattering and pair creation* (eds Huber, M. C. E. *et al.*) 225–242. ISBN: 978-1-4614-7804-1 (Springer New York, New York, NY, 2013).

186. Shakura, N. I. & Sunyaev, R. A. Black holes in binary systems. Observational appearance. *Astronomy and Astrophysics* **24,** 337–355 (1973).

187. Shapiro, S. L., Lightman, A. P. & Eardley, D. M. A two-temperature accretion disk model for Cygnus X-1 - Structure and spectrum. *Astrophysical Journal* **204,** 187–199 (Feb. 1976).

188. Spruit, H. C. Particle acceleration in a flow accreting through shock waves. *Astronomy and Astrophysics* **194,** 319–327 (Apr. 1988).

189. Stern, B. E., Beloborodov, A. M. & Poutanen, J. Bizarre Hard X-Ray Outbursts of Cygnus X-1. *The Astrophysical Journal* **555,** 829–833 (July 2001).

190. Stirling, A. M. *et al.* A relativistic jet from Cygnus X-1 in the low/hard X-ray state. *Monthly Notices of the RAS* **327,** 1273–1278 (Nov. 2001).

191. Tanaka, Y. *et al.* Gravitationally redshifted emission implying an accretion disk and massive black hole in the active galaxy MCG-6-30-15. *Nature* **375,** 659–661 (June 1995).

192. Tananbaum, H., Gursky, H., Kellogg, E., Giacconi, R. & Jones, C. Observation of a Correlated X-Ray Transition in Cygnus X-1. *Astrophysical Journal, Letters* **177,** L5 (Oct. 1972).

193. Tang, Q.-W., Wang, X.-Y. & Tam, P.-H. T. Discovery of GeV Emission from the Direction of the Luminous Infrared Galaxy NGC 2146. *Astrophysical Journal* **794,** 26 (Oct. 2014).

194. Tavani, M. The variable Crab Nebula. *ArXiv e-prints.* arXiv: 1106.0164 [astro-ph.HE] (June 2011).

195. Tavani, M. *et al.* Extreme particle acceleration in the microquasar CygnusX-3. *Nature* **462,** 620–623 (Dec. 2009).

196. Tavani, M. *et al.* The AGILE Mission. *Astronomy and Astrophysics* **502,** 995–1013 (Aug. 2009).

197. Tully, R. B. *Nearby galaxies catalog* (1988).

198. Tully, R. B. *et al.* The Extragalactic Distance Database. *Astronomical Journal* **138,** 323–331 (Aug. 2009).

199. Urry, C. M. & Padovani, P. Unified Schemes for Radio-Loud Active Galactic Nuclei. *Publications of the ASP* **107,** 803 (Sept. 1995).

200. Urry, M. *The AGN Paradigm for Radio-Loud Objects* in *Active Galactic Nuclei: From Central Engine to Host Galaxy* (eds Collin, S., Combes, F. & Shlosman, I.) **290** (2003), 3. eprint: astro-ph/0301309.

201. van Paradijs, J. *Neutron Stars and Black Holes in X-Ray Binaries* in *NATO Advanced Science Institutes (ASI) Series C* (eds Buccheri, R., van Paradijs, J. & Alpar, A.) **515** (1998), 279. eprint: astro-ph/9802177.

202. Veledina, A., Vurm, I. & Poutanen, J. A self-consistent hybrid Comptonization model for broad-band spectra of accreting supermassive black holes. *Monthly Notices of the RAS* **414,** 3330–3343 (July 2011).

203. VERITAS Collaboration *et al.* A connection between star formation activity and cosmic rays in the starburst galaxy M82. *Nature* **462,** 770–772 (Dec. 2009).

204. Verrecchia, F. *et al.* An updated list of AGILE bright γ-ray sources and their variability in pointing mode. *Astronomy and Astrophysics* **558,** A137 (Oct. 2013).

205. Vurm, I. & Poutanen, J. Time-Dependent Modeling of Radiative Processes in Hot Magnetized Plasmas. *Astrophysical Journal* **698,** 293–316 (June 2009).

206. Walton, D. J. *et al.* Hard X-Ray Lags in Active Galactic Nuclei: Testing the Distant Reverberation Hypothesis with NGC 6814. *Astrophysical Journal, Letters* **777,** L23 (Nov. 2013).

207. Wilks, S. The large-sample distribution of the likelihood ratio for testing composite hypotheses. English. *Ann. Math. Stat.* **9,** 60–62. ISSN: 0003-4851 (1938).

208. Wojaczyński, R. & Niedźwiecki, A. The X-/γ-Ray Correlation in NGC 4945 and the Nature of Its γ-Ray Source. *Astrophysical Journal* **849,** 97 (Nov. 2017).

209. Wojaczyński, R., Niedźwiecki, A., Xie, F.-G. & Szanecki, M. Gamma-ray activity of Seyfert galaxies and constraints on hot accretion flows. *Astronomy and Astrophysics* **584,** A20 (Dec. 2015).

210. Xie, F.-G. & Yuan, F. Radiative efficiency of hot accretion flows. *Monthly Notices of the RAS* **427,** 1580–1586 (Dec. 2012).

211. Xie, F.-G., Niedźwiecki, A., Zdziarski, A. A. & Yuan, F. Monte Carlo simulations of global Compton cooling in inner regions of hot accretion flows. *Monthly Notices of the RAS* **403,** 170–178 (Mar. 2010).

212. Yoast-Hull, T. M., Gallagher III, J. S., Zweibel, E. G. & Everett, J. E. Active Galactic Nuclei, Neutrinos, and Interacting Cosmic Rays in NGC 253 and NGC 1068. *Astrophysical Journal* **780,** 137 (Jan. 2014).

213. Yuan, F. & Narayan, R. Hot Accretion Flows Around Black Holes. *Annual Review of Astron and Astrophys* **52,** 529–588 (Aug. 2014).

214. Zanin, R. *et al.* Gamma rays detected from Cygnus X-1 with likely jet origin. *Astronomy and Astrophysics* **596,** A55 (Nov. 2016).

215. Zdziarski, A. A. & Gierliński, M. Radiative Processes, Spectral States and Variability of Black-Hole Binaries. *Progress of Theoretical Physics Supplement* **155,** 99–119 (2004).

216. Zdziarski, A. A., Malzac, J. & Bednarek, W. A model of the TeV flare of Cygnus X-1: electron acceleration and extended pair cascades. *Monthly Notices of the RAS* **394,** L41–L45 (Mar. 2009).

217. Zdziarski, A. A., Johnson, W. N. & Magdziarz, P. Broad-band γ-ray and X-ray spectra of NGC 4151 and their implications for physical processes and geometry. *Monthly Notices of the RAS* **283,** 193–206 (Nov. 1996).

218. Zdziarski, A. A., Mikołajewska, J. & Belczyński, K. Cyg X-3: a low-mass black hole or a neutron star. *Monthly Notices of the RAS* **429,** L104–L108 (Feb. 2013).

219. Zdziarski, A. A., Malyshev, D., Chernyakova, M. & Pooley, G. G. High-energy gamma-rays from Cyg X-1. *Monthly Notices of the RAS* **471,** 3657–3667 (Nov. 2017).

220. Zdziarski, A. A., Poutanen, J. & Johnson, W. N. Observations of Seyfert Galaxies by OSSE and Parameters of Their X-Ray/Gamma-Ray Sources. *Astrophysical Journal* **542,** 703–709 (Oct. 2000).

221. Zdziarski, A. A., Lubiński, P. & Sikora, M. The MeV spectral tail in Cyg X-1 and optically thin emission of jets. *Monthly Notices of the RAS* **423,** 663–675 (June 2012).

222. Zdziarski, A. A., Poutanen, J., Paciesas, W. S. & Wen, L. Understanding the Long-Term Spectral Variability of Cygnus X-1 with Burst and Transient Source Experiment and All-Sky Monitor Observations. *Astrophysical Journal* **578,** 357–373 (Oct. 2002).

223. Ziółkowski, J. Determination of the masses of the components of the HDE 226868/Cyg X-1 binary system. *Monthly Notices of the RAS* **440,** L61–L65 (May 2014).